IMPACTS OF AGE AND EXERCISE ON SUBENDOTHELIAL MATRIX MECHANICS

A Dissertation

Presented to the Faculty of the Graduate School

of Cornell University

In Partial Fulfillment of the Requirements for the Degree of

Doctor of Philosophy

by

Julie Carol Kohn

August 2017

IMPACTS OF AGE AND EXERCISE ON SUBENDOTHELIAL MATRIX MECHANICS

Julie Carol Kohn, Ph. D.

Cornell University 2017

The artery is a complex tissue composed of multiple layers, the mechanical properties of which can influence disease development. The inner-most layer, the intima, is comprised of a monolayer of endothelial cells which reside on the subendothelial matrix tissue. Cholesterol permeation past the endothelial cell monolayer and into the vessel wall is an initiating step of atherosclerosis, the build-up of plaque in arteries. Cardiovascular disease is a major cause of death worldwide, and its risk factors, including increased age, poor diet, and sedentary lifestyle, cause arterial stiffening. While most studies focus on bulk arterial stiffening caused by these risk factors, here, we focused on changes in the micro-scale subendothelial matrix. As a consequence of substrate stiffening, endothelial cell-cell junctions begin to separate, a key step in vessel permeation. In this thesis work, we sought to understand the cardiovascular risk factors that alter subendothelial matrix mechanics and the effects of these mechanical cues on endothelial cells.

In the first study of this thesis work, an *in vitro* model was used to analyze the dual effects of substrate stiffness and physiological shear flow on endothelial cells. We determined that these factors in concert effect RhoA activity and nitric oxide production, important factors to proper cardiovascular health. In the subsequent *in vivo* experiments, we found that the subendothelial matrix stiffens heterogeneously with age, and this effect can be reversed with an exercise

regimen. We also demonstrated that consistent exercise is important in the maintenance of proper cardiovascular health through the mitigation of age-induced micro-scale stiffening. Exercise also provided an ameliorating effect on micro-scale stiffening caused by Western diet consumption, but did not decrease bulk stiffening to the same extent. Finally, an *in silico* model of endothelial cells on heterogeneous substrates demonstrated that increased substrate stiffness heterogeneities, as are found in aged arteries, produced more heterogeneous endothelial cell basal strains upon applied substrate stretch and fluid shear stress. Overall, this thesis demonstrates that major cardiovascular risk factors such as advanced age, sedentary lifestyle, and poor diet influence the micro-scale mechanics of the artery intima, and we demonstrate impacts of these mechanical changes on endothelial cells. We propose that future studies seeking to combat atherogenesis may benefit from targeting subendothelial matrix stiffening.

BIOGRAPHICAL SKETCH

Julie Carol Kohn was born in New Brunswick, New Jersey on May 27, 1990 and grew up in Allendale, New Jersey with her two parents, Paul and Pamela Kohn. She attended Bucknell University and graduated magna cum laude in 2012 with a Bachelor of Science in Chemical Engineering, with a minor in Biomedical Engineering, and became a member of Tau Beta Pi and Mortar Board honor societies. In college, Julie worked in the laboratory of Dr. Donna Ebenstein on eliminating adhesion during nanoindentation experiments in fluids. During two of her summers in college, Julie was an engineering intern at Becton Dickinson in Franklin Lakes, New Jersey. She joined Cornell University's Ph. D. program in 2012 and was immediately interested in the laboratory of Dr. Cynthia A. Reinhart-King. In 2013, Julie was awarded the prestigious National Science Foundation Graduate Research Fellowship and throughout her Ph. D. studies was able to present her work at four engineering conferences. In 2016, Julie was awarded a Whitaker International Program Fellowship, and completed her final year of Ph. D. research with Dr. Thomas Franz at the University of Cape Town in South Africa. Julie loves to sing, play the trumpet, camp, and is a proud Girl Scout leader. She is an adventurous traveler and would like to combine this spirit with her passion for helping others following graduation.

To Pamela and Paul Kohn

for their constant love and support

ACKNOWLEDGMENTS

First, I would like to sincerely thank Dr. Cynthia Reinhart-King for the opportunity to work in her laboratory and experience her mentorship. I have grown in so many ways over my time in her lab, and I cannot imagine where I would be today without those experiences. She has helped me understand not only the field of mechanobiology, but also how to conduct thorough and important research and to communicate those studies to the larger public. I would also like to recognize my thesis committee members Dr. Jan Lammerding and Dr. Eve Donnelly for their support through my work, even as my research moved across the globe. In my work overseas, Dr. Thomas Franz also allowed me to develop as a researcher as I started working in a new field.

I am grateful to the National Science Foundation for their fellowship and the ability to conduct high-quality research about which I am passionate. To the Whitaker International Program, thank you for making the final year of my Ph. D. research one I will never forget and for understanding that learning can happen beyond the lab bench. To my collaborators and fellow authors: Dr. Chih-Chang Chu, Dr. Francesca Seta, Dr. David Putnam, Dr. Mingyu He, Na Young Kim, Dennis Zhou, and Allen Zhou, I appreciated the opportunity to work on different projects with you and grow the biomedical engineering field.

To my CRK lab mates, including Dr. François Bordeleau, Dr. Saumendra Bajpai, Dr. Casey Kraning-Rush, Dr. Brooke Mason, Dr. Shawn Carey, Dr. Courtney Faber, Joseph Miller, Danielle LaValley, Aniqua Rahman, Emmanuel Lollis, Jacob VanderBurgh, Lauren Hapach, Matthew Zanotelli,

Marianne Lintz, Johanna Uribe and Adam Muñoz: thank you for keeping me sane, for the deep conversations, the office decorations and the eventful wine tours. I cannot believe we made it all of these years together and still never saw the Pumpkin Fairy. I would especially like to recognize the Masters of Engineering and Bachelors of Science students whom I worked with on this journey: Nicholas Deisadze, Adeline Chen, Stephanie Cheng, Peter Joe, Katharina Fung, Shweta Modi, Jenny Ma, and Julian Azar. I appreciate your patience as I learned how to become a better mentor and for the tireless hours you poured into making our research impactful.

There will always be a special place in my heart for the three people who entered the CRK lab with me as first-year students. To Alexandra McGregor: your heart and passion are immense and your dedication to your friends, family and research are unmeasurable. I am glad that I got to know and work with you and I know one day you will make a wonderful professional researcher. To Turi Alcoser: the strength you brought to your relationships and to your research will never be forgotten. In our short time together, you made a large impact in my life and the lives of many others. Of course, Dr. Marsha Lampi: thank you for the constant support and late-night talks. I am very grateful for getting to spend five years with you developing our friendship and learning how to buffer glass the perfect amount. We did it! And finally, for helping me through a tough time, a special thank you goes to David.

Moving across the world can be intimidating, but my lab mates and friends at the University of Cape Town were there for me throughout the whole process. Thank you to the UCT Mechanobiology lab, including: Dr. Mazin Sirry, Dr. Andie De Villiers, Chimwemwe Msosa, Dodzi

Motchon, Lee Kruse, John Nchejane, Juliet Nagawa, Riham Ahmed, Absalom Maluleke, Ghodeejah Higgins, Jerry Sam, Nicholas Mandel, and Thabi Matseke. Special appreciation goes to Dr. Tamer Abdalrahman and Kevin Sack, for working patiently with me and who helped me believe in my computational modeling abilities. My friends in Cape Town became my African family, and I was glad to share my world with yours.

I would especially like to thank my housemates Meredith Horne, Dr. Mary Clare McCorry, Dr. Hannah Watkins, Ruari, Mary Godec, Lana, and Mark Arand. Thank you for dealing with me before 10 am, and for providing me with steak dinners, surprise ice cream, big hugs, and warm licks. To all of my friends at Cornell- you were my Ithaca family, and I will always treasure our outdoor adventures, wine tours, rock climbing sessions, Canadian expeditions, and talks under the stars.

The most important thank you must go to my parents. Although our family is small, we are tight-knit and undefeatable. Thank you for filling our house with love and taking care of Skinny and Stuffed, Lucky, Hopper and Jumper, Comet, Miracle, Shae Lee, and my countless fish all of these years. Somehow you managed that on top of your involvement with my Girl Scouts, sports, and music activities. I know 100% that I am writing this today because of our Saturday morning family meetings, hours of multiplication flash cards, and lots of chocolate before my exams. Somehow you helped me find the balance in life between academics (where I had an organic chemistry tutor before I even took the class), and my social life (throwing Friday night parties and going on exotic jungle vacations). I cannot imagine having a more empathetic and dedicated family.

TABLE OF CONTENTS

List of Figures and Tables

Chapter 1: Introduction

Chapter 2: Cooperative effects of matrix stiffness and fluid shear stress on endothelial cell behavior

Chapter 3: Mechanical heterogeneities in the subendothelial matrix develop with age and decrease with exercise

Chapter 4: Beneficial effects of exercise on arterial stiffness are short-lived

Chapter 5: Western diet-induced subendothelial matrix stiffening is mitigated by exercise

Chapter 6: Subendothelial matrix heterogeneities induce heterogeneous basal cell strain

Chapter 8: Additional Studies

Appendix D: Mouse surgery for aorta extraction and thoracic aorta cleaning

List of Abbreviations

AFM	Atomic force microscopy
AGE	Advanced glycation end product
ANOVA	Analysis of variance
Arg	Arginine
BAEC	Bovine aortic endothelial cell
BCA	Bicinchoninic acid
BP	Blood pressure
CML	N(ε) carboxymethyl-lysine
CVD	Cardiovascular disease
DAF-FM	4-amino-5-methylamino-2’,7’-difluorofluorescein
DAPI	4’,6-diaminido-2-phenylindole
DOX	Doxorubicin
EC	Endothelial cell
ECG	Electrocardiogram
ECM	Extracellular matrix
EKV	ECG-gated Kilohertz Visualization
ELISA	Enzyme linked immunosorbent assay
eNOS	Endothelial nitric oxide synthase
Erk1/2	Extracellular signal-regulated kinase
FA	Focal adhesion

FAK	Focal adhesion kinase
HFHS	High fat, high sugar or ‘Western’ diet
Leu	Leucine
LVEF	Left ventricular ejection fraction
MAEC	Mouse aortic endothelial cell
MAP	Mean arterial pressure
MEM	Minimum essential media
MLC	Myosin light chain
MMP	Matrix metalloproteinase
ND	Normal diet
NO	Nitric oxide
NS	Not statistically significant
OA	Opening angle
PA	Polyacrylamide
PBS	Phosphate buffered saline
PECAM	Platelet-endothelial cell adhesion molecule
PWV	Pulse wave velocity
RAGE	Receptor for advanced glycation end products
RIPA	Radioimmunoprecipitation assay
ROCK	Rho-associated protein kinase
ROS	Reactive oxygen species
SEM	Standard error of the mean

SIM	Structured illumination microscope
TEM	Transmission electron microscopy
VE-cadherin	Vascular endothelial cadherin
VSMC	Vascular smooth muscle cell

CHAPTER 1

INTRODUCTION

Portions of this chapter are published in Frontiers in Genetics.[1]

1.1 Introduction to cardiovascular disease and arterial stiffness

Cardiovascular disease (CVD) is the leading cause of death in the United States due to the incidence of stroke and heart attack, and is of primary concern in the population over 65 years old.[2,3] Atherosclerosis, or the formation of plaques in arteries, is initiated by uptake of cholesterol into the artery wall, and is mediated by the inner layer of the artery, the intima. The intima is a complex region comprised of the extracellular matrix (ECM), primarily collagen and elastin, and the endothelial cell (EC) monolayer (Figure 1.1). The ECM tissue immediately beneath the EC monolayer is known as the basement membrane, and together with the connective tissue and the internal elastic lamina, comprises the intima ECM. The outer layers of the artery wall include the media, predominantly comprised of vascular smooth muscle cells, and the adventitia, which together are orders of magnitude stiffer than the intima.[4] Therefore, intimal stiffness is outweighed by the media and adventitia in bulk mechanical measurement of vessels.

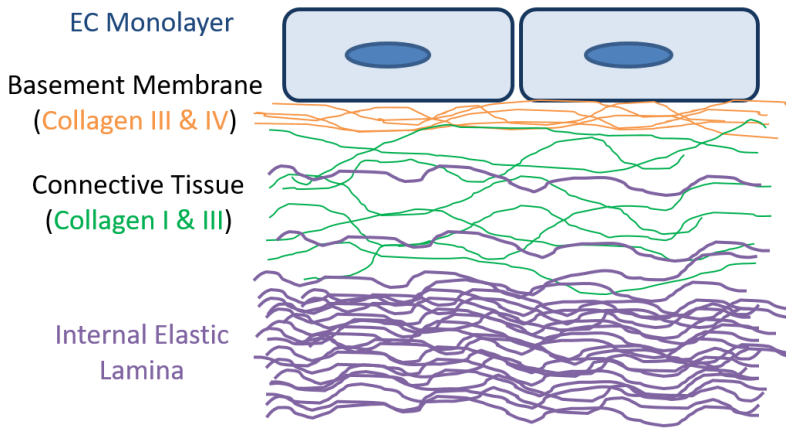

Figure 1.1: The structure of the intima layer of the artery wall, comprising of an endothelial cell monolayer and the extracellular matrix fibers, primarily collagen and elastin.

While micro-scale subendothelial matrix stiffness, has recently been shown to increase with age[5] and poor diet,[6] bulk or macro-scale stiffness is still more widely studied and used for clinical evaluation. Key risk factors for the development of CVD include increased age, lack of exercise, and poor diet,[7] and are clinically assessed using bulk mechanical measurements. The gold standard for clinical measurement to predict CVD is through pulse wave velocity (PWV).[8,9] Indeed, higher aortic PWV in humans is associated with a 48% increase in CVD risk,[10] and PWV has been shown to increase with age and decrease with exercise.[11–13] Bulk aortic health is also measured by arterial compliance,[14] release of nitric oxide (NO) while exercising,[15] and forward pressure wave amplitude.[16] Arterial response to acetylcholine[17–19] and bradykinin[20,21] serves as another metric of cardiovascular health and decreases with age, demonstrating that age impacts arterial function.

1.2 Cells respond to mechanical stimuli

Cells are known to respond to many types of mechanical cues, such as shear stress[22,23] and ECM stiffness.[24,25] Durotaxis, the process by which cells selectively migrate according to matrix stiffness, has been demonstrated in ECs,[26,27] and is mediated by traction forces and focal adhesions (FAs).[28–31] Cells both exert forces on the ECM (endogenous forces), often resulting from cytoskeleton contraction, and respond to forces from the ECM (exogenous forces).[32] On stiffer substrates, cells exhibit increased cell-ECM adhesion[33] and ECs increase their spreading.[34,35] ECs on a stiff matrix also demonstrate more defined actin stress fibers and are more stiff themselves than ECs placed on more compliant gels; in fact, ECs taken from a gel and seeded onto glass increased their elastic modulus within 8 hours from 2.5 to more than 3 kPa.[36]

ECs adhere to the subendothelial matrix through FA complexes, assemblies of scaffold and effector proteins together with integrins. Integrin proteins also serve to anchor actin stress fibers to the ECM.[37] Importantly, these complexes sense the biochemistry, topography and mechanical forces present in the environment, and transfer these signals to the cytoskeleton, primarily through actin polymerization and actomyosin contraction.[37] For example, impairment of focal adhesion kinase helps to tighten endothelial cell-cell junctions.[38] ECM stiffness impacts FA dynamics, as those formed on compliant matrices are punctate and short-lived, while those on stiffer substrates are more elongated and are found in stable arrays.[32,39] Shear stress can also impact FAs dynamics, as cells under shear exhibit FAs aligned with the flow direction, and a coalescence of smaller FAs into fewer but larger FAs.[40]

In vitro platforms are used to simulate the mechanical stiffness and other physiological properties of *in vivo* tissue. Polyacrylamide (PA) gels are commonly used to mimic physiological tissue stiffness, due to the ease of tuning the mechanical properties, the beneficial optical qualities, and ability to adhere ECM proteins onto these gels.[41] PA gels are also biocompatible and cells can be seeded and cultured on the top surface.[27,36] Collagen gels can also be used to simulate 3D ECM environments with variations in stiffness.[36,42] Micropillars or microposts serve as another *in vitro* platform, and can be patterned with ECM islands through microcontact printing,[43] allowing for defined points of contact between the cell and ECM. Recently, it was shown that cells respond with heterogeneous traction force distributions when placed on micropillars with different compliance.[44] Finally, computational, or *in silico*, models can be used to determine cellular mechanosensitivity, such as EC response to shear stress[45] and focal adhesion dynamics.[46]

1.3 Initiation of atherosclerosis

1.3.1 Endothelial cell-cell junctions

The EC monolayer creates an important barrier, whose function is necessary in preventing many diseases.[47,48] Importantly, cholesterol permeation past the EC monolayer and into the vessel wall is an initiating step of atherosclerosis.[49] This barrier protection is imperative to vascular health, and is damaged with increased aging.[5,50] The EC barrier is modulated by adherins junctions, which can be effected through vasoactive factors such as vascular endothelial growth factor and thrombin.[51,52] Higher traction forces between the cell and the ECM cause increased actomyosin contractility and gaps in the EC monolayer.[51,53] Therefore, junction integrity is a function of centripetal tension created by EC contraction due to actomyosin activation.[54,55]

EC monolayers on stiff matrices display an atheroprone phenotype with increased junction width and monolayer permeability *in vitro* and *in vivo*.[5,51] ECM stiffness has been shown to regulate EC contractility and F-actin stress fiber formation through Rho, Rho-associated protein kinase (ROCK), and myosin light chain (MLC) signaling.[25,54,56,57] Contractility is activated in cells placed on stiffer gels, and is mediated by myosin light chain phosphorylation.[25,57] Cell contraction is a function of many mechanical cues and signaling pathways, most notably the Rho GTPases, where Rho is known to control stress fiber formation and actomyosin bundles, and Rac and cdc42 form lamellipodia and filopodia.[58–60] EC contractility disrupts adherins junctions, causing EC barrier dysfunction, and increased permeability of small molecules into the vascular wall (Figure 1.2). Barrier dysfunction is also responsible for other pro-atherosclerotic events such as neutorphil transmigration.[25]

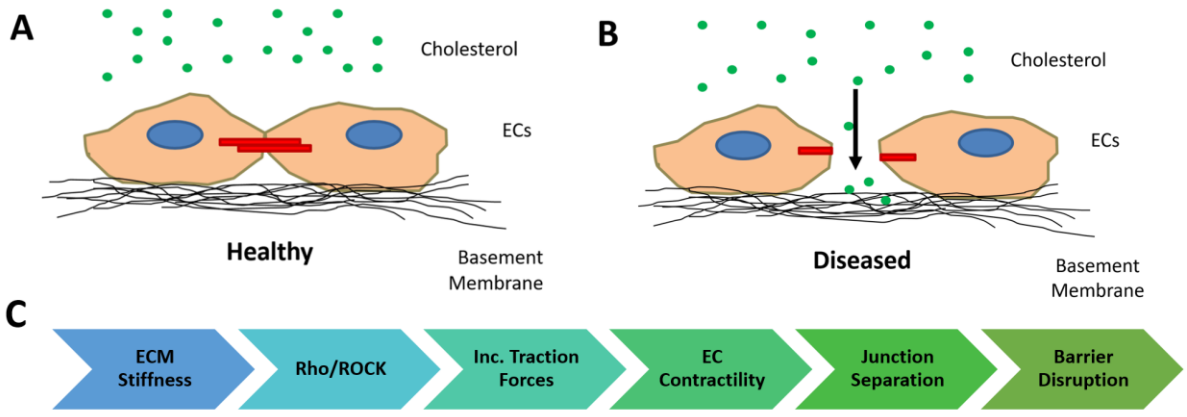

Figure 1.2: Compared to endothelial cells (ECs) in a healthy vessel (A), ECs in a diseased artery (B) can contract, creating junctional gaps, and cholesterol can permeate into the artery. (C) ECM stiffness leads to endothelial monolayer barrier disruption through cell mechanosensing.

In ECs, the key junctional protein vascular endothelial (VE)-cadherin links to F-actin through catenins, forming complexes with proteins in the armadillo family, and acts as a cell-cell mechanosensor.[52,61–63] This protein can be fluorescently tagged and imaged to measure the distance between ECs, the EC junction width, which is indicative of EC barrier function.[5] Monolayer permeability can also be assessed *in vitro* or *in vivo* through measuring the amount of dye which permeates through the membrane over time.[5,52,64]

The complex interplay between the intima ECM, integrins, cytoskeletal proteins and cadherins mediates the junctional integrity of the EC monolayer (Figure 1.3). Many factors have complex effects on junctional integrity, such as RhoA, which promotes junction gaps when concentrated at contractile filaments, but helps to close junction gaps when recruited at membrane protrusions.[56] Interestingly, NO has been shown to destabilize adherins junctions by mediating stress fiber formation and VE-cadherin phosphorylation by controlling the balance of Rho and Rac activation.[52] Shear stress also plays a role in VE-cadherin-mediated junctional integrity by decreasing cell-cell junction tension, and by triggering cytoskeletal remodeling.[65]

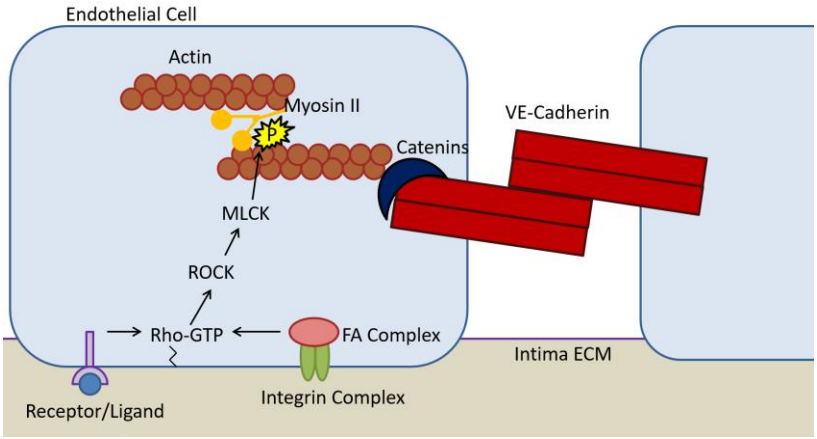

Figure 1.3: Mechanical cues from the intima ECM can be transduced through focal adhesion complexes and disrupt VE-cadherin via the Rho/ROCK pathway.

1.3.2 Nitric oxide and endothelial cell function

NO is a potent vasodialator[66,67] and mediates endothelium-dependent vascular smooth muscle cell (VSMC) relaxation.[66,68] Activation of the PI3K/Akt pathway upregulates NO production and vascular compliance through endothelial nitric oxide synthase (eNOS),[69] which is activated through phosphorylation at Ser1177.[12,70] In ECs, activated eNOS converts L-arginine into NO, which diffuses into the VSMCs of the media and activates guanylate cyclase to produce cGMP, which medicates vascular contraction and relaxation.[71–73] (Figure 1.4).

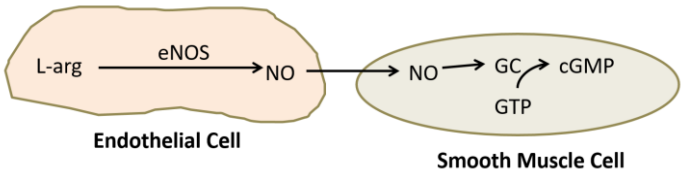

Figure 1.4: Nitric oxide production occurs in the endothelial cells and influences vascular smooth muscle cell contraction and relaxation.

Importantly, decreased NO production and impaired vessel dilation are hallmarks of EC dysfunction.[74–76] NO helps to maintain artery health,[77,78] and mice with less available NO display higher bulk arterial stiffness.[69] In fact, with advanced age, eNOS gene and protein expression decreases.[12,79] NO production increases under applied fluid shear stress[80,81] which can be initiated through exercise,[20] and the stable degradation product of NO, nitrite, also increases with exercise.[82] Indeed, eNOS activity decreases with age[12,21] and eNOS gene and protein production increases with exercise.[12,82] Immunohistochemistry images of eNOS production by EC *in vivo*[83] display patterns of high concentrations of eNOS in certain areas of the intima. *In vitro*, NO production can be assessed fluorescently by using a DAF-FM substrate which fluoresces after permeating the cell membrane and interacting with NO.[69,84]

Advanced age impairs EC eNOS production,[12,79] and damages mitochondrial function, leading to increased reactive oxygen species (ROS) formation.[85] Aged ECs are more prone to apoptosis *in vivo*,[86] which is enhanced by pro-atherosclerotic factors such as oxidized LDL, pro-inflammatory cytokines and increased ROS,[87–89] which promote oxidative stress. Inversely, NO helps to protect against EC apoptosis.[89–91] In young ECs, ROS such as superoxide and hydrogen peroxide are

quenched by the antioxidant enzymes, superoxide dismutase and catalase.[76] However, this pattern breaks down in aged ECs, and a pro-oxydant phenotype is seen through decreased NO production.[76] Indeed, ECs cultured *in vitro* to the 14th passage show reduced eNOS and decreases in Akt phosphorylation and S-NO production by over 30%.[87] Even the application of shear stress, which normally has a profound apoptosis inhibitory effect through NO production, failed to upregulate eNOS protein or NO production, and therefore failed to inhibit apoptosis in aged ECs, although the ECs did align in the shear direction.[87] Other cardiovascular risk factors, such as poor diet and lack of exercise can also alter the eNOS pathways and the bioavailability of NO.[79,92–94] Okabe *et al.* (2007) show that apolipoprotein E knockout mice treated with a high-fat diet display increased eNOS production following an exercise regimen. Exercise is also known to increase shear stress on ECs,[20] which can regulate the eNOS pathway.[78,95]

1.4 Importance of understanding micro-scale stiffness

Historically, greater emphasis has been placed on macro-scale arterial testing than on layer-specific mechanics because bulk properties are used clinically and are associated with cardiovascular events including aneurism, atherosclerosis, and hypertension.[96–98] However, the artery is a complex viscoelastic composite material, and therefore, proper mechanical testing should incorporate these attributes.[99] Since PWV does not provide an accurate measurement of artery mechanics at a scale that cells can sense, previous studies have used micro-scale mechanical testing to measure micro-scale mechanical properties. Atomic force microscopy (AFM) can be used to collect force curves and elastic modulus values of ECs.[25,53] AFM has also been used to indent vessel ECM, which shows that cardiovascular risk factors such as age and

poor diet increase intimal stiffness.[5,6] Importantly, subendothelial matrix stiffness has been shown to influence EC barrier function, a mediator of atherosclerotic plaque development.[5,56,57] Cholesterol permeability between ECs due to EC barrier dysfunction is an initiating step to arterial inflammation and plaque development.[48,49,100] Not only do cells respond to the mechanical ECM cues, but they can detect small heterogeneities in stiffness. Recently, single cells were seeded on micropillar arrays of heterogeneous stiffness and demonstrated higher traction forces on the stiff side.[44] These data indicate that cells are mechanosensitive to micro-scale stiffness cues in their environment and may be influenced by small, heterogeneous stiffness changes. This highlights the need to study the *in vivo* spatial stiffness heterogeneity patterns in the subendothelial matrix and the response of ECs to these micro-scale mechanical changes.

1.5 Arterial stiffness measurement techniques

1.5.1 Methods to measure macro-scale stiffness

Bulk mechanical testing on arteries is well-established and has been performed for over half a century.[101,102] Macro-scale arterial mechanics are used clinically to predict the likelihood of cardiovascular disease risk,[103] and are also essential to the development of tissue engineered vascular grafts.[104] Several macro-scale techniques for measuring the mechanical properties of intact arteries have been developed (Figure 1.5).

Technique	Diagram	Measurement
Tensile Testing	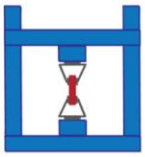	Bulk biological tissue mechanics
Opening Angle		Bulk residual mechanics of biological tissue
Pulse-Wave Velocity	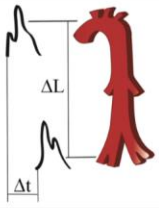	Clinical measurement Bulk arterial system mechanics
Ultrasound	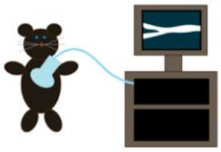	Clinical measurement Visual analysis of arterial distensibility and compliance

Figure 1.5: Macro-scale techniques to determine artery mechanics.

The most common method to determine the elastic modulus of an artery is based on the quotient of stress and strain derived from tensile testing. Despite the widespread use of tensile testing, there are more than four definitions of stress and strain in the literature, which leads to differences in the values obtained through mechanical testing results.[105] Tensile measurements are made by applying tension to a material until it reaches failure, producing a stress-strain curve. Artery samples are removed from the host, cut circumferentially or longitudinally, stored in temperature-controlled environments and tested within 48 hours of surgery.[105] As opposite ends of the sample are pulled vertically, the material enters the plastic regime and begins to exhibit necking, before ultimately reaching the failure point. Tensile testing has been performed on

human arteries to characterize their mechanical changes in a number of conditions, including aging,[106–108] as well as plaque[109] and aneurism development.[110] Most often, aortas, coronary arteries, and carotid arteries are used to study the differential mechanics of diseased states after autopsy because they are the dominant sites of disease development, and as the largest vessels, they are also the easiest to obtain.[109,111–113]

The opening angle (OA) is a measure of the residual stress of an unloaded tissue and has been used as an indicator of artery composition and viscoelasticity.[114–116] The OA measurement was originally developed to understand the stress-free state of tissues[117] but can also be used to elucidate the viscoelastic properties of an artery after tissue loading.[118] OA measurements are also performed in concert with other mechanical tests, such as tensile testing,[119] and in doing so have demonstrated a correlation between OA and arterial stiffness. Although taking an OA measurement is useful when analyzing the residual stress and strain properties of the arterial wall, it limits further testing on the uncut artery.

PWV measurements are the primary clinical method used to assess arterial stiffening and to help predict CVD events.[8,9,120] PWV is the measurement of the time for a pressure wave to propagate down the atrial tree over a known distance. A non-invasive ultrasound or invasive catheter method can be used to record the pressure wave in two different locations on the body. The physical distance between the two locations, usually the carotid and femoral arteries in humans, is measured on the surface of the body using a tape measure, and the velocity measurement is the ratio of distance traveled to elapsed time.[8,96] Measurements along the aorta and aorto-iliac

pathway are the most clinically relevant because the aorta and its branches are the first vessels that blood encounters out of the heart and PWV values using this pathway have been shown as predictive values for arterial stiffness.[8] PWV is directly correlated with the elastic modulus by the Moens–Korteweg equation, which takes into account the vessel radius and the wall thickness and density.[102] PWV values are inversely correlated with artery distensibility and compliance.[121] However, PWV does not take into account the differences in arterial stiffness between elastic and muscular parts of the vascular tree.[8]

PWV has many advantages over direct mechanical testing because it can be used for clinical applications, is non-invasive when using an ultrasound technique, and can be used to calculate elastic modulus values. Ultrasound non-invasively images internal organs using sound waves and the associated reflected waves. Ultrasound and its accompanying image processing techniques provide a simple and visual determination of arterial mechanical properties. B-mode, or brightness-mode, ultrasound can be used to image a two-dimensional cross-section of the vessel, whereas M-mode, or motion-mode, can record B-mode images in quick succession, providing a 'video' of the cross-sectional area. Pulse-Doppler ultrasound records images over time, but also employs the Doppler effect to record blood movement in the vessel. Due to the prevalence of ultrasound equipment, ultrasound is used extensively to produce non-invasive measurements of artery mechanics in both clinical and research settings. Blood pressure if often also measured simultaneously to help provide a better understanding of cardiovascular health. [12,122,123]

PWV is correlated with arterial stiffness and can be used to predict cardiovascular disease in patients.[10,124] Higher PWV measurements are associated with a higher risk of stroke, cardiovascular death, and coronary heart disease.[125] Patients with hypertension and high aortic PWV measurements have increased stenosis frequency, and a higher prevalence of atherosclerotic lesions in the aorta and lower extremities.[126] Hallock (1934) used PWV measurements to determine that PWV in the aorta increases from 4.1 m/s in patients ages 5–9 to 6.4 m/s in patients ages 35–44 and up to 10.5 m/s for patients over 65.[101] Notably, PWV increases with age for both men and women,[101,127] and pulse pressure increases by 25% from ages 30 to 60.[128] Using PWV and distensibility measurements, the 2001 Rotterdam Study demonstrated that stiffness is associated with atherosclerosis in both the carotid artery and the aorta.[96] The Rotterdam study also indicated that aortic stiffness alone can be used as a predictor of atherosclerosis because elevated aortic stiffness is associated with atherosclerosis throughout the entire arterial tree.[96] PWV has become a powerful method for predicting cardiovascular risk clinically, and in hypertensive patients, it is the best predictor of cardiovascular mortality regardless of age.[103] PWV can also be used to assess stiffness of murine arteries through ultrasound images.[11,30,129]

In addition to PWV measurements, distensibility, and compliance measurements obtained using ultrasound are also used clinically to assess cardiovascular health. Using ultrasound B- and M-modes, the expansion and contraction of the artery with the cardiac pulse can be measured to determine distensibility, which is a measure of artery elasticity.[130,131] A decrease in artery distensibility is directly correlated with increasing arterial stiffness, and therefore, indicates that

distensibility can be used as a metric for cardiovascular disease.[132,133] The clinical definition of compliance is the ratio of blood volume to arterial blood pressure, although in practice, the compliance of an artery can be measured as the ratio of change in cross-sectional area to the change in pressure, which is known as the cross-sectional compliance[134,135] Decreased arterial compliance is correlated with a higher risk of cardiovascular disease.[136] Techniques in ultrasound software can also assess other cardiovascular risk factors, such as wall strain,[130] atherosclerotic plaque location, and intima-media thickness.[96,132] In addition to age-related effects, patients with increased serum cholesterol also have impaired radial artery compliance and distensibility.[137] A decrease in compliance can be attributed to altered arterial and blood flow pressures due to increases in wall thickening, collagen deposition, or elastin fragmentation.[136]

1.5.2 Methods to measure micro-scale stiffness

While significant emphasis has been placed on macro-scale measurements of vessel mechanics, less is known about the changes in the mechanical properties of the individual arterial layers or the ECM within these layers. Macro-scale measurements generally treat the artery as a uniform material, and do not take into account that arteries are composite materials with three distinct layers. Mechanical analysis on the cell-scale is fundamental to the field of mechanobiology and our understanding of the mechanical cues driving cell behavior and function. Several approaches to measure micro-scale mechanical changes have been developed which measure layer-specific mechanical changes. Micro-scale tests are more relevant for studies of cellular mechanotransduction in the vessel wall and investigations of the cellular response to changes in arterial mechanics (Figure 1.6).

Technique	Diagram	Measurement
Atomic Force Microscopy	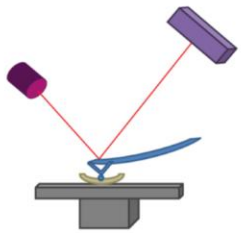	Sub-cellular mechanics Cellular mechanics Local biological tissue mechanics
Nanoindentation		Cellular mechanics Local biological tissue mechanics
Micropipette Aspiration	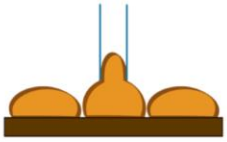	Cellular mechanics Local biological tissue mechanics

Figure 1.6: Micro-scale techniques to measure vascular mechanics.

The use of AFM force indentation measurements for ECM mechanical testing in arteries is a relatively newer technique, and it allows for layer-specific mechanical properties to be determined. In AFM, a cantilever with a micron-scale tip is brought in contact with a sample, and as the cantilever deflects, a laser beam focused on the back of the cantilever is also deflected, providing information regarding the indentation.[138,139] The two primary AFM modes are 'contact mode,' where the cantilever tip is dragged along the sample surface, or 'AC (tapping)' mode, where the tip oscillates near its resonant frequency close to the sample surface and intermittent indentations are recorded.[140] Most commonly, AFM is used to "image" samples, creating a topographical map, by dragging the cantilever across a sample.[141] AFM tip materials, geometries, and sizes are dependent on the specific application. AFM indentations for force measurements

can use tips with radii from ~5 to 50 nm, allowing for nanoscale resolution.[141] Spherical beads of varying diameters up to the micro-scale can also be placed on the AFM cantilever for force indentation measurements.[142,143] AFM tips can also be functionalized with biological sensors that limit the interaction area with the material.[144,145]

There has been an increasing interest in the technique of AFM to obtain force measurements on biological materials.[5,6,146] AFM force measurement records the deflection of the cantilever as it indents into the sample material to produce a force versus indentation curve.[139] Data can be fit to standard mathematical models such as the Hertz model, to provide mechanical properties such as the elastic modulus at the indentation location.[146–148] Within the vasculature, AFM has been used to measure local stiffness at different locations within an artery, as well as the mechanical contributions of specific ECM components, namely collagen and elastin.[149] AFM has also been used to study the mechanics of atherosclerotic plaques and fibrous caps,[150,151] as well the effects of age and diet on intima stiffness.[5,6,146]

Importantly, the values found using AFM are orders of magnitude smaller than those found using tensile testing due to the multiple layers in the artery. In porcine aortas, AFM testing showed the tunica adventitia had an elastic modulus range of 0.7–391 kPa and that the pulmonary arteries have a stiffer adventitia that ranges between 2.3 and 1,130 kPa.[152] Notably, AFM testing of the porcine medial layer indicates it is orders of magnitude stiffer than the adventitia, and has an elastic modulus ranging from 1 to 30 MPa.[149] Furthermore, Lundkvist et al. (1997), reported the intima stiffness of healthy human arteries is 34.4 kPa when measured using AFM,[153] while tensile

testing on the composite artery indicates an elastic modulus ranging between 1.5 and 3.8 MPa.[110,113] Bulk mechanical measurement techniques typically provide values of the stiffest layer, the media, primarily comprised of collagen fibers and smooth muscle cells;[1,36] however, this value does not represent the stiffness of the entire vessel. When probed individually, it is apparent that single artery layers, such as the intima, are orders of magnitude more compliant. The wide stiffness range of the different artery layers underscore the importance of analyzing mechanical properties of individual layers using micro-scale techniques, especially when studying behaviors of mechanosensitive cells.

AFM has also been used to study cellular and sub-cellular mechanics using live samples, including measuring EC stiffness.[154,155] It was suggested that cells adopt the relative stiffness values of their matrix; therefore, cell-stiffness may be a measure of vascular health.[36] On the subcellular level, AFM has been used to study the properties of the plasma membrane, ECM, and cytoskeleton.[156,157] When performing sub-cellular analysis, AFM tips can be modified to create bio-specific molecular sensors that are used for studying surface receptor interactions and measuring adhesion molecule stiffness.[144,158] Simultaneous topography and recognition imaging is a recent advancement in AFM technology, where a ligand is functionalized to the AFM cantilever tip to provide simultaneous measurements of material topography and cell-ligand interactions.[159] A recent study using topography and recognition imaging with a VE-cadherin-Fc modified AFM tip showed VE-cadherin forms ellipsoid clusters and suggests the protein is bound to actin filaments.[145] Because AFM can be used to determine artery mechanics at the cellular and

subcellular levels, and its applications continue to develop, it is expected to have increased prevalence in the mechanobiology field.

Nanoindentation measurements use a nano-scale tip to indent into a material and generate a load versus displacement curve that can be used to calculate material mechanics, such as hardness. Unlike AFM which records cantilever displacements, in nanoindentation, an external load is applied to the indenter tip to push the tip into the surface.[138] Displacement in nanoindentation is measured directly by the cantilever's depression into the sample surface, unlike the deflected laser measurement used by the AFM. Whereas older studies relied on imaging the tip depression in the sample to determine the area of contact, current nanoindentation methods can estimate the area of contact based on a well-defined tip geometry, such as a triangular Berkovich or spheroid tip.[160] Many biological materials have been characterized using nanoindentation,[161] including carotid plaques.[162] Arterial tissue probed with nanoindentation indicates that porcine elastic aortas have elastic moduli between 60 and 70 kPa.[163] The technique has also been used to measure the mechanical properties of rat arteries, where the effective elastic moduli ranged from 22 to 37 kPa.[164] The arterial stiffness values obtained with nanoindentation are comparable to AFM measurements, and both are orders of magnitude lower than the bulk vessel stiffness. Nanoindentation allows for micro- and nanoscale measurements, with a force range of 1 μN to 500 mN, and a displacement range of 1 nm to 20 μm.[161,165] Nanoindentors have indentation depths on the nanometer scale;[165] however, their contact area with the material can be hundreds to thousands of nanometers wide.[141] These

length scales bridge the gap between more sensitive AFM measurements and macro-scale testing.

Different mathematical models are used to fit AFM and nanoindentation data, including the Hertz model,[147,166] the Oliver-Pharr model,[160,167] and the Johnson–Kendall–Roberts (JKR) adhesion model.[168] The choice of analysis model is based on the properties of the tip-sample interaction, taking into account the shape of the indentation curve and any discontinuities in the curve.[138] For biological tissues and hydrated biomaterials, significant adhesion between the tip and sample must be accounted for when determining mechanical properties with nanoindentaiton.[169]

A final micro-scale technique, micropipette aspiration, uses suction through a pipette to pull one end of a cell or matrix into a 0.5–0.8 mm glass tube.[170,171] The distance the material travels into the pipette is tracked using microscopy[172] and is directly related to the material stiffness. Soft biological tissue mechanics can be measured using pipette aspiration by applying an aspiration pressure on the inside of the pipette to deform the tissue.[173] The elastic moduli measured using micropipette aspiration are similar to the values obtained using AFM and nanoindentation. Although micropipette aspiration is relatively simple to perform and is well-characterized, it is a lesser used technique for testing the mechanics of *ex vivo* samples. AFM particularly has become more popular, likely due to its versatility in measuring cellular and sub-cellular properties.

1.6 Causes of arterial stiffening

1.6.1 Changes due to age, diet and exercise

Age[5,174] and Western (high-fat, high-sugar) diet[6] increase arterial stiffness on the macro-scale and micro-scale in animal models. Interestingly, biaxial tensile testing has shown that individuals over the age of 30 have stiffer abdominal aortas compared to younger patients.[106] With age, arterial collagen production increases and elastin content decreases, leading to an increase in overall arterial stiffness.[136,175] Collagen fibers are thought to be orders of magnitude stiffer than elastin[176], and their increased concentration in the artery leads to stiffening. Specifically, collagen I and III are the load-bearing matrix fibers and comprise 90% of the collagen fibers in the artery.[4,177] While arteries from mice on a Western diet do not display increased collagen content, they do present increased activity for the crosslinker transglutaminase 2, which returned to baseline following change to a normal diet.[6] Elastin fragmentation and fibrosis is increased in aged human aortas,[178] and there is an increase in elastin-degrading plasma matrix metalloproteinases (MMPs).[179,180] In fact, serum levels of MMP-9, another elastin-degrading enzyme, is directly correlated with PWV.[181] The medial and adventitial layers are the primary effectors of bulk arterial stiffness as they are orders of magnitude stiffer than the intima. Measurements of collagen and elastin throughout the artery wall show the intima comprises more elastin than collagen, whereas the adventitia has an equal amount of both proteins.[182] One study shows that the intima ECM is primarily composed of 75% elastin and 25% collagen in healthy vessels, with most fibers oriented axially.[182] However, while the impacts of cardiovascular risk factors, such as age and diet have been primarily studied on the macro-scale, and more data are needed on the effects on intimal health alone.

Exercise is beneficial to arterial health and reduces risk for CVD.[7] Exercise regimens have been used to mitigate the impacts of age[174] and Western diet[94] on macro-scale stiffness, and prevent the suppression of NO caused by Western diet.[94] Subjects after an exercise regimen show an increase in arterial compliance in humans,[14] and a decrease in bulk arterial stiffness in rodents.[13,174] Treadmill exercise in rats promotes increased eNOS phosphorylation and increased NO/cGMP, measured through transglutaminase 2 function.[12] While some studies measure a decrease in collagen and increase elastin fiber production with exercise training,[13,174] other studies demonstrate similar elastin and collagen amounts post-treatment.[12,183] Recently, exercise has also been shown to modify the internal elastic lamina and increase arterial elastin content in Western diet-fed mice.[30] Cardiac exercise increases blood flow and pulse pressure, increasing shear stress on ECs.[20] Shear stress is known to increase the expression of atheroprotective genes such as eNOS and decreases the expression of the atheroprone genes to increase superoxide.[22] The dual effects of shear stress and stiffness on EC phenotype have recently been explored to show that cells on more compliant gels are more sensitive to changes in shear stress and respond to the ROCK inhibitor Y-27632,[23] which influences cell contractility. Therefore, while exercise can be used for arterial destiffening, the effects on intima-specific changes have not been well-studied.

1.6.2 Advanced glycation end products

Aged artery stiffness is also altered by the increased presence of ECM cross linkers such as advanced glycation end products (AGEs).[184] Proteins and lipids can be modified with AGEs

through a Maillard reaction,[185] and cause increased artery stiffness *in vivo* through crosslinks.[186,187] N(ε) carboxymethyl-lysine (CML) is a common AGE found *in vivo*, is linked to diabetes,[188] and has been shown to decrease in arteries of exercised animals.[13] Gu *et al*. (2014) show that aged rats not only demonstrated elevated levels of plasma CML, but also aortic CML content, which was mitigated by exercise.[13] Atherosclerotic plaques and foam cells contain high levels of CML modifications.[186] Young mice administered a high-fat diet demonstrate a significant increase in arterial AGEs, which are also elevated in healthy old mice.[189] CML is known as a dietary AGE whose function is receptor for AGEs (RAGE) dependent,[190] as it is a ligand for RAGE, triggering vascular inflammation cascades.[191] Importantly, CML plays a role in inducing arterial stiffening and endothelium-dependent relaxation.[190]

The increased presence of AGEs often results in unwanted cardiovascular effects and CML serves as a biomarker for oxidative damage.[186] AGEs and NO production are linked through a variety of signaling aspects,[185] and AGEs can be detrimental to vascular health through a decrease in NO availability.[84,185] For example, glycated low-density lipoprotein decreases NO production,[192] and AGEs promote increased expansion of the molecular packing of collagen.[193] The activation of RAGE is known to increase myosin activity, promoting cell rigidity,[194] and the addition of the AGE/RAGE complex to arteries increases mitochondrial superoxide production,[195] which promotes oxidative stress. In mice, AGEs, PWV and superoxide all increase with age and decrease with treatment of sodium nitride,[184] a compound which neutralizes free radicals with NO.

1.7 Organization of the dissertation

The aim of this work is to explore the implications of age, exercise, and diet on micro-scale subendothelial matrix stiffening and stiffening heterogeneity. We find that all of these factors have impacts on both macro- and micro-scale stiffness and we provide a few possible causes for this stiffening. Finally, we use these data in a computational model to examine the effects of heterogeneous stiffening on ECs. In Chapter 2, we demonstrate that ECM stiffness and shear stress in concert effect EC function through measuring NO production. These data are applicable to the underlying effects of cardiac exercise on vascular health due to the increased shear stress placed on ECs during exercise. In Chapter 3, we investigate the effects of age and exercise on micro-scale changes in intima stiffness. We find that not only does the intima stiffen with age, but that advanced age causes increased micro-scale heterogeneity. This effect is reversed by exercise, as both mean stiffness and the amount of heterogeneity decrease following an exercise regimen. We also demonstrate a linear correlation between macro-scale stiffness measured through PWV and micro-scale stiffness of the intima for the animals in this study. In Chapter 4, the long-lasting impact of exercise is tested through an *in vivo* study where aged mice undergo an eight-week exercise regimen, and then an eight-week sedentary period. Macro- and micro-scale stiffness, as well as cardiac function, all showed significant benefit due to the exercise period, but after rest, these values returned to their pre-exercise baseline levels. This study also demonstrates that intimal collagen and serum AGEs decrease following exercise, and begin to return to baseline following rest. In Chapter 5, young mice are fed a high-fat, high-sugar (HFHS) diet and then underwent a return to a normal diet or an exercise period. A return to normal diet de-stiffened the arteries on both the macro- and micro-scales. However, exercised mice on a

HFHS diet only showed a benefit to their micro-scale intimal stiffness. Overall, these data demonstrate the importance of diet on arterial health and, unlike the correlation found in the Chapter 3 study, that micro- and macro-scale stiffness can be effected by different treatments. In Chapter 6, a computational model was produced that measures the impact of subendothelial matrix stiffness heterogeneities on a single EC or multiple EC model. The values of the heterogenous 'aged' and homogeneous 'young' matrices were supplied from data collected during the study in Chapter 3, and ECs on the 'aged' matrix displayed increased basal strain heterogeneity. Conclusions from the thesis work overall and proposed future directions are presented in Chapter 7. Chapter 8 details additional experiments completed during the Ph. D. research, but which are not included in the primary work. Protocols for key experimental methods that were created or modified are found in the appendices.

1.8 References

1. Kohn, J. C., Lampi, M. C. (co-first authors) & Reinhart-King, C. A. Age-related vascular stiffening: causes and consequences. *Front. Genet.* **6,** 112 (2015).
2. National Center for Health Statistics. *Health, United States, 2010: with special feature on death and dying*. (2010).
3. Benetos, A. *et al.* Influence of age, risk factors, and cardiovascular and renal disease on arterial stiffness: clinical applications. *Am. J. Hypertens.* **15,** 1101–1108 (2002).
4. Fleenor, B. S., Marshall, K. D., Durrant, J. R., Lesniewski, L. A. & Seals, D. R. Arterial stiffening with ageing is associated with transforming growth factor-β1-related changes in adventitial collagen: reversal by aerobic exercise. *J. Physiol.* **588,** 3971–3982 (2010).

5. Huynh, J. *et al.* Age-related intimal stiffening enhances endothelial permeability and leukocyte transmigration. *Sci. Transl. Med.* **3,** 112ra122 (2011).
6. Weisbrod, R. M. *et al.* Arterial stiffening precedes systolic hypertension in diet-induced obesity. *Hypertension* **62,** 1105–1110 (2013).
7. World Heart Federation. *Cardiovascular disease risk factors*. (2017).
8. Laurent, S. *et al.* Expert consensus document on arterial stiffness: methodological issues and clinical applications. *Eur. Heart J.* **27,** 2588–2605 (2006).
9. Van Bortel, L. M. *et al.* Expert consensus document on the measurement of aortic stiffness in daily practice using carotid-femoral pulse wave velocity. *J. Hypertens.* **30,** 445–448 (2012).
10. Mitchell, G. F. *et al.* Arterial stiffness and cardiovascular events: the Framingham Heart Study. *Circulation* **121,** 505–511 (2010).
11. Di Lascio, N., Stea, F., Kusmic, C., Sicari, R. & Faita, F. Non-invasive assessment of pulse wave velocity in mice by means of ultrasound images. *Atherosclerosis* **237,** 31–37 (2014).
12. Steppan, J. *et al.* Exercise, vascular stiffness, and tissue transglutaminase. *J. Am. Heart Assoc.* **3,** e000599 (2014).
13. Gu, Q. *et al.* Contribution of receptor for advanced glycation end products to vasculature-protecting effects of exercise training in aged rats. *Eur. J. Pharmacol.* **741,** 186–194 (2014).
14. Tanaka, H. *et al.* Aging, habitual exercise, and dynamic arterial compliance. *Circulation* **102,** 1270–1275 (2000).
15. Tordi, N. *et al.* Effects of resuming endurance training on arterial stiffness and nitric oxide production during exercise in elite cyclists. *Appl. Physiol. Nutr. Metab.* **31,** 244–249 (2006).
16. Cooper, L. L. *et al.* Components of hemodynamic load and cardiovascular events: The

Framingham Heart Study. *Circulation* **131,** 354–361 (2015).

17. Taddei, S. *et al.* Physical activity prevents age-related impairment in nitric oxide availability in elderly athletes. *Circulation* **101,** 2896–2901 (2000).
18. Donoso, M. V. *et al.* Aging differentially modifies arterial sensitivity to endothelin-1 and 5-hydroxytryptamine: Studies in dog coronary arteries and rat arterial mesenteric bed. *Peptides* **15,** 1489–1495 (1994).
19. Ragazzi, E. *et al.* Endothelial nucleotide-mediated aorta relaxation in aged Watanabe heritable hyperlipidemic rabbits. *J. Cardiovasc. Pharmacol.* **26,** 119–126 (1995).
20. Seals, D. R., Desouza, C. A., Donato, A. J. & Tanaka, H. Habitual exercise and arterial aging. *J. Appl. Physiol.* **105,** 1323–1332 (2008).
21. Cernadas, M. *et al.* Expression of Constitutive and Inducible Nitric Oxide Synthases in the Vascular Wall of Young and Aging Rats. *Circ. Res.* **83,** 279–286 (1998).
22. Laughlin, M. H., Newcomer, S. C. & Bender, S. B. Importance of hemodynamic forces as signals for exercise- induced changes in endothelial cell phenotype. *J. Appl. Physiol.* **104,** 588–600 (2008).
23. Galie, P., van Oosten, A., Chen, C. S. & Janmey, P. A. Application of multiple levels of fluid shear stress to endothelial cells plated on polyacrylamide gels. *Lab Chip* **15,** 1205–1212 (2015).
24. Hsu, C. C. *et al.* Blood pressure, atherosclerosis, and albuminuria in 10,113 participants of the atherosclerosis risk in communities (ARIC) study. *J. Hypertens.* **27,** 397–409 (2009).
25. Stroka, K. M. & Aranda-Espinoza, H. Endothelial cell substrate stiffness influences neutrophil transmigration via myosin light chain kinase-dependent cell contraction. *Blood* **118,** 1632–

1640 (2011).

26. Raab, M. *et al.* Crawling from soft to stiff matrix polarizes the cytoskeleton and phosphoregulates myosin-II heavy chain. *J. Cell Biol.* **199,** 669–683 (2012).
27. Lo, C. M., Wang, H. B., Dembo, M. & Wang, Y. L. Cell movement is guided by the rigidity of the substrate. *Biophys. J.* **79,** 144–152 (2000).
28. Isenberg, B. C., DiMilla, P. A., Walker, M., Kim, S. & Wong, J. Y. Vascular smooth muscle cell durotaxis depends on substrate stiffness gradient strength. *Biophys. J.* **97,** 1313–1322 (2009).
29. Plotnikov, S. V., Pasapera, A. M., Sabass, B. & Waterman, C. M. Force fluctuations within focal adhesions mediate ECM-rigidity sensing to guide directed cell migration. *Cell* **151,** 1513–1527 (2012).
30. Padilla, J. *et al.* Regular exercise reduces endothelial cortical stiffness in Western diet – fed female mice. *Hypertension* **68,** 1236–1244 (2016).
31. Vincent, L. G., Choi, Y. S., Alonso-Latorre, B., del Alamo, J. C. & Engler, A. J. Mesenchymal stem cell durotaxis depends on substrate stiffness gradient strength. *Biotechnol. J.* **8,** 472–484 (2013).
32. Mason, B. N., Califano, J. P. & Reinhart-King, C. A. in *Engineering Biomaterials for Regenerative Medicine* (ed. Bhatia, S. K.) 19–38 (Springer New York, 2012).
33. Engler, A. J. *et al.* Myotubes differentiate optimally on substrates with tissue-like stiffness: pathological implications for soft or stiff microenvironments. *J. Cell Biol.* **166,** 877–887 (2004).
34. Califano, J. P. & Reinhart-King, C. A. A balance of substrate mechanics and matrix chemistry regulates endothelial cell network assembly. *Cell. Mol. Bioeng.* **1,** 122–132 (2008).
35. Yeung, T. *et al.* Effects of substrate stiffness on cell morphology, cytoskeletal structure, and

adhesion. *Cell Motil. Cytoskeleton* **60,** 24–34 (2005).

36. Byfield, F. J., Reen, R. K., Shentu, T. P., Levitan, I. & Gooch, K. J. Endothelial actin and cell stiffness is modulated by substrate stiffness in 2D and 3D. *J. Biomech.* **42,** 1114–1119 (2009).
37. Geiger, B., Spatz, J. P. & Bershadsky, A. D. Environmental sensing through focal adhesions. *Mol. Cell Biol.* **10,** 21–33 (2009).
38. Arnold, K. M., Goeckeler, Z. M. & Wysolmerski, R. B. Loss of focal adhesion kinase enhances endothelial barrier function and increases focal adhesions. *Microcirculation* **20,** 637–649 (2013).
39. Pelham, R. J. J. & Wang, Y.-L. Cell locomotion and focal adhesions are regulated by substrate flexibility. *Proc. Natl. Acad. Sci. U. S. A.* **94,** 13661–13665 (1998).
40. Davies, P. F., Robotewskyj, A. & Griem, M. L. Quantitative studies of endothelial cell adhesion: directional remodeling of focal adhesion sites in response to flow forces. *J. Clin. Invest.* **93,** 2031–2038 (1994).
41. Wang, Y. L. & Pelham, R. J. J. Preparation of a flexible, porous polyacrylamide substrate for mechanical studies of cultured cells. *Methods in Enzymology* **298,** 489–496 (1998).
42. Mason, B. N., Starchenko, A., Williams, R. W., Bonassar, L. J. & Reinhart-King, C. A. Tuning 3D collagen matrix stiffness independently of collagen concentration modulates endothelial cell behavior. *Acta Biomater.* **9,** 4635–4644 (2013).
43. Tee, S.-Y., Fu, J., Chen, C. S. & Janmey, P. A. Cell shape and substrate rigidity both regulate cell stiffness. *Biophys. J.* **100,** L25–L27 (2011).
44. Breckenridge, M. T., Desai, R. A., Yang, M. T., Fu, J. & Chen, C. S. Substrates with engineered step changes in rigidity induce traction force polarity and durotaxis. *Cell. Mol. Bioeng.* **7,** 26–

34 (2014).

45. Ferko, M. C., Bhatnagar, A., Garcia, M. B. & Butler, P. J. Finite-element stress analysis of a multicomponent model of sheared and focally-adhered endothelial cells. *Ann. Biomed. Eng.* **35,** 208–223 (2007).
46. Nicolas, A., Geiger, B. & Safran, S. A. Cell mechanosensitivity controls the anisotropy of focal adhesions. *Proc. Natl. Acad. Sci. U. S. A.* **101,** 12520–12525 (2004).
47. Wojciak-Stothard, B. & Ridley, A. J. Rho GTPases and the regulation of endothelial permeability. *Vascul. Pharmacol.* **39,** 187–199 (2002).
48. Hansson, G. K. Inflammation, atherosclerosis, and coronary artery disease. *N. Engl. J. Med.* **353,** 1685–1695 (2005).
49. Lusis, A. Atherosclerosis. *Nature* **407,** 233–241 (2000).
50. Carlson, K. H., Bourne, W. M., McLaren, J. W. & Brubaker, R. F. Variations in human corneal endothelial cell morphology and permeability to fluorescein with age. *Exp. Eye Res.* **47,** 27–41 (1988).
51. Krishnan, R. *et al.* Substrate stiffening promotes endothelial monolayer disruption through enhanced physical forces. *Am. J. Physiol. Cell Physiol.* **300,** C146–C154 (2011).
52. Di Lorenzo, A. *et al.* eNOS-derived nitric oxide regulates endothelial barrier function through VE-cadherin and Rho GTPases. *J. Cell Sci.* **126,** 5541–5552 (2013).
53. Stroka, K. M. & Aranda-Espinoza, H. Effects of morphology vs. cell–cell interactions on endothelial cell stiffness. *Cell Mol. Bioeng.* **4,** 9–27 (2011).
54. Hsu, B. Y., Bae, Y. H., Mui, K. L., Liu, S.-L. & Assoian, R. K. Apolipoprotein E3 inhibits Rho to regulate the mechanosensitive expression of Cox2. *PLoS One* **10,** e0128974 (2015).

55. Dejana, E. Endothelial cell-cell junctions: happy together. *Mol. Cell Biol.* **5,** 261–270 (2004).

56. Szulcek, R. *et al.* Localized RhoA GTPase activity regulates dynamics of endothelial monolayer integrity. *Cardiovasc. Res.* **99,** 471–482 (2013).

57. Birukova, A. A. *et al.* Endothelial barrier disruption and recovery is controlled by substrate stiffness. *Microvasc. Res.* **87,** 50–57 (2013).

58. Ridley, A. Rho family proteins: coordinating cell responses. *Trends Cell Biol.* **11,** 471–477 (2001).

59. Ridley, A. J. & Hall, A. The small GTP-binding protein rho regulates the assembly of focal adhesions and actin stress fibers in response to growth factors. *Cell* **70,** 389–399 (1992).

60. Ridley, A. J., Paterson, H. F., Johnston, C. L., Diekmann, D. & Hall, A. The small GTP-binding protein rat regulates growth factor-induced membrane. *Cell* **70,** 401–410 (1992).

61. Etienne-Manneville, S. & Hall, A. Rho GTPases in cell biology. *Nature* **420,** 629–635 (2002).

62. Barry, A. K., Wang, N. & Leckband, D. E. Local VE-cadherin mechanotransduction triggers long-ranged remodeling of endothelial monolayers. *J. Cell Sci.* **128,** 1341–1351 (2015).

63. Ferreri, D., Minnear, F., Yin, T., Kowalczyk, A. & Vincent, P. N-cadherin levels in endothelial cells are regulated by monolayer maturity and p120 availability. *Cell Commun. Adhes.* **15,** 333–349 (2008).

64. Shen, Q., Rigor, R. R., Pivetti, C. D., Wu, M. H. & Yuan, S. Y. Myosin light chain kinase in microvascular endothelial barrier function. *Cardiovasc. Res.* **87,** 272–280 (2010).

65. Conway, D. E. *et al.* Fluid shear stress on endothelial cells modulates mechanical tension across VE-cadherin and PECAM-1. *Curr. Biol.* **23,** 1024–1030 (2013).

66. Cohen, R. A. *et al.* Mechanism of nitric oxide–induced vasodilatation. *Circ. Res.* **84,** 210–219

(1999).

67. Moncada, S., Palmer, R. M. & Higgs, E. A. Nitric oxide: physiology, pathophysiology, and pharmacology. *Pharmacol. Rev.* **43,** 109–142 (1991).
68. Cohen, R. A. *et al.* Nitric oxide is the mediator of both endothelium-dependent relaxation and hyperpolarization of the rabbit carotid artery. *Proc. Natl. Acad. Sci. U. S. A.* **94,** 4193–4198 (1997).
69. Soucy, K. G. *et al.* Impaired shear stress-induced nitric oxide production through decreased NOS phosphorylation contributes to age-related vascular stiffness. *J. Appl. Physiol.* **101,** 1751–1759 (2006).
70. Chung, A. Y. *et al.* Endothelial dysfunction and compromised eNOS/Akt signaling in the thoracic aorta during the progression of Marfan syndrome. *Br. J. Pharmacol.* **150,** 1075–1083 (2007).
71. Palmer, R. M. J., Ashton, D. S. & Moncada, S. Vascular endothelial cells synthesize nitric oxide from L-arginine. *Lett. to Nat.* **333,** 664–666 (1988).
72. Denninger, J. W. & Marletta, M. A. Guanylate cyclase and the NO/cGMP signaling pathway. *Biochim. Biophys. Acta* **1411,** 334–350 (1999).
73. Carvajal, J. A., Germain, A. M., Huidobro-Toro, J. P. & Weiner, C. P. Molecular mechanism of cGMP-mediated smooth muscle relaxation. *J. Cell. Physiol.* **184,** 409–420 (2000).
74. Szmitko, P. E. *et al.* New markers of inflammation and endothelial cell activation: Part I. *Circulation* **108,** 1917–1923 (2003).
75. Widlansky, M. E., Gokce, N., Keaney, J. F. & Vita, J. A. The clinical implications of endothelial dysfunction. *J. Am. Coll. Cardiol.* **42,** 1149–1160 (2003).

76. Donato, A. J., Morgan, R. G., Walker, A. E. & Lesniewski, L. A. Cellular and molecular biology of aging endothelial cells. *J. Mol. Cell. Cardiol.* 122–135 (2015).

77. Boo, Y. C. & Jo, H. Flow-dependent regulation of endothelial nitric oxide synthase: role of protein kinases. *Am. J. Physiol. Cell Physiol.* **285,** C499-508 (2003).

78. Li, H., Horke, S. & Förstermann, U. Vascular oxidative stress, nitric oxide and atherosclerosis. *Atherosclerosis* **237,** 208–219 (2014).

79. Tanabe, T. *et al.* Exercise training improves aging decrease in eNOS expression of the aorta. *Acta Physiol. Scand.* **178,** 3–10 (2003).

80. Wessells, H. *et al.* Fluid shear stress-induced nitric oxide production in human cavernosal endothelial cells: inhibition by hyperglycaemia. *Br. J. Urol. Int.* **97,** 1047–1052 (2006).

81. Corson, M. *et al.* Phosphorylation of endothelial nitric oxide synthase in response to fluid shear stre. *Circ. Res.* **79,** 984–991 (1996).

82. Sessa, W. C., Pritchard, K., Seyedi, N., Wang, J. & Hintze, T. H. Chronic exercise in dogs increases coronary vascular nitric oxide production and endothelial cell nitric oxide synthase gene expression. *Circ. Res.* **74,** 349–353 (1994).

83. Lake-Bruse, K. D. *et al.* Gene transfer of endothelial nitric oxide synthase (eNOS) in eNOS-deficient mice. *Am. J. Physiol.* **277,** H770–H776 (1999).

84. Bucala, R., Tracey, K. & A, C. Advanced glycosylation produces quench nitric oxide and mediate defective endothelium-dependent vasodilation in experimental diabetes. *J. Clin. Invest.* **87,** 432–438 (1991).

85. Kokoszka, J. E., Coskun, P., Esposito, L. A. & Wallace, D. C. Increased mitochondrial oxidative stress in the Sod2 (+/-) mouse results in the age-related decline of mitochondrial function

culminating in increased apoptosis. *Proc. Natl. Acad. Sci. U. S. A.* **98,** 2278–2283 (2001).

86. Asai, K. *et al.* Peripheral vascular endothelial dysfunction and apoptosis in old monkeys. *Arterioscler. Thromb. Vasc. Biol.* **20,** 1493–1499 (2000).
87. Hoffmann, J. *et al.* Aging enhances the sensitivity of endothelial cells toward apoptotic stimuli: important role of nitric oxide. *Circ. Res.* **89,** 709–715 (2001).
88. Dimmeler, S., Haendeler, J., Galle, J. & Zeiher, A. Oxidized low density lipoprotein induces apoptosis of human endothelial cells by activation of CPP32-like proteases: a mechanistic clue to the response to injury hypothesis. *Circulation* **95,** 1760–1763 (1997).
89. Dimmeler, S., Rippmann, V., Weiland, U., Haendeler, J. & Zeiher, A. Angiotensin II induces apoptosis of human endothelial cells: protective effect of nitric oxide. *Circ. Res.* **81,** 970–976 (1997).
90. Dimmeler, S. & Zeiher, a M. Nitric oxide-an endothelial cell survival factor. *Cell Death Dfferentiation* **6,** 964–968 (1999).
91. Haendeler, J., Zeiher, A. & Dimmeler, S. Nitric oxide and apoptosis. *Vitam. Horm.* **57,** 59–79 (1999).
92. Kleindienst, A. *et al.* Exercise does not activate the β3 adrenergic receptor–eNOS pathway, but reduces inducible NOS expression to protect the heart of obese diabetic mice. *Basic Res. Cardiol.* **111,** 40 (2016).
93. Gioscia-Ryan, R. A. *et al.* Aerobic exercise increases stress resistance in arteries of old mice. *FASEB J.* **28,** 1106.9 (2014).
94. Lesniewski, L. A. *et al.* Aging compounds western diet-associated large artery endothelial dysfunction in mice: prevention by voluntary aerobic exercise. *Exp. Gerontol.* **48,** 1218–1225

(2013).

95. Boo, Y. C. *et al.* Shear stress stimulates phosphorylation of endothelial nitric-oxide synthase at Ser 1179 by Akt-independent mechanisms. *J. Biol. Chem.* **277,** 3388–3396 (2002).
96. van Popele, N. M. *et al.* Association between arterial stiffness and atherosclerosis: The Rotterdam Study. *Stroke* **32,** 454–460 (2001).
97. Van Sloten, T. T. *et al.* Local stiffness of the carotid and femoral artery is associated with incident cardiovascular events and all-cause mortality: The Hoorn Study. *J. Am. Coll. Cardiol.* **63,** 1739–1747 (2014).
98. Kaess, B. *et al.* Aortic stiffness, blood pressure progression, and incident hypertension. *JAMA* **308,** 875–881 (2012).
99. García, A., Martínez, M. & Peña, E. Viscoelastic properties of the passive mechanical behavior of the porcine carotid artery: influence of proximal and distal positions. *Biorheology* **49,** 271–288 (2012).
100. Glass, C. K. & Witztum, J. L. Atherosclerosis: the road ahead. *Cell* **104,** 503–516 (2001).
101. Hallock, P. Arterial elasticity in man in relation to age as evaluated by the pulse wave velocity method. *Arch. Intern. Med.* **54,** 770 (1934).
102. Newman, D. L. & Greenwald, S. E. in *The Arterial System* (eds. Bauerand, R. D. & Busse, R.) 109–115 (Springer, 1978).
103. Blacher, J., Asmar, R., Djane, S., London, G. M. & Safar, M. E. Aortic pulse wave velocity as a marker of cardiovascular risk in hypertensive patients. *Hypertension* **33,** 1111–1117 (1999).
104. Ravi, S. & Chaikof, E. L. Biomaterials for vascular tissue engineering. *Regen. Med.* **5,** 107–

120 (2010).

105. Khanafer, K., Schlicht, M. & Berguer, R. How should we measure and report elasticity in aortic tissue? *Eur. J. Vasc. Endovasc. Surg.* **45,** 332–339 (2013).

106. Vande Geest, J. P., Sacks, M. S. & Vorp, D. A. Age dependency of the biaxial biomechanical behavior of human abdominal aorta. *J. Biomech. Eng.* **126,** 815–822 (2004).

107. Haskett, D., Johnson, G., Zhou, A., Utzinger, U. & Vande Geest, J. Microstructural and biomechanical alterations of the human aorta as a function of age and location. *Biomech. Model. Mechanobiol.* **9,** 725–736 (2010).

108. Shafigh, M., Fatouraee, N. & Seddighi, A. S. Determining the biomechanical properties of human intracranial blood vessels through biaxial tensile test and fitting them to a hyperelastic model. *Eng. Solid Mech.* **1,** 43–56 (2013).

109. Walsh, M. T. *et al.* Uniaxial tensile testing approaches for characterization of atherosclerotic plaques. *J. Biomech.* **47,** 793–804 (2014).

110. Khanafer, K. *et al.* Determination of the elastic modulus of ascending thoracic aortic aneurysm at different ranges of pressure using uniaxial tensile testing. *J. Thorac. Cardiovasc. Surg.* **142,** 682–686 (2011).

111. Glagov, S., Zarins, C., Giddens, D. & Ku, D. Hemodynamics and atherosclerosis. Insights and perspectives gained from studies of human arteries. *Arch. Pathol. Lab. Med.* **112,** 1018–1031 (1988).

112. Atienza, J. M. Response of human coronary arteries at different mechanical conditions. in *2010 Annual International Conference of the IEEE Engineering in Medicine and Biology* 3585–3588 (IEEE, 2010).

113. Karimi, A., Navidbakhsh, M., Shojaei, A. & Faghihi, S. Measurement of the uniaxial mechanical properties of healthy and atherosclerotic human coronary arteries. *Mater. Sci. Eng. C* **33,** 2550–2554 (2013).

114. Fonck, E. *et al.* Effect of elastin degradation on carotid wall mechanics as assessed by a constituent-based biomechanical model. *Am. J. Physiol. Hear. Circ. Physiol.* **292,** H2754-2763 (2007).

115. Zhang, W., Guo, X. & Kassab, G. S. A generalized Maxwell model for creep behavior of artery opening angle. *J. Biomech. Eng.* **130,** 54502 (2008).

116. Wan, W. & Gleason, R. L. Dysfunction in elastic fiber formation in fibulin-5 null mice abrogates the evolution in mechanical response of carotid arteries during maturation. *Am. J. Physiol. - Hear. Circ. Physiol.* **304,** H674–H686 (2013).

117. Chuong, C. J. & Fung, Y. C. On residual stress in arteries. *J. Biomech. Eng.* **108,** 189–192 (1986).

118. Rehal, D., Guo, X., Lu, X. & Kassab, G. S. Duration of no-load state affects opening angle of porcine coronary arteries. *Am. J. Physiol. - Hear. Circ. Physiol.* **290,** H1871–H1878 (2006).

119. Tian, L. *et al.* Linked opening angle and histological and mechanical aspects of the proximal pulmonary arteries of healthy and pulmonary hypertensive rats and calves. *Am. J. Physiol. Hear. Circ. Physiol.* **301,** H1810–1818 (2011).

120. Protogerou, A. D., Papaioannou, T. G. & Vlachopoulos, C. Arterial stiffness mapping: a better navigation to Ithaca? *J. Am. Coll. Cardiol.* **63,** 1748–1750 (2014).

121. Cecelja, M. & Chowienczyk, P. Role of arterial stiffness in cardiovascular disease. *JRSM Cardiovasc. Dis.* **1,** cvd.2012.012016 (2012).

122. Niederhoffer, N. *et al.* Physical exercise, aortic blood pressure, and aortic wall elasticity and composition in rats. *Hypertension* **35,** 919–924 (2000).

123. Sacre, J. W., Jennings, G. L. R. & Kingwell, B. A. Exercise and dietary influences on arterial stiffness in cardiometabolic disease. *Hypertension* **63,** 888–893 (2014).

124. Safar, M. E., Levy, B. I. & Struijker-Boudier, H. Current perspectives on arterial stiffness and pulse pressure in hypertension and cardiovascular diseases. *Circulation* **107,** 2864–2869 (2003).

125. Sutton-Tyrrell, K. *et al.* Elevated aortic pulse wave velocity, a marker of arterial stiffness, predicts cardiovascular events in well-functioning older adults. *Circulation* **111,** 3384–3390 (2005).

126. Maarek, B., Simon, A. C., Levenson, J., Pithois-Merli, I. & Bouthier, J. of the atherosclerotic process in systemic hypertension poorly controlled by drug treatment. *Am. J. Cardiol.* **59,** 414–417 (1987).

127. van der Heijden-Spek, J. J. *et al.* Effect of age on brachial artery wall properties differs from the aorta and is gender dependent: a population study. *Hypertension* **35,** 637–642 (2000).

128. Kelly, R., Hayward, C., Avolio, A. & O'Rourke, M. O. Noninvasive determination of age-related changes in the human arterial pulse. *Circulation* **80,** 1652–1659 (1989).

129. Williams, R. *et al.* Noninvasive ultrasonic measurement of regional and local pulse-wave velocity in mice. *Ultrasound Med. Biol.* **33,** 1368–1375 (2007).

130. Godia, E. *et al.* Carotid artery distensibility: a reliability study. *J. Ultrasound Med.* **26,** 1157–1165 (2007).

131. MacSweeney, S. T. R., Young, G., Greenhalgh, R. M. & Powell, J. T. Mechanical properties of

the aneurysmal aorta. *Br. J. Surg.* **79,** 1281–1284 (1992).

132. Selzer, R. H., Mack, W. J., Lee, P. L., Kwong-Fu, H. & Hodis, H. . Improved common carotid elasticity and intima-media thickness measurements from computer analysis of sequential ultrasound frames. *Atherosclerosis* **154,** 185–193 (2001).
133. Gamble, G., Zorn, J., Sanders, G., MacMahon, S. & Sharpe, N. Estimation of arterial stiffness, compliance, and distensibility from M-mode ultrasound measurements of the common carotid artery. *Stroke* **25,** 11–16 (1994).
134. Reneman, R. S., Van Merode, T., Hick, P., Muytjens, A. M. M. & Hoeks, A. P. G. Age-related changes in carotid artery wall properties in men. *Ultrasound Med. Biol.* **12,** 465–471 (1986).
135. Tozzi, P., Corno, A. & Hayoz, D. Definition of arterial compliance. *Am. J. Physiol. Circ. Physiol.* **278,** H1407 (2000).
136. Zieman, S. J., Melenovsky, V. & Kass, D. a. Mechanisms, pathophysiology, and therapy of arterial stiffness. *Arterioscler. Thromb. Vasc. Biol.* **25,** 932–943 (2005).
137. Giannattasio, C. *et al.* Impaired radial artery compliance in normotensive subjects with familial hypercholesterolemia. *Atherosclerosis* **124,** 249–260 (1996).
138. Mann, A. B. in *Nanotribology and Nanomechanics* (ed. Bhushan, B.) 575–622 (Springer-Verlag, 2007).
139. Binnig, G. & Quate, C. F. Atomic force microscope. *Phys. Rev. Lett.* **56,** 930–933 (1986).
140. Zhong, Q., Inniss, D., Kjoller, K. & Elings, V. B. Fractured polymer/silica fiber surface studied by tapping mode atomic force microscopy. *Surf. Sci. Lett.* **290,** L688–L692 (1993).
141. Hurley, D. C. in *Applied Scanning Probe Methods XI: Scanning Probe Microscopy Techniques* (eds. Avouris, P. et al.) 99–100 (Springer-Verlag, 2009).

142. Radmacher, M. Measuring the elastic properties of biological samples with the AFM. *IEEE Eng. Med. Biol. Mag.* **16,** 47–57 (1997).

143. Costa, K. D. & Yin, F. C. Analysis of indentation: implications for measuring mechanical properties with atomic force microscopy. *J. Biomech. Eng.* **121,** 462–471 (1999).

144. E. Leckband, D. Novel functions and binding mechanisms of carbohydrate-binding proteins determined by force measurements. *Curr. Protein Pept. Sci.* **12,** 743–759 (2011).

145. Chtcheglova, L. A., Wildling, L., Waschke, J., Drenckhahn, D. & Hinterdorfer, P. AFM functional imaging on vascular endothelial cells. *J. Mol. Recognit.* **23,** 589–596 (2010).

146. Peloquin, J., Huynh, J., Williams, R. M. & Reinhart-King, C. A. Indentation measurements of the subendothelial matrix in bovine carotid arteries. *J. Biomech.* **44,** 815–821 (2011).

147. Hertz, H. Tiber die beriihrung fester elastischer korper (On the contact of elastic solids). *J. für die reine und Angew. Math.* **95,** 156–171 (1881).

148. Mahaffy, R. E., Shih, C. K., MacKintosh, F. C. & Käs, J. Scanning probe-based frequency-dependent microrheology of polymer gels and biological cells. *Phys. Rev. Lett.* **85,** 880–883 (2000).

149. Beenakker, J.-W. M., Ashcroft, B. A., Lindeman, J. H. N. & Oosterkamp, T. H. Mechanical properties of the extracellular matrix of the aorta studied by enzymatic treatments. *Biophys. J.* **102,** 1731–1737 (2012).

150. Hayenga, H. N., Trache, A., Trzeciakowski, J. & Humphrey, J. D. Regional atherosclerotic plaque properties in ApoE-/-mice quantified by atomic force, immunofluorescence, and light microscopy. *J. Vasc. Res.* **48,** 495–504 (2011).

151. Marzec, K. M. *et al.* Visualization of the biochemical markers of atherosclerotic plaque with

the use of Raman, IR and AFM. *J. Biophotonics* **7,** 744–756 (2014).

152. Grant, C. A. & Twigg, P. C. Pseudostatic and dynamic nanomechanics of the tunica adventitia in elastic arteries using atomic force microscopy. *ACS Nano* **7,** 456–464 (2013).
153. Lundkvist, A. *et al.* Viscoelastic properties of healthy human artery measured in saline solution by AFM-based indentation technique. *Mater. Res. Soc.* **436,** 353–358 (1997).
154. Kusche-Vihrog, K. *et al.* C-reactive protein makes human endothelium stiff and tight. *Hypertension* **57,** 231–237 (2011).
155. Lee, S. Y. *et al.* Probing the mechanical properties of TNF-alpha stimulated endothelial cell with atomic force microscopy. *Int. J. Nanomedicine* **6,** 179–195 (2011).
156. Kasas, S. & Dietler, G. Probing nanomechanical properties from biomolecules to living cells. *Pflügers Arch. Eur. J. Physiol.* **456,** 13–27 (2008).
157. Lu, L., Oswald, S. J., Ngu, H. & Yin, F. C.-P. Mechanical properties of actin stress fibers in living cells. *Biophys. J.* **95,** 6060–6071 (2008).
158. Sarangapani, K. K., Marshall, B. T., McEver, R. P. & Zhu, C. Molecular stiffness of selectins. *J. Biol. Chem.* **286,** 9567–9576 (2011).
159. Preiner, J., Ebner, A., Chtcheglova, L., Zhu, R. & Hinterdorfer, P. Simultaneous topography and recognition imaging: physical aspects and optimal imaging conditions. *Nanotechnology* **20,** 215103–215111 (2009).
160. Oliver, W. C. & Pharr, G. M. Measurement of hardness and elastic modulus by instrumented indentation: advances in understanding and refinements to methodology. *J. Mater. Res.* **19,** 3–20 (2004).
161. Ebenstein, D. M. & Pruitt, L. A. Nanoindentation of biological materials. *Nanotoday* **1,** 26–

33 (2006).

162. Ebenstein, D. M., Coughlin, D., Chapman, J., Li, C. & Pruitt, L. A. Nanomechanical properties of calcification, fibrous tissue, and hematoma from atherosclerotic plaques. *J. Biomed. Mater. Res. - Part A* **91,** 1028–1037 (2009).
163. Hemmasizadeh, A., Autieri, M. & Darvish, K. Multilayer material properties of aorta determined from nanoindentation tests. *J. Mech. Behav. Biomed. Mater.* **15,** 199–207 (2012).
164. Hanna, M. A. *et al.* Structural remodeling of coronary resistance arteries: effects of age and exercise training. *J. Appl. Physiol.* **117,** 616–623 (2014).
165. Fischer-Cripps, A. C. *Nanoindentation*. (Springer New York, 2002).
166. Johnson, K. L. One hundred years of Hertz contact. *Proc. Inst. Mech. Eng.* **196,** 363–378 (1982).
167. Oliver, W. C. & Pharr, G. M. An improved technique for determining hardness and elastic modulus using load and displacement sensing indentation experiments. *J. Mater. Res.* **7,** 1564–1583 (1992).
168. Johnson, K. L., Kendall, K. & Roberts, A. D. Surface energy and the contact of elastic solids. *Proc. R. Soc. London. Ser. A* **324,** 301–313 (1971).
169. Kohn, J. C. & Ebenstein, D. M. Eliminating adhesion errors in nanoindentation of compliant polymers and hydrogels. *J. Mech. Behav. Biomed. Mater.* **20,** 316–326 (2013).
170. Matsumoto, T., Abe, H., Ohashi, T., Kato, Y. & Sato, M. Local elastic modulus of atherosclerotic lesions of rabbit thoracic aortas measured by pipette aspiration method. *Physiol. Meas.* **23,** 635–648 (2002).

171. Sato, M., Matsumoto, T. & Ohashi, T. in *Human Biomechanics and Injury Prevention* (eds. Kajzer, J., Tanaka, E. & Yamada, H.) 147–148 (Springer, 2000).

172. Shao, J. Y., Ting-Beall, H. P. & Hochmuth, R. M. Static and dynamic lengths of neutrophil microvilli. *Proc. Natl. Acad. Sci. U. S. A.* **95,** 6797–6802 (1998).

173. Aoki, T., Ohashi, T., Matsumoto, T. & Sato, M. The pipette aspiration applied to the local stiffness measurement of soft tissues. *Ann. Biomed. Eng.* **25,** 581–587 (1997).

174. Gu, Q. *et al.* Chronic aerobic exercise training attenuates aortic stiffening and endothelial dysfunction through preserving aortic mitochondrial function in aged rats. *Exp. Gerontol.* **56,** 37–44 (2014).

175. Greenwald, S. E. Ageing of the conduit arteries. *J. Pathol.* **211,** 157–172 (2007).

176. Shadwick, R. E. Mechanical design in arteries. *J. Exp. Biol.* **202,** 3305–3313 (1999).

177. Díez, J. in *Atherosclerosis, Large Arteries and Cardiovascular Risk* (eds. Safar, M. & Frohlich, E.) **44,** 76–95 (2007).

178. Schlatmann, T. J. M. & Becker, A. E. Histologic changes in the normal aging aorta: implications for dissecting aortic aneurysm. *Am. J. Cardiol.* **39,** 13–20 (1977).

179. Wang, M. *et al.* Aging increases aortic MMP-2 activity and angiotensin II in nonhuman primates. *Hypertension* **41,** 1308–1316 (2003).

180. Bonnema, D. D. *et al.* Effects of age on plasma matrix metalloproteinases (MMPs) and tissue inhibitor of metalloproteinases (TIMPs). *J. Card. Fail.* **13,** 530–540 (2007).

181. Yasmin *et al.* Matrix metalloproteinase-9 (MMP-9), MMP-2, and serum elastase activity are associated with systolic hypertension and arterial stiffness. *Arterioscler. Thromb. Vasc. Biol.* **25,** 372–378 (2005).

182. Keyes, J. T., Haskett, D. G., Utzinger, U., Azhar, M. & Vande Geest, J. P. Adaptation of a planar microbiaxial optomechanical device for the tubular biaxial microstructural and macroscopic characterization of small vascular tissues. *J. Biomech. Eng.* **133,** 75001 (2011).

183. Nosaka, T., Tanaka, H., Watanabe, I., Sato, M. & Matsuda, M. Influence of regular exercise on age-related changes in arterial elasticity: mechanistic insights from wall compositions in rat aorta. *Can. J. Appl. Physiol.* **28,** 204–212 (2003).

184. Fleenor, B. S. *et al.* Sodium nitrite de-stiffening of large elastic arteries with aging: role of normalization of advanced glycation end-products. *Exp. Gerontol.* **47,** 588–594 (2012).

185. Goldin, A., Beckman, J. A., Schmidt, A. M. & Creager, M. A. Advanced glycation end products: sparking the development of diabetic vascular injury. *Circulation* **114,** 597–605 (2006).

186. Schleicher, E. D., Wagner, E. & Nerlich, A. G. Increased accumulation of the glycoxidation product N(epsilon)-(carboxymethyl)lysine in human tissues in diabetes and aging. *J. Clin. Invest.* **99,** 457–468 (1997).

187. Sims, T. J., Rasmussen, L. M., Oxlund, H. & Bailey, A. J. The role of glycation cross-links in diabetic vascular stiffening. *Diabetologia* **39,** 946–951 (1996).

188. Dyer, D. G. *et al.* Accumulation of Maillard reaction products in skin collagen in diabetes and aging. *J. Clin. Invest.* **91,** 2463–2469 (1993).

189. Henson, G. D., Walker, A. E., Reihl, K. D., Donato, A. J. & Lesniewski, L. A. Dichotomous mechanisms of aortic stiffening in high-fat diet fed young and old B6D2F1 mice. *Physiol. Rep.* **2,** e00268 (2014).

190. Grossin, N. *et al.* Dietary CML-enriched protein induces functional arterial aging in a RAGE-

dependent manner in mice. *Mol. Nutr. Food Res.* **59,** 927–938 (2015).

191. Kislinger, T. *et al.* N(episoln)-carboxymethyl lysine adducts of proteins are ligands for receptor for advanced glycation end products that activate cell signaling pathways and modulate gene expression. *J. Biol. Chem.* **274,** 31740–31749 (1999).
192. Posch, K. *et al.* Glycated low-density lipoprotein attenuates shear stress-induced nitric oxide synthesis by inhibition of shear stress-activated L-arginine uptake in endothelial cells. *Diabetes* **48,** 1331–1337 (1999).
193. Tanaka, S., Avigad, G., Brodsky, B. & Eikenberry, E. F. Glycation induces expansion of the molecular packing of collagen. *J. Mol. Biol.* **203,** 495–505 (1988).
194. Simard, E. *et al.* Receptor for advanced glycation end-products signaling interferes with the vascular smooth muscle cell contractile phenotype and function. *PLoS One* **10,** e0128881 (2015).
195. Coughlan, M. T. *et al.* RAGE-induced cytosolic ROS promote mitochondrial superoxide generation in diabetes. *J. Am. Soc. Nephrol.* **20,** 742–752 (2009).

CHAPTER 2

COOPERATIVE EFFECTS OF MATRIX STIFFNESS AND FLUID SHEAR STRESS ON ENDOTHELIAL CELL BEHAVIOR

This chapter includes sections from a published article in Biophysical Journal.[1] The shear exposure setup for this study was developed by Dennis Zhou and the RhoA activation kit was run by François Bordeleau.

2.1 Abstract

Arterial hemodynamic shear stress and blood vessel stiffening both significantly influence the arterial endothelial cell (EC) phenotype and atherosclerosis progression, and both have been shown to signal through cell-matrix adhesions. However, the cooperative effects of fluid shear stress and matrix stiffness on ECs remain unknown. To investigate these cooperative effects, we cultured bovine aortic ECs on hydrogels matching the elasticity of the intima of compliant, young, or stiff, aging arteries. The cells were then exposed to laminar fluid shear stress of 12 dyn/cm^2. Cells grown on more compliant matrices displayed increased elongation and tighter EC-cell junctions. Notably, cells cultured on more compliant substrates also showed decreased RhoA activation under laminar shear stress. Additionally, nitric oxide production was enhanced in ECs cultured on more compliant substrates. Together, our results demonstrate that a signaling cross talk between stiffness and fluid shear stress exists within the vascular microenvironment, and, importantly, matrices mimicking young and healthy blood vessels can promote and augment the

atheroprotective signals induced by fluid shear stress. These data suggest that targeting intimal stiffening and/or the EC response to intima stiffening clinically may improve vascular health.

2.2 Introduction

Mechanotransduction within the cardiovascular system is well studied but still not fully understood. It is well established that hemodynamic shear stress regulates atherosclerosis progression and the arterial endothelial cell (EC) phenotype.[2,3] However, the shear stress studies conducted to date have largely been performed on ECs cultured on plastic or glass,[4–6] which have significantly different compositions and mechanical properties compared with human vascular tissue.[7] Evidence is now emerging that changes in vessel stiffness that occur with age, metabolic disorders, and atherosclerosis can promote an atherosclerotic phenotype in the cells within the vessel wall.[7–10] Increased matrix stiffness from 2.5 to 10 kPa (mimicking age-related stiffening of the EC matrix) induces increased endothelium permeability and leukocyte transmigration, both of which are hallmarks of atherosclerosis progression.[7] Although both fluid shear stress and matrix stiffness are implicated in atherosclerosis progression and signal through many of the same intracellular pathways,[11,12] it is not yet known whether these mechanical cues can act synergistically to affect EC health.

Laminar arterial-level shear stress (10–30 dyn/cm^2) is associated with an atheroprotective EC phenotype and causes ECs to align and elongate in the flow direction,[2] which is hypothesized to minimize EC resistance to fluid shear stress.[13] In contrast, ECs exposed to low and oscillatory shear stress (<4 dyn/cm^2), which is prevalent at atherosclerosis-prone arterial bifurcations,

remain in a cobblestone-like formation.[6] Fluid shear stress also affects multiple intracellular signaling pathways that can be atheroprotective. Notably, many of these pathways signal through focal adhesion kinase (FAK),[12] which has also been shown to be activated in response to increased matrix stiffness.[14] Among the signaling molecules mediated by FAK, extracellular signal-regulated kinase (Erk1/2),[12] and endothelial nitric oxide synthase (eNOS)[15] play key roles in vascular homeostasis. eNOS is responsible for producing the vasodilator nitric oxide (NO),[4,5,16] which has multiple atheroprotective effects. Laminar fluid shear stress is also known to activate both Erk1/2 and eNOS in ECs cultured on plastic or glass.[4,17–19] Additionally, both ERK and eNOS have been shown to respond to mechanical stretch,[20,21] suggesting that they are sensitive to mechanical cues from the extracellular matrix. ERK can mediate EC health by downregulating Rho-associated protein kinase (ROCK),[22] whereas eNOS phosphorylation has been shown to respond to ROCK activity,[23] suggesting that matrix stiffness, which is known to affect the Rho-ROCK pathway, may influence shear-induced ERK and eNOS activity. Specifically, RhoA is affected by matrix stiffness, and helps to mediate actin reorganization.[7,24]

Here, we investigated the cooperative effects of matrix stiffness and fluid shear stress on EC health, with a specific focus on RhoA activation and NO production. Our data indicate that compliant substrates mimicking the stiffness of young, healthy arteries upregulate shear-induced NO production. Additionally, RhoA activation is upregulated after one hour of shear flow on stiff substrates mimicking the stiffness of aged, diseased arteries.

2.3 Materials and Methods

Hydrogel preparation and cell culture: Polyacrylamide (PA) gels were prepared as described previously[7,25] and functionalized with 0.1 mg/mL rat tail collagen type I (BD Biosciences). Bovine aortic ECs (BAECs) between passages 6 and 12 were seeded on the PA gels of 2.5 or 10 kPa, or onto collagen-coated glass. The hydrogel substrates were chosen to mimic the mechanical properties of the subendothelial matrix in young and aged blood vessels.[7,26] Samples were maintained with M199 media (Invitrogen) supplemented with 10% FetalClone III (HyClone) and 1% each of minimum essential media (MEM) amino acids (Invitrogen), MEM vitamins (Medtech), and penicillin-streptomycin (Invitrogen). Samples were used at a minimum of 1 day post-confluence.

Shear exposure setup: Three Brookfield DV-II+ Pro Viscometer and the CPE-40 cone (0.8°, 48 mm diameter) were validated as laminar shear stress models as shown by previous studies.[27,28] The viscometers were first warmed to 37± 2°C using a circulating water bath and hot plate. They were then sterilized by thoroughly washing with Microcide (Global Biotechnologies), 70% ethanol, and sterile water. To minimize evaporation, KimWipes (VWR) were then taped onto the ceiling of the viscometer interior using double-sided tape (Scotch), and very thoroughly saturated with sterile water to humidify the viscometer. Dextran was added to the L-15 media at 29 mg/mL and thoroughly dissolved at 37°C for one hour with rocking to achieve a viscosity of 4 cP on the day of the experiment. The cone was then sterilized again using 70% ethanol, fastened inside the viscometer, and moved upwards by 0.325 mm (the glass coverslip is ~0.155 mm thick, and the gel is ~0.130 mm thick). The bottom of the 40 mm diameter coverslip was then dried quickly, and

inverted onto 6 µL of silicone oil viscosity standard (Brookfield Engineering), which was well-spread on top of a thin ~35 mm diameter circular layer of vacuum grease (Dow Corning) (Figure 2.1). After ensuring that the coverslip adhered to the viscometer plate, 1.5 mL of L-15 media with dextran was gently added inside the viscometer. In addition, small droplets of sterile PBS were placed on the sides of the viscometer interior, to help humidify the setup. After 5 minutes, the L15 media was aspirated to wash out any residual M199 media from the sample, and 3.2 mL of L15 media with dextran was gently added inside the viscometer. The culture media was replaced as often as needed to prevent evaporation for both the sheared and static control samples during the 24 hours of shear stress exposure. Static controls cultured with hydrophobic pen residue on the coverslip bottom were also placed inside L15 media with dextran inside a well-humidified incubator at 37°C and atmospheric CO_2 levels.

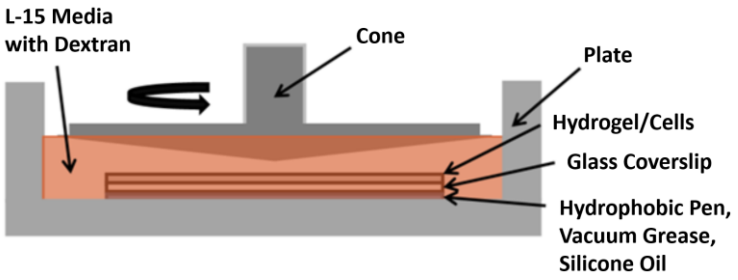

Figure 2.1: Cone-and-Plate Viscometer Schematic. Before transferring the sample to the viscometer, the viscometer cone and plate were thoroughly cleaned with microcide, 70% ethanol, and sterile deionized water. Vacuum grease and silicone oil were spread onto the plate to form a thin hydrophobic layer. The sample was then placed on top of this thin hydrophobic layer, and the hydrophobic coating on the coverslip's bottom edge helped "seal" the sample in-place, to prevent sample detachment during the 24 hours of shear stress exposure. L15 media

with dextran supplement to increase media viscosity was used for all fluid shear stress experiments. This figure was originally created by Dennis Zhou.

Cell exposure to prolonged shear: Phase images were taken on a Zeiss Axiovert 40 C with a Zeiss AxioCam b/w, 412-311 camera before and after the shear stress exposure. Samples underwent either static culture or shear of 12 dyn/cm^2 in L-15 media for 24 hours. Afterwards, the samples were gently washed twice in phosphate buffered saline (PBS), and immediately fixed in 3.7% formaldehyde. Cells were washed in 1% Triton X-100 and blocked with 4% bovine serum albumin. Actin was stained with Alexa Flour 568 phalloidin (Invitrogen), and nuclei were stained with 4',6-diaminido-2-phenylindole (DAPI) (Sigma-Aldrich). Images were captured on a Zeiss Axio Observer.Z1m microscope with a Hamamatsu ORCA-ER camera.

Rho activation: Samples underwent 0, 10, or 60 min of 12 dyn/cm^2 shear. The BAECs were washed once with ice-cold phosphate-buffered saline (PBS) and lysed with ice-cold modified radioimmunoprecipitation assay (RIPA) buffer (150 mM sodium chloride, 50 mM Tris-hydrochloride, 0.5% sodium deoxycholate, 0.1% sodium dodecyl sulfate, 1% Nonidet P40, 25 mM sodium fluoride, 1 mM sodium orthovanadate, 1:100 dilution of protease inhibitor cocktail; Sigma-Aldrich). Cell lysates were analysed for intracellular BAEC RhoA activity using a RhoA G-LISA kit (Cytoskeleton, Denver, CO) according to the manufacturer's protocol.

NO quantification: DAF-FM diacetate (4-amino-5-methylamino-2',7'-difluorofluorescein diacetate; Molecular Probes, Eugene, OR) was used to detect intracellular NO. DAF-FM diacetate

is non-fluorescent until it crosses the cell membrane and becomes DAF-FM, and then interacts with NO to become a fluorescent benzotriazole.[29,30] Cells were treated with 12 dyn/cm^2 of shear stress or static culture for 3 h prior to 10 μM of DAF-FM diacetate incubation. The dye was incubated for 30 min in 37°C and 5% CO_2, and then the samples were rinsed with PBS and incubated in M199 media for 15 min. Samples were imaged on a Zeiss LSM700 inverted laser scanning confocal microscope with a 10× objective (Carl Zeiss, Oberkochen, Germany). For all samples, a 488 nm laser was used to image 40.2 μm-deep sections for each sample. Twenty fields of view were taken per sample, and brightfield microscopy was used to ensure that the approximate cell count in each field of view was the same. Unstained cells were imaged to determine background fluorescence, which was subtracted from the fluorescent intensity values. Experiments were normalized over the range of fluorescent intensity values from the sheared glass sample in each experimental group, and data are presented where the control glass value was set to 0.5.

Statistical analysis: All analyses were performed using GraphPad Prism 5 (GraphPad Software, La Jolla, CA) or Excel 2010 (Microsoft, Redmond, WA). Student's t-tests or parametric one-way or two-way analysis of variance (ANOVA) with post hoc Tukey's honest significance test were performed where appropriate, and p-values < 0.05 were considered statistically significant.

2.4 Results

To investigate the role of matrix stiffness in fluid shear stress-induced EC realignment, PA substrates mimicking young and aged arteries were seeded with ECs and placed in a cone-and-

plate viscometer. 24 hours of shear stress also induced actin reorganization, which aligns in the direction of the shear flow (Figure 2.2).

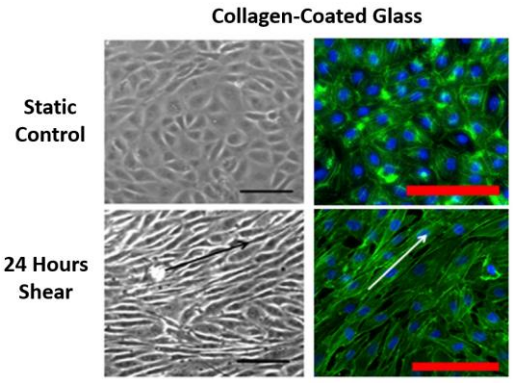

Figure 2.2: Matrix stiffness influences EC morphology under fluid shear stress. Representative phase contrast and fluorescence images of ECs before and after shear stress exposure for 24 h at 12 dyn/cm^2. Actin fiber (green) and DAPI (blue) staining, showing reorganization of the actin network parallel to the flow direction. Arrows indicate approximate flow direction and the black/red scale bars are 100 mm.

To explore the mechanism by which EC-cell junctions are stabilized by compliant matrices and fluid shear stress, we focused on Rho-mediated signaling. The Rho/ROCK pathway has emerged as a mediator of EC barrier integrity and is strongly dependent on matrix stiffness.[31,32] Activation of RhoA is required for actin reorganization and EC alignment under laminar fluid shear stress.[24] Our data indicate that significant RhoA activation is present after 60 min of fluid shear stress for ECs cultured on stiff 10 kPa and glass substrates (Figure 2.3), as previously shown for ECs cultured on glass.[33] Notably, RhoA activation is significantly attenuated on the compliant 2.5 kPa hydrogels after 60 min of fluid shear stress.

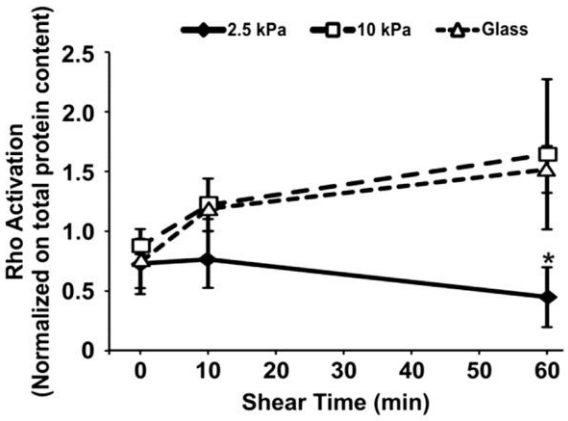

Figure 2.3: RhoA activation of ECs after 10 or 60 min of shear (12 dyn/cm^2) or static culture. EC RhoA activation is greater on stiffer matrices at 60 min. Data are mean ± SE, five replicates. $*p < 0.05$, Tukey's test, compared with 10 kPa and glass samples. Shear exposure and cell lysates collection was completed by Julie Kohn and the RhoA activation kit was run by François Bordeleau.

To further explore whether these early signaling events result in physiological changes in the ECs, we measured NO production in response to shear stress as a function of matrix stiffness. Our data indicate that after 3 h of fluid shear stress, NO production is elevated in response to fluid shear and this response is enhanced on more compliant matrices (Figure 2.4). These data suggest that compliant matrices augment the atheroprotective effects of fluid shear stress on ECs by increasing NO production.

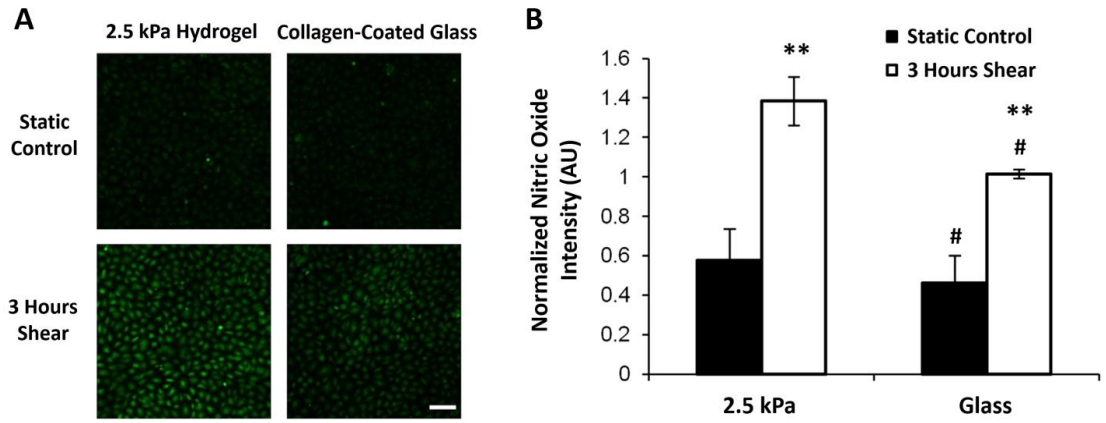

Figure 2.4: Matrix stiffness influences NO production induced by fluid shear stress. (A) Representative fluorescent images of ECs on 2.5 kPa gels or on collagen-coated glass stained with DAF-FM diacetate after 12 dyn/cm^2 shear stress exposure for 3 h or static conditions. Scale bar, 100 µm. (B) Fluorescence quantification of samples normalized to glass shear from each experiment (mean ± SE, n = 3 control samples and n = 5 sheared samples, 20 fields of view per sample). #$p < 0.005$ and $**p < 0.02$ (Student's t-test).

2.5 Discussion

Together, our results demonstrate a strong interplay between laminar fluid shear stress and matrix stiffness that affects EC health and function, and may contribute to atheroprone and atheroprotective EC phenotypes. Although the process of EC elongation and alignment to fluid shear stress is not fully understood, Rho GTPase activity and cell traction stresses are known to modulate cell elongation and alignment.[24] An initial increase in RhoA is needed for ECs under fluid shear to form stress fibers and for cells to orient in the flow direction. A decline in RhoA is then required for the cells to spread and elongate directionally.[34] It was previously shown that decreased matrix stiffness results in decreased RhoA activity,[7] and we demonstrate that this

trend also occurs under fluid shear stress. Our data support this model for the role of Rho in EC realignment to flow, where ECs elongate on compliant substrates and exhibit reduced RhoA activity. Since RhoA is known to mediate EC cell morphology,[11,33,35] the lower RhoA values on the 2.5 kPa matrix may allow for increased EC elongation.

Our previous work indicates that ECs form tighter cell-cell junctions on more compliant matrices, strengthening the junctions and inducing an atheroprotective phenotype.[7] Recent evidence suggests that cells tend to move in the direction of principal stresses (normal to the cell-cell junction) to avoid shearing along each other.[36] We speculate that the compliant 2.5 kPa substrates used in our system may provide the optimal amount of Rho activation to allow cells to elongate without providing such strong cell-cell adhesion that the cells are inhibited from moving adjacent to each other during the alignment process.

Previous studies have shown that ERK and eNOS phosphorylation is affected by fluid shear stress.[4,17–19] Nitric oxide itself is also upregulated with fluid shear stress application.[37] NO is also influenced by age, where shear generates greater levels of NO production in young aortas than in aged aortas.[38] Here, our data show an increase in shear-induced NO production following shear stress on compliant matrices more than on stiff matrices. Our data demonstrate that matrix stiffness, which changes with age,[7] plays an important role in understanding the effects of shear-induced NO production. It is also important to note that we collected our data using steady flow. It is likely that physiological, pulsatile flow may augment an atheroprone response even further.

2.6 Conclusions

Although the atheroprotective role of fluid shear stress is well documented, we demonstrate that matrix compliance also has an atheroprotective role that synergizes with fluid shear stress. When cultured on more compliant matrices under laminar fluid shear stress, ECs exhibit decreased Rho activation and increased nitric oxide production. Our results reveal a critical role of matrix mechanics in mediating the EC response to fluid shear stress, and underscore the need to create more physiologically relevant models to study cell mechanotransduction.

2.7 References

1. Kohn, J. C., Zhou, D. W. (co-first authors), *et al.* Cooperative effects of matrix stiffness and fluid shear stress on endothelial cell behavior. *Biophys. J.* **108,** 471–478 (2015).
2. Malek, A. M. & Izumo, S. Mechanism of endothelial cell shape change and cytoskeletal remodeling in response to fluid shear stress. *J. Cell Sci.* **109,** 713–726 (1996).
3. Zaragoza, C., Márquez, S. & Saura, M. Endothelial mechanosensors of shear stress as regulators of atherogenesis. *Curr. Opin. Lipidol.* **23,** 446–452 (2012).
4. Boo, Y. C. *et al.* Shear stress stimulates phosphorylation of endothelial nitric-oxide synthase at Ser 1179 by Akt-independent mechanisms. *J. Biol. Chem.* **277,** 3388–3396 (2002).
5. Jo, H. *et al.* Differential effect of shear stress on extracellular signal-regulated kinase and N-terminal Jun kinase in endothelial cells. *J. Biol. Chem.* **272,** 1395–1401 (1997).
6. Chien, S. Effects of disturbed flow on endothelial cells. *Ann. Biomed. Eng.* **36,** 554–562 (2008).
7. Huynh, J. *et al.* Age-related intimal stiffening enhances endothelial permeability and leukocyte transmigration. *Sci. Transl. Med.* **3,** 112ra122 (2011).

8. Isenberg, B. C., DiMilla, P. A., Walker, M., Kim, S. & Wong, J. Y. Vascular smooth muscle cell durotaxis depends on substrate stiffness gradient strength. *Biophys. J.* **97,** 1313–1322 (2009).
9. Peyton, S. R. & Putnam, A. J. Extracellular matrix rigidity governs smooth muscle cell motility in a biphasic fashion. *J. Cell. Physiol.* **204,** 198–209 (2005).
10. Huynh, J., Bordeleau, F., Kraning-Rush, C. M. & Reinhart-King, C. A. Substrate stiffness regulates PDGF-induced circular dorsal ruffle formation through MLCK. *Cell. Mol. Bioeng.* **6,** 138–147 (2013).
11. Tzima, E. Role of small GTPases in endothelial cytoskeletal dynamics and the shear stress response. *Circ. Res.* **98,** 176–185 (2006).
12. Li, S. *et al.* Fluid shear stress activation of focal adhesion kinase. *J. Biol. Chem.* **272,** 30455–30462 (1997).
13. Whited, B. M. & Rylander, M. N. The influence of electrospun scaffold topography on endothelial cell morphology, alignment, and adhesion in response to fluid flow. *Biotechnol. Bioeng.* **111,** 184–195 (2014).
14. Paszek, M. J. *et al.* Tensional homeostasis and the malignant phenotype. *Cancer Cell* **8,** 241–254 (2005).
15. Koshida, R. *et al.* Role of focal adhesion kinase in flow-induced dilation of coronary arterioles. *Arterioscler. Thromb. Vasc. Biol.* **25,** 2548–2553 (2005).
16. Li, H., Horke, S. & Förstermann, U. Vascular oxidative stress, nitric oxide and atherosclerosis. *Atherosclerosis* **237,** 208–219 (2014).
17. Kimura, H. *et al.* EGF positively regulates the proliferation and migration, and negatively regulates the myofibroblast differentiation of periodontal ligament-derived endothelial

progenitor cells through MEK/ERK-and JNK-dependent signals. *Cell. Physiol. Biochem.* **32,** 899–914 (2013).

18. Sumpio, B. E. *et al.* MAPKs (ERK1/2, p38) and AKT can be phosphorylated by shear stress independently of platelet endothelial cell adhesion molecule-1 (CD31) in vascular endothelial cells. *J. Biol. Chem.* **280,** 11185–11191 (2005).
19. Bretón-Romero, R. *et al.* Critical role of hydrogen peroxide signaling in the sequential activation of p38 MAPK and eNOS in laminar shear stress. *Free Radic. Biol. Med.* **52,** 1093–1100 (2012).
20. Laboureau, J., Dubertret, L., Lebreton-de Coster, C. & Coulomb, B. ERK activation by mechanical strain is regulated by the small G proteins rac-1 and rhoA. *Exp. Dermatol.* **13,** 70–77 (2004).
21. Takeda, H. *et al.* Bi-phasic activation of eNOS in response to uni-axial cyclic stretch is mediated by differential mechanisms in BAECs. *Life Sci.* **79,** 233–239 (2006).
22. Mavria, G. *et al.* ERK-MAPK signaling opposes Rho-kinase to promote endothelial cell survival and sprouting during angiogenesis. *Cancer Cell* **9,** 33–44 (2006).
23. Ming, X.-F. *et al.* Rho GTPase/Rho kinase negatively regulates endothelial nitric oxide synthase phosphorylation through the inhibition of protein kinase B/Akt in human endothelial cells. *Mol. Cell. Biol.* **22,** 8467–8477 (2002).
24. Shiu, Y.-T. *et al.* Rho mediates the shear-enhancement of endothelial cell migration and traction force generation. *Biophys. J.* **86,** 2558–2565 (2004).
25. Califano, J. P. & Reinhart-King, C. A. A balance of substrate mechanics and matrix chemistry regulates endothelial cell network assembly. *Cell. Mol. Bioeng.* **1,** 122–132 (2008).

26. Peloquin, J., Huynh, J., Williams, R. M. & Reinhart-King, C. A. Indentation measurements of the subendothelial matrix in bovine carotid arteries. *J. Biomech.* **44,** 815–821 (2011).
27. Sdougos, H. P., Bussolari, S. R. & Dewey, C. F. Secondary flow and turbulence in a cone-and-plate device. *J. Fluid Mech.* **138,** 379–404 (1984).
28. Fewell, M. E. & Hellums, J. D. The secondary flow of Newtonian fluids in cone-and-plate viscometers. *Trans. Soc. Rheol.* **21,** 535–565 (1977).
29. Kojima, H. *et al.* Detection and imaging of nitric oxide with novel fluorescent indicators: diaminofluoresceins. *Anal. Chem.* **70,** 2446–2453 (1998).
30. Kojima, H. *et al.* Development of a fluorescent indicator for nitric oxide based on the fluorescein chromophore. *Chem. Pharm. Bull.* **46,** 373–375 (1998).
31. Wojciak-Stothard, B. & Ridley, A. J. Shear stress-induced endothelial cell polarization is mediated by Rho and Rac but not Cdc42 or PI 3-kinases. *J. Cell Biol.* **161,** 429–439 (2003).
32. Birukova, A. A. *et al.* Endothelial barrier disruption and recovery is controlled by substrate stiffness. *Microvasc. Res.* **87,** 50–57 (2013).
33. Tzima, E., Del Pozo, M. A., Shattil, S. J., Chien, S. & Schwartz, M. A. Activation of integrins in endothelial cells by fluid shear stress mediates Rho-dependent cytoskeletal alignment. *EMBO J.* **20,** 4639–4647 (2001).
34. Barauna, V. G., Mantuan, P. R., Magalhães, F. C., Campos, L. C. G. & Krieger, J. E. AT1 receptor blocker potentiates shear-stress induced nitric oxide production via modulation of eNOS phosphorylation of residues Thr495 and Ser1177. *Biochem. Biophys. Res. Commun.* **441,** 713–719 (2013).
35. Wojciak-Stothard, B. & Ridley, A. J. Rho GTPases and the regulation of endothelial

permeability. *Vascul. Pharmacol.* **39,** 187–199 (2002).

36. Trepat, X. & Fredberg, J. J. Plithotaxis and emergent dynamics in collective cellular migration. *Trends Cell Biol.* **21,** 638–646 (2011).

37. Wessells, H. *et al.* Fluid shear stress-induced nitric oxide production in human cavernosal endothelial cells: inhibition by hyperglycaemia. *Br. J. Urol. Int.* **97,** 1047–1052 (2006).

38. Soucy, K. G. *et al.* Impaired shear stress-induced nitric oxide production through decreased NOS phosphorylation contributes to age-related vascular stiffness. *J. Appl. Physiol.* **101,** 1751–1759 (2006).

CHAPTER 3

MECHANICAL HETEROGENEITIES IN THE SUBENDOTHELIAL MATRIX DEVELOP WITH AGE AND DECREASE WITH EXERCISE

This chapter includes sections from a published article in the Journal of Biomechanics.[1] Mouse body weights were recorded by Adeline Chen and Stephanie Cheng. Creation of the linear mixed effects model for this study and statistical analysis of spatial heterogeneity was performed by Daniel R. Kowal.

3.1 Abstract

Arterial stiffening occurs with age and is associated with lack of exercise. Notably both age and lack of exercise are major cardiovascular risk factors. While it is well established that bulk arterial stiffness increases with age, more recent data suggest that the intima, the innermost arterial layer, also stiffens during aging. Micro-scale mechanical characterization of individual layers is important because cells primarily sense the matrix that they are in contact with and not necessarily the bulk stiffness of the vessel wall. To investigate the relationship between age, exercise, and subendothelial matrix stiffening, atomic force microscopy was utilized here to indent the subendothelial matrix of the thoracic aorta from young, aged-sedentary, and aged-exercised mice, and elastic modulus values were compared to conventional pulse wave velocity measurements. The subendothelial matrix elastic modulus was elevated in aged-sedentary mice compared to young or aged-exercised mice, and the macro-scale stiffness of the artery was found

to linearly correlate with the subendothelial matrix elastic modulus. Notably, we also found that with age, there exists an increase in the point-to-point variations in modulus across the subendothelial matrix, indicating non-uniform stiffening. Importantly, this heterogeneity is reversible with exercise. Given that vessel stiffening is known to cause aberrant endothelial cell behavior, and the spatial heterogeneities we find exist on a length scale much smaller than the size of a cell, these data suggest that further investigation in the heterogeneity of the subendothelial matrix elastic modulus is necessary to fully understand the effects of physiological matrix stiffening on cell function.

3.2 Introduction

Risk factors for the development of cardiovascular disease (CVD) include increased age and lack of exercise,[2] and risk is assessed clinically using macro-scale mechanical measurements. The standard clinical methodology to measure vessel stiffness and predict CVD is pulse wave velocity (PWV) testing, which is typically performed using ultrasound.[3–5] PWV values have been shown to increase with age and decrease with exercise.[6–8] However, while PWV is important in the prediction of the development of CVD,[4] it does not provide information on the mechanical properties of individual layers of the blood vessel or measurements at a scale at which cells sense. Cells are known to respond to matrix stiffness[9,10] and their response to stiffening has been linked to vessel permeability and leukocyte transmigration,[11–13] hallmarks of atherosclerosis. Therefore, micro-scale elastic modulus measurement is necessary since macro-scale mechanical measurements do not provide a complete picture of subendothelial mechanics.

To measure the micro-scale properties of tissues, measurement techniques such as atomic force microscopy (AFM) have been implemented to probe the individual layers of the artery at the sub-micron level.[14–16] Previously, we used AFM to demonstrate that intimal arterial extracellular matrix (ECM) stiffness increases with age[11] and due to a high fat, high sugar diet.[17] However, these studies focused on the mean mechanics of the subendothelial matrix and did not account for the complex spatial heterogeneities within the artery. Based on these and other similar studies, the predominant in vitro models used to study endothelial cell (EC) response to stiffness use primarily gels of homogeneous stiffness.[10,12,15,18,19] However, cells are known to respond to heterogeneous matrix cues and display heterogeneous traction forces.[20] The artery is a complex mechanical environment, and therefore we propose that the subendothelial matrix will display heterogeneous mechanical profiles, and that measuring these potential heterogeneities with respect to cardiovascular risk factors will allow us to better understand the mechanical environment ECs face *in vivo*.

Here, we characterize the mechanical variations in the elastic modulus of the subendothelial matrix as a function of age and exercise, two critical factors that affect the progression of atherosclerosis.[2,11,17,21] Our data indicate that increased vessel stiffening with age is accompanied by an increase in spatial heterogeneities in elastic modulus, and exercise decreases this heterogeneity.

3.3 Materials and Methods

Animal groups: All animal treatments and experiments were carried out under Cornell University's Institutional Animal Care and Use Committee guidelines. C57Bl/6 male mice were obtained from the National Institute on Aging at 2 or 18 months of age. Mice were allowed to acclimate for 1-2 weeks before treatment. During treatment mice were weighed 5 times per week, and control and experimental groups were housed in the same cage.

Exercise treatment: Mice were separated into exercise groups based on arrival date at the facility. Chronic swimming regimens have been shown to provide the typical adaptations of cardiac exercise to the neuromuscular and cardiovascular systems.[22] An 8-week forced swim regimen was used with up to 5 mice per tank. Swimming was chosen for the exercise regimen due to the ease of material obtainability and its known ability to affect the cardiovascular system.[22] Swimming also provides a set amount of exercise to all animal cohorts, unlike voluntary wheel running which can provide different exercise treatments to aged animals.[23] In an earlier pilot study which assessed swim regimen length, 8 weeks was determined to be the amount of exercise time necessary to cause a significant decrease in PWV for C57Bl/6 mice (data not shown). To minimize stress levels in the animals, prior to the first week of swimming the mice were acclimated to the tank with three 3-min swimming sessions, as has been shown to familiarize mice to this technique.[22] Mice then swam 5 days per week for 10 minutes during the first week, 30 min per day for weeks 2-3, and 45 min per day for weeks 4-8. During treatments, all mice were monitored for bobbing, "gang swimming," or exhaustion, and they were dried after swimming.

Pulse wave velocity: PWV readings were recorded for each mouse before and after the exercise treatment. Mice were shaved on the abdomen and the upper back/neck regions a few days prior to ultrasound measurements. Mice were anesthetized with isoflurane, where the heart rate was maintained from 400-500 BPM, and the body temperature and electrocardiogram (ECG) were constantly monitored. Doppler ultrasound was performed using a Vevo2100 with an MS550D transducer to measure transit time at abdominal and thoracic aorta locations. Abdominal readings were made with the animal supine and thoracic readings were made with the animal prone. Doppler readings with at least 5 heart beat cycles were recorded for each mouse. The arrival time was calculated between the velocity upstroke and the peak of the R-wave and measured at thoracic and abdominal aorta locations. The transit time was calculated as the difference between the two arrival times as previously described.[24] PWV was calculated as the distance measured over the animal's body divided by the transit time.

Aorta preparation: Mice were anesthetized with 2-4% isoflurane until they were unresponsive. The chest cavity was then opened and the heart was perfused with 10 mL of phosphate buffered saline (PBS). The thoracic aorta was excised, cleaned of excess tissue, and stored in PBS on ice. Immediately prior to beginning AFM mechanical testing, the thoracic aorta was cut longitudinally, the ECs were scraped off as previously described,[16] and the tissue was bonded (Loctite Super Glue) to a petri dish and covered with room temperature PBS.

Atomic force microscopy: Contact mode AFM (Asylum MFP-3D) was used to measure the subendothelial matrix elastic modulus of the thoracic aorta samples after the ECs were removed. Measurements were taken in a 100 by 100 μm area of the artery in an 11x11 point grid with indents occurring every 10 μm. Indentations were made 300-500nm into the tissue using a 5μm radius spherical polystyrene bead on a silicon nitride cantilever with a spring constant of 0.12 N/m as calibrated by the manufacturer (Novascan Technologies). The AFM tips were calibrated before measuring each aorta sample and had a mean spring constant of 0.19 ± 0.03 N/m. The data was fit to the Hertz model assuming a Poisson's ratio of 0.5[16,17] using the Asylum curve fitting software to determine the elastic modulus.

Statistics: Group comparisons of the PWV data were conducted using the Student's t-test for normally distributed data and the Wilcoxon Rank-Sum test for non-normally distributed data, where normality was determined using a Shapiro-Wilk test (JMP software) with statistical significance at a p-value less than 0.05. Mean AFM data was analyzed using analysis of variance (ANOVA) to compare more than two groups and the empirical cumulative distribution functions of the AFM data were compared pair-wise using the Kolmogorov-Smirnov test with p-values less than 0.05. Error bars are presented as standard error of the mean (SEM).

To characterize the effects of age and exercise on arterial mechanics, and in particular the spatial heterogeneity of the elastic modulus maps, we created an additive statistical model.[25] The additive model was represented as a linear mixed effects model with age and exercise group effects and calculations were completed with R software, using the mgcv package.[26] The elastic

modulus values were square-root-transformed to satisfy normality of the residuals. From the linear mixed effects model, spatial heterogeneity was calculated using a smoothing parameter, the inverse of the variance of the random effects term.[27] A large smoothing parameter for an elastic modulus map represents smoother, more linear values, where a smaller value indicates a rougher elastic modulus map. The smoothing parameter provides a more direct spatial heterogeneity measurement than sample variance. The bootstrap was used to estimate the sampling distribution of the log-transformed smoothing parameter values.[28] Mouse-level bootstrap re-samplings were performed to assess the spatial heterogeneity of subendothelial matrix stiffness values within each mouse.

3.4 Results

Mice were separated into treatment groups and showed no body weight change

Aged (18 months old at the beginning of the study) and young (2 months old at the beginning of the study) mice were used for age treatment groups, and the aged mice were separated into aged-sedentary (Aged Sed) and aged-exercised (Aged Ex) groups, which underwent a swimming regimen for 8 weeks (Figure 3.1A). All mice were weighed 5 days per week to ensure stress on the animal was minimized as indicated by maintenance of a healthy weight (Figure 3.1B).

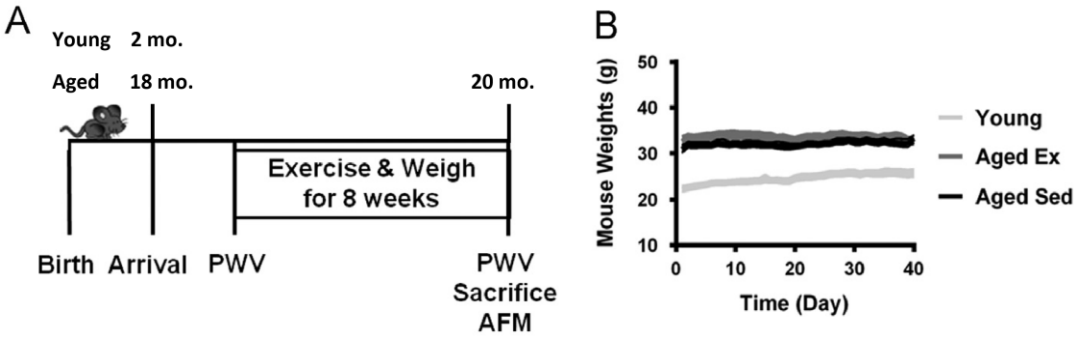

Figure 3.1: Schematic of timeline of experimental procedures. (A) Mice were received at Cornell, and given time to acclimate prior to the exercise regimen. PWV measurements were taken before and after exercise. AFM measurements were taken after sacrifice. (B) Weights of mice throughout the experimental timeline. Lines represent mean and SEM.

Macro-scale arterial stiffening increases with age, decreases with exercise treatment, and is linearly correlated with subendothelial matrix elastic modulus

PWV is a measurement of bulk artery stiffness and is the standard clinical metric for predicting CVD.[4] Here, PWV measurements of male C57Bl/6 mice were made using Doppler ultrasound and the transit time method, where the arrival time at each location was measured between the peak of the R-wave on the ECG and the upstroke of the velocity profile (Figure 3.2A) as previously described.[24] PWV measurements of young (2 months old) and aged (18 months old) mice taken before the exercise regimen indicate an increase in bulk arterial stiffness with age (Figure 3.2B) as previously shown.[6] Aged mice were divided into exercised and sedentary groups, and following an 8-week swimming exercise regimen, PWV was shown to decrease in aged mice (20 months old) compared to sedentary mice of the same age (Figure 3.2C). These results demonstrate the prescribed exercise regimen described in Fig. 1 cause changes in the bulk stiffness of arteries.

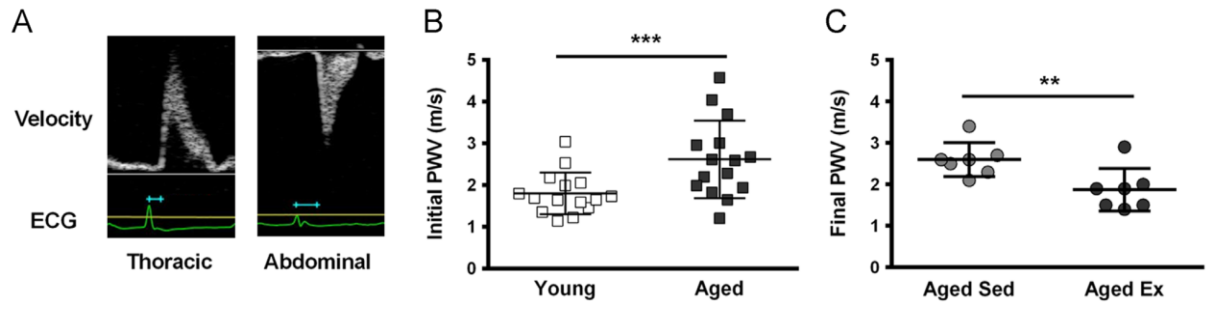

Figure 3.2: Macro-scale stiffness increases with age and decreases with exercise. (A) Representative Doppler ultrasound images used to measure the transit time between the thoracic and abdominal aorta. The arrival times at each location are shown in blue. (B) PWV measurements in aged mice (18 months old, n = 15 mice) relative to young mice (2 months old, n = 14 mice), *** $p < 0.005$ (Student's t-test). (C) PWV measurements in aged-sedentary mice (20 months old, n = 7 mice) and aged-exercised mice (20 months old, n = 7 mice) taken after an exercise regimen performed by half of the aged mice, ** $p < 0.02$ (Wilcoxon-Rank Sum test).(For interpretation of the references to color in this figure legend, the reader is referred to the web version of this article.)

Micro-scale elastic modulus increases with age and decreases with exercise in aged mice

Although bulk stiffness of large arteries is assessed clinically, this information provides very little information about the mechanics of individual layers of the artery. Recent evidence from our lab and others has demonstrated that the mechanical environment of the intimal ECM dictates EC function and health[9,11–13] underscoring the need to understand subendothelial matrix mechanics. Here, we used AFM coupled with a spherical probe and shallow indentations to produce force-distance curves analyzed using the Hertz model as previously described.[16] We validated the Hertz

model in our system based on the goodness of fit, as shown in an example plot of the Hertz model fit to the data and the residuals of this fit (Figure 3.3A). AFM was used to create elastic modulus maps of the subendothelial matrix along the thoracic aorta by profiling 100 by 100 µm tissue sections, from young (4 months old), aged-sedentary (20 months old), and aged-exercised (20 months old) mice. This dimension was chosen because it is of sufficient size to provide the detail necessary to define the spatial distribution of elastic modulus beneath multiple cells in a monolayer. Average values across the grid indicate that subendothelial matrix elastic modulus increases with age and decreases with exercise in aged mice (Figure 3.3B). The PWV measurements were plotted against the AFM results, indicating there is a positive and linear correlation between macro- and micro-scale elastic modulus (Figure 3.3C).

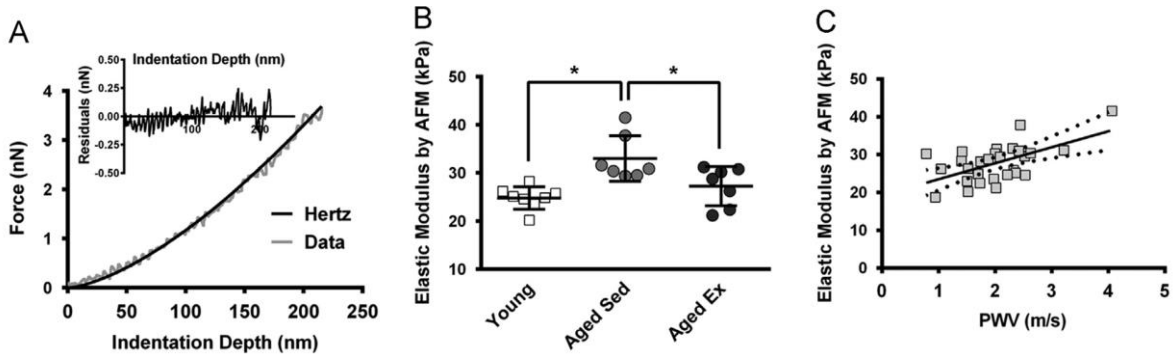

Figure 3.3: Micro-scale elastic modulus increases with age and decreases with exercise. (A) Representative Hertz model fit to AFM force-indentation curve, and inset shows the residuals of the Hertz model fit to the data. (B) The mean elastic modulus of the subendothelial matrix in aged-sedentary mice (20 months old, n = 7 mice) relative to young mice (4 months old, n = 8 mice) and aged-exercised mice (20 months old, n = 7 mice) based on AFM measurements, * $p < 0.01$ (Linear Mixed Effects Model, square-root transform). (C) Comparison of PWV macro-

scale stiffness with micro-scale AFM elastic modulus values from each mouse, $p < 0.02$ (Linear Mixed Effects Model). The solid line indicates the linear fit and the dotted lines indicate the standard error.

Elastic modulus heterogeneity increases with age and decreases with exercise in aged mice

Typically, nano- and micro-indentation measurements of tissues have been reported as mean values (Figure 3.3B).[11,14,17,29] However, most tissues, including the intima, are complex, and it is known that cells can respond to heterogeneous cues in matrix stiffness.[10,20] Using AFM, we probed the subendothelial matrix every 10 µm over a 100 by 100 µm space. Examination of the distribution of AFM values reveals that qualitative differences exist between the elastic modulus values in aged-sedentary (20 months old) mice compared to aged-exercised (20 months old) and young (4 months old) mice (Figure 3.4A). The frequency of high elastic modulus values within the subendothelial matrix (above 50kPa) is increased with age and decreased with exercise in aged mice (Figure 3.4B). The empirical cumulative distribution functions of AFM elastic modulus values are changed with age and exercise in aged mice, demonstrating a larger spread of elastic modulus values in aged-sedentary mice compared to young mice or to aged-exercised mice (Figure 3.4C). Overall, these data indicate that there is an increase in heterogeneity of mechanical elastic modulus values with age that can be reversed with exercise. These results suggest that the subendothelial matrix is more mechanically complex than previously thought.

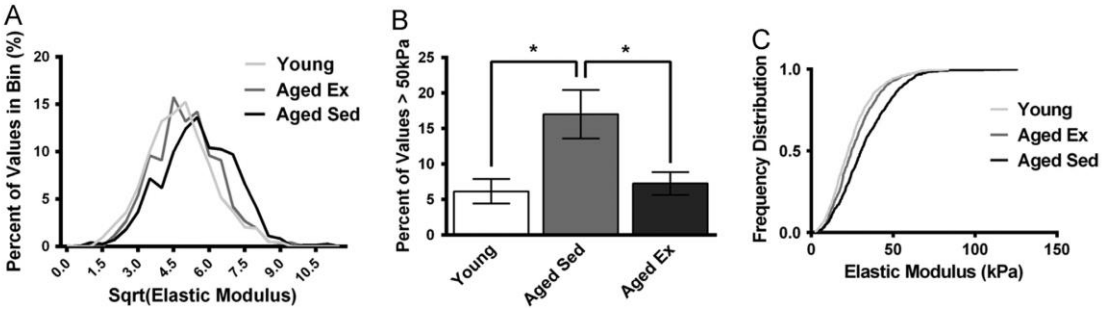

Figure 3.4: Range of AFM elastic modulus values increases with age and decreases with exercise. (A) Representative stiffness heterogeneity profiles of the aortic intima demonstrate heterogeneous distributions where young and aged-exercised mice have a more positive skew (square-root transform). (B) Plot of AFM measurement values greater than 50 kPa in aged-sedentary mice compared to young and aged-exercised mice, * $p < 0.05$ (ANOVA), error bars SEM. (C) The empirical cumulative distribution functions of the spread of values of the aged-sedentary mice compared to both the young and the aged-exercised mice ($p < 0.0001$, pair-wise comparisons using the Kolmogorov–Smirnov test).

Spatial micro-heterogeneities of elastic modulus increase with age and decrease with exercise

Our data indicate that there is an overall increase in the variations in mechanical measurements in the subendothelial matrix of aged-sedentary (20 months old) mice compared to young (4 months old) or aged-exercised (20 months old) mice. To investigate the spatial dependence of these heterogeneities, we used AFM to create one stiffness profile or 'map' on the thoracic aorta for each mouse in a random location. To create these maps, indents were made every 10 µm over a 100 by 100 µm area of the tissue. These maps were displayed on an 'x' and 'y' coordinate system to help visualize the spatial heterogeneity, and the 'z' axis displays the elastic modulus at that specific location. Spatial heterogeneity profiles of aortic subendothelial matrix demonstrate

complex patterns of elastic modulus 'hotspots' in the aged-sedentary mice (Figure 3.5A). To determine how the locations of elastic modulus 'hotspots' varied between experimental cohorts, we employed a linear mixed effects model. The linear mixed effects model with mouse-specific spatial effects was estimated from the square-root-transformed elastic modulus data, which satisfies normality of the residuals. The sampling distributions of the group differences in log-smoothing parameters were estimated using 1000 bootstrap simulations. Among sedentary mice, the log-smoothing parameters were lower for aged-sedentary mice than young mice in 95% of the bootstrap simulations (Figure 3.5B). Among aged mice, the log-smoothing parameters were lower for aged-sedentary mice in 92% of the bootstrap simulations than for the aged-exercised mice (Figure 3.5C). Together these data indicate that the model predicts that spatial heterogeneity increases with age and decreases with exercise in aged mice.

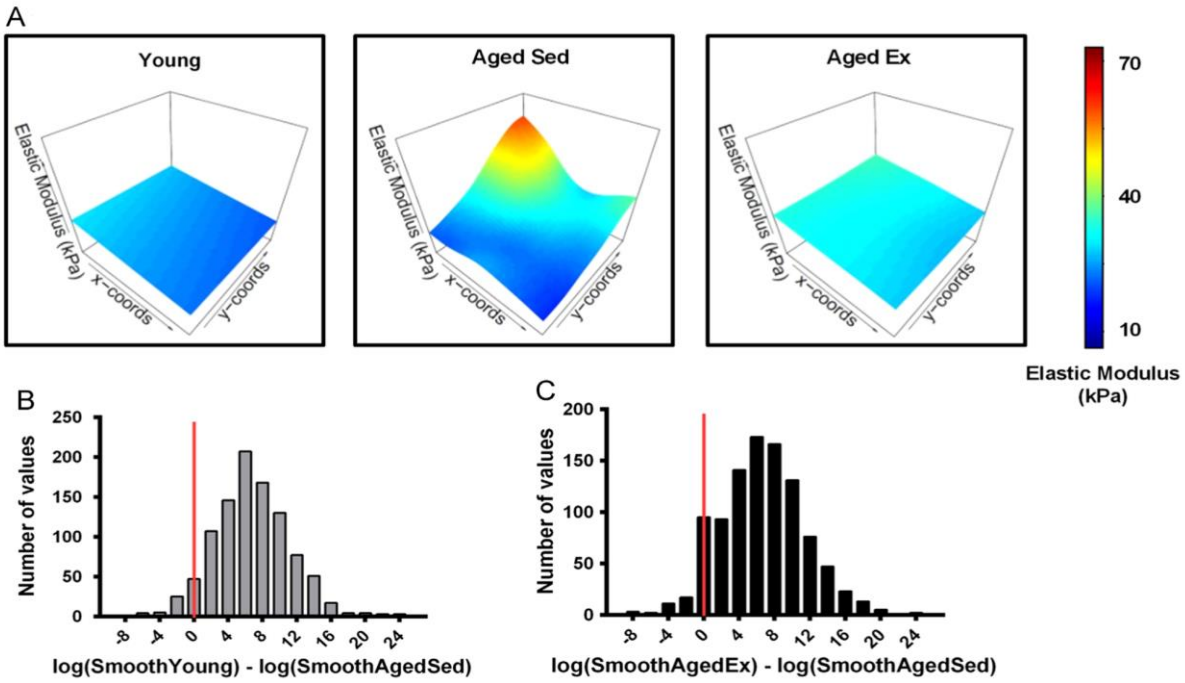

Figure 3.5: The spatial heterogeneity of elastic modulus values in the mouse aorta increases with age and decreases with exercise. (A) Representative AFM elastic modulus maps of a 100 by 100 µm aorta sections, where the 'z' axis values represent the elastic modulus found at each 'x' and 'y' coordinate of the intima. These plots demonstrate 'hotspots' of increased elastic modulus in the aged-sedentary mice and complex spatial patterns of increased elastic modulus. Histograms of bootstrap simulations of the smoothing parameter for the AFM measurements of the (B) aged-sedentary mice compared to young mice, and (C) aged-sedentary mice compared to aged-exercised mice (Linear Mixed Effects Model, log transform) indicate that the spatial heterogeneity of subendothelial matrix stiffness increases with age and decreases with exercise in aged mice. Data to the right of the red line indicate simulations where the aged-sedentary mice have more spatial heterogeneity than the compared group. Daniel R. Kowal performed the bootstrap simulations and created the images for this figure.

3.5 Discussion

Here, we show that the elastic modulus profiles of the mouse aortic subendothelial matrix are more complex than previously reported, and this complexity is a function of age and exercise. The elastic modulus measured using an AFM within a 100 μm by 100 μm patch can vary from 2 to 100 kPa. Heterogeneity in elastic modulus increases with age and decreases with exercise, and importantly, the spatial variation of these values also follows the same trend. These data indicate that aged-sedentary mice contain subendothelial matrix profiles that are more mechanically complex than those of young or aged-exercised mice. Our data also indicate that the increase in mean micro-scale elastic modulus with age and decrease with exercise correlates with macro-scale PWV measurements. PWV measures bulk artery stiffness, which is thought to be influenced in most part by the thick medial layer.[30] This measurement does not account for the complexities of mechanical micro-heterogeneities found using AFM. Our data indicate that PWV, the current gold standard clinical technique, may also give an indication of mean micro-scale intimal health. Arterial stiffness has been shown to increase with increased collagen deposition, the degradation of elastin fibers, and the action of crosslinking agents such as advanced glycation end products (AGEs).[31,32] Collagen is a major contributor to the mechanical properties of the artery, and the increased presence of collagen fibers in the artery over elastin fibers contributes to bulk arterial stiffening.[33,34] As arteries age, collagen production increases and elastin content decreases, leading to an increase in overall arterial stiffness.[7,35,36] Exercise has the opposite effect on arterial composition, resulting in more compliant vessels.[7] Increased stiffness in arteries from aged mice is also likely partly due to the increased presence of ECM cross-linkers such as AGEs,[31] which are mitigated with exercise.[37] The underlying causes of increased mechanical heterogeneities

describe in our study are not yet clear. It is possible that they are due to increased collagen aggregation[38,39] and/or changes in collagen cross-linking. While artery fiber composition has been studied in relation to age and exercise[7,40,41] less is known about specific micro-scale changes in the subendothelial matrix at the scale at which AFM is detecting. Further studies are required to determine the specific physical and biochemical changes which cause the increase in heterogeneity we report here.

PWV is the gold standard for measuring macro-scale artery stiffness due to its clinical accessibility and application as a strong predictor of CVD.[3–5] High aortic PWV in humans is associated with a 48% increase in CVD risk.[4] Our data confirm reports from others indicating PWV increases with age and decrease with exercise in rodents.[6,7] Ours is the first study to our knowledge to show that macro- and micro-scale stiffness measurements in the artery are linearly correlated. Together with our previous data demonstrating that matrix stiffness can induce EC dysfunction,[9,11] these data suggest that that clinical evaluation of the artery using PWV could provide information about subendothelial matrix mechanics and EC health. The assessment of subendothelial matrix and EC function using macro-scale techniques may allow for new insights into cardiovascular health and the relationship between arterial stiffness and disease progression.

Based on our data, the elastic modulus of the subendothelial matrix can range over an order of magnitude, indicating that ECs experience a non-uniform, complex mechanical environment in vivo. It is well known that ECs respond to the mechanical properties of their matrix.[9,13,42] Matrix

stiffness can regulate EC traction forces, contractility, and F-actin stress fiber formation through Rho/ROCK/MLCK signaling.[11,13,42–45] AFM elastic modulus maps described here indicate that aged-sedentary mice have more heterogeneous elastic modulus profiles. Recently, single cell studies have demonstrated that cells exert heterogeneous traction forces in response to a heterogeneous ECM.[20] Importantly, higher cellular traction forces have been shown to result in centripetal cellular tension that disrupts of EC-EC contacts, causing the formation of gaps in the EC monolayer.[11,12,46] Given the known role of matrix stiffness in the regulation of cellular traction forces and the role of traction force in preserving monolayer integrity, it is likely that more complex mechanical elastic modulus profiles like those we describe here may result in increased disruption of barrier function with age. Our results underscore the need for the development of novel *in vitro* platforms that accurately reflect the micro-heterogeneities in elastic modulus present in the subendothelial matrix and a need to better understand how cells integrate multiple mechanical cues.

3.6 Conclusions

While much is known about bulk arterial stiffness, here we demonstrate that micro-scale subendothelial matrix elastic modulus also is affected by age and exercise. Importantly, the subendothelial matrix stiffens due to age heterogeneously, and these effects are mediated by exercise. Not only does the subendothelial matrix become more heterogeneous, but the spatial heterogeneity of the elastic modulus values also increases with age and decrease following an exercise regimen.

3.7 References

1. Kohn, J. C. *et al.* Mechanical heterogeneities in the subendothelial matrix develop with age and decrease with exercise. *J. Biomech.* **49,** 1447–1453 (2016).
2. Grundy, S. M., Pasternak, R., Greenland, P., Smith, S. & Fuster, V. Assessment of cardiovascular risk by use of multiple-risk-factor assessment equations. *Circulation* **100,** 1481–1492 (1999).
3. Laurent, S. *et al.* Expert consensus document on arterial stiffness: methodological issues and clinical applications. *Eur. Heart J.* **27,** 2588–2605 (2006).
4. Van Bortel, L. M. *et al.* Expert consensus document on the measurement of aortic stiffness in daily practice using carotid-femoral pulse wave velocity. *J. Hypertens.* **30,** 445–448 (2012).
5. Mitchell, G. F. *et al.* Arterial stiffness and cardiovascular events: the Framingham Heart Study. *Circulation* **121,** 505–511 (2010).
6. Di Lascio, N., Stea, F., Kusmic, C., Sicari, R. & Faita, F. Non-invasive assessment of pulse wave velocity in mice by means of ultrasound images. *Atherosclerosis* **237,** 31–37 (2014).
7. Steppan, J. *et al.* Exercise, vascular stiffness, and tissue transglutaminase. *J. Am. Heart Assoc.* **3,** e000599 (2014).
8. Gu, Q. *et al.* Chronic aerobic exercise training attenuates aortic stiffening and endothelial dysfunction through preserving aortic mitochondrial function in aged rats. *Exp. Gerontol.* **56,** 37–44 (2014).
9. Lo, C. M., Wang, H. B., Dembo, M. & Wang, Y. L. Cell movement is guided by the rigidity of the substrate. *Biophys. J.* **79,** 144–152 (2000).
10. Kohn, J. C. *et al.* Cooperative Effects of Matrix Stiffness and Fluid Shear Stress on Endothelial

Cell Behavior- Supplement. *Biophys. J.* **108,** 1–6 (2015).

11. Stroka, K. M. & Aranda-Espinoza, H. Endothelial cell substrate stiffness influences neutrophil transmigration via myosin light chain kinase-dependent cell contraction. *Blood* **118,** 1632–1640 (2011).
12. Krishnan, R. *et al.* Substrate stiffening promotes endothelial monolayer disruption through enhanced physical forces. *Am. J. Physiol. Cell Physiol.* **300,** C146–C154 (2011).
13. Huynh, J. *et al.* Age-related intimal stiffening enhances endothelial permeability and leukocyte transmigration. *Sci. Transl. Med.* **3,** 112ra122 (2011).
14. Peloquin, J., Huynh, J., Williams, R. M. & Reinhart-King, C. A. Indentation measurements of the subendothelial matrix in bovine carotid arteries. *J. Biomech.* **44,** 815–821 (2011).
15. Engler, A. J., Richert, L., Wong, J. Y., Picart, C. & Discher, D. E. Surface probe measurements of the elasticity of sectioned tissue, thin gels and polyelectrolyte multilayer films: Correlations between substrate stiffness and cell adhesion. *Surf. Sci.* **570,** 142–154 (2004).
16. Klein, E. A. *et al.* Cell-cycle control by physiological matrix elasticity and in vivo tissue stiffening. *Curr. Biol.* **19,** 1511–1518 (2009).
17. Weisbrod, R. M. *et al.* Arterial stiffening precedes systolic hypertension in diet-induced obesity. *Hypertension* **62,** 1105–1110 (2013).
18. Wang, Y. L. & Pelham, R. J. J. Preparation of a flexible, porous polyacrylamide substrate for mechanical studies of cultured cells. *Methods in Enzymology* **298,** 489–496 (1998).
19. Stroka, K. M., Levitan, I. & Aranda-Espinoza, H. OxLDL and substrate stiffness promote neutrophil transmigration by enhanced endothelial cell contractility and ICAM-1. *J. Biomech.* **45,** 1828–1834 (2012).

20. Breckenridge, M. T., Desai, R. A., Yang, M. T., Fu, J. & Chen, C. S. Substrates with engineered step changes in rigidity induce traction force polarity and durotaxis. *Cell. Mol. Bioeng.* **7,** 26–34 (2014).
21. Tanaka, H. *et al.* Aging, habitual exercise, and dynamic arterial compliance. *Circulation* **102,** 1270–1275 (2000).
22. Kregel, K. *et al.* in *Resource Book for the Design of Animal Exercise Protocols* 23–57 (2006). doi:10.2460/ajvr.68.6.583
23. Fleenor, B. S., Marshall, K. D., Durrant, J. R., Lesniewski, L. A. & Seals, D. R. Arterial stiffening with ageing is associated with transforming growth factor-β1-related changes in adventitial collagen: reversal by aerobic exercise. *J. Physiol.* **588,** 3971–3982 (2010).
24. Williams, R. *et al.* Noninvasive ultrasonic measurement of regional and local pulse-wave velocity in mice. *Ultrasound Med. Biol.* **33,** 1368–1375 (2007).
25. Wood, S. N. *Generalized Additive Models: An Introduction With R*. (Chapman & Hall/CRC, 2006).
26. R Core Team. in *R Foundation for Statistical Computing* (2014).
27. Ruppert, D., Wand, M. P. & Carroll, R. J. in *Cambridge Series in Statistical and Probabilistic Mathematics (No. 12)* (eds. Gill, R., Ripley, B. D., Ross, S., Stein, M. & Williams, D.) (Cambridge University Press, 2003).
28. Efron, B. & Tibshirani, R. *An Introduction to the Bootstrap*. (CHAPMAN & HALL/CRC, 1994). doi:10.1214/ss/1063994971
29. Jacot, J. G., Dianis, S., Schnall, J. & Wong, J. Y. A simple microindentation technique for mapping the microscale compliance of soft hydrated materials and tissues. *J. Biomed. Mater.*

Res. Part A **79A,** 485–494 (2006).

30. Shadwick, R. E. Mechanical design in arteries. *J. Exp. Biol.* **202,** 3305–3313 (1999).
31. Greenwald, S. E. Ageing of the conduit arteries. *J. Pathol.* **211,** 157–172 (2007).
32. Fleenor, B. S. *et al.* Sodium nitrite de-stiffening of large elastic arteries with aging: Role of normalization of advanced glycation end-products. *Exp. Gerontol.* **47,** 588–594 (2012).
33. Díez, J. in *Blood Pressure and Arterial Wall Mechanics in Cardiovascular Diseases* (eds. Safar, M. E., O'Rourke, M. F. & Frohlich, E. D.) 205–214 (Springer-Verlag, 2014).
34. Fleenor, B. S. & Berrones, A. J. in *Arterial Stiffness: Implications and Interventions* 19–20 (Springer Internaional Publishing, 2015).
35. Kohn, J. C., Lampi, M. C. & Reinhart-King, C. A. Age-related vascular stiffening: causes and consequences. *Front. Genet.* **6,** 112 (2015).
36. Zieman, S. J., Melenovsky, V. & Kass, D. a. Mechanisms, pathophysiology, and therapy of arterial stiffness. *Arterioscler. Thromb. Vasc. Biol.* **25,** 932–943 (2005).
37. Gu, Q. *et al.* Contribution of receptor for advanced glycation end products to vasculature-protecting effects of exercise training in aged rats. *Eur. J. Pharmacol.* **741,** 186–194 (2014).
38. Keyes, J. T., Haskett, D. G., Utzinger, U., Azhar, M. & Vande Geest, J. P. Adaptation of a planar microbiaxial optomechanical device for the tubular biaxial microstructural and macroscopic characterization of small vascular tissues. *J. Biomech. Eng.* **133,** 75001 (2011).
39. Greenberg, S. R. The association of medial collagenous tissue with atheroma formation in the aging human aorta as revealed by a special technique. *Histol. Histopathol.* **1,** 323–326 (1986).
40. Schlatmann, T. J. M. & Becker, A. E. Histologic changes in the normal aging aorta: implications for dissecting aortic aneurysm. *Am. J. Cardiol.* **39,** 13–20 (1977).

41. Avolio, A., Jones, D. & Tafazzoli-Shadpour, M. Quantification of alterations in structure and function of elastin in the arterial media. *Hypertension* **32,** 170–175 (1998).

42. Hsu, B. Y., Bae, Y. H., Mui, K. L., Liu, S.-L. & Assoian, R. K. Apolipoprotein E3 inhibits Rho to regulate the mechanosensitive expression of Cox2. *PLoS One* **10,** e0128974 (2015).

43. Szulcek, R. *et al.* Localized RhoA GTPase activity regulates dynamics of endothelial monolayer integrity. *Cardiovasc. Res.* **99,** 471–482 (2013).

44. Birukova, A. A. *et al.* Endothelial barrier disruption and recovery is controlled by substrate stiffness. *Microvasc. Res.* **87,** 50–57 (2013).

45. Ridley, A. Rho family proteins: coordinating cell responses. *Trends Cell Biol.* **11,** 471–477 (2001).

46. Stroka, K. M. & Aranda-Espinoza, H. Effects of morphology vs. cell–cell interactions on endothelial cell stiffness. *Cell Mol. Bioeng.* **4,** 9–27 (2011).

CHAPTER 4

BENEFICIAL EFFECTS OF EXERCISE ON ARTERIAL STIFFNESS ARE SHORT-LIVED

This chapter includes sections from an article currently in revision.[1] Body weight data was collected by Shweta Modi, Jenny Ma, and Julian Azar. The structured illumination microscope was setup by Joseph Miller and François Bordeleau. The CML ELISA kit was run by Hannah Watkins.

4.1 Abstract

Aerobic exercise helps to maintain cardiovascular health in part by mitigating age-induced arterial stiffening. However, the long-term effects of exercise regimens on aortic stiffness remain unknown. To examine how arterial stiffening changes following exercise cessation, mice were exposed to an 8-week swimming regimen followed by an 8-week sedentary rest period. Cardiovascular stiffness was measured throughout both the exercise and rest periods. After swimming, macro-scale pulse wave velocity decreases, and after 4 weeks of rest, pulse wave velocity returns to baseline and the elastic modulus of the subendothelial matrix re-stiffens. Within the same time frame, the collagen content in the intima layer and the presence of advanced glycation end products increase. Overall, our data indicate that consistent exercise is necessary for maintaining compliant vessels.

4.2 Introduction

Increased stiffness within the vasculature is independently associated with cardiovascular disease (CVD) risk, and is often measured using pulse wave velocity (PWV), the gold standard measurement of bulk arterial stiffness.[2] Well known risk factors for CVD include increased age and lack of exercise.[3,4] Importantly, these risk factors are also associated with increased artery stiffness.[2,5,6] Changes in subendothelial matrix stiffness are associated with endothelial cell contraction, endothelial cell-cell junction disruption, and increased vessel permeability.[7,8] Previously, we showed that increased vascular stiffness in aged mice can be decreased through exercise, and that these effects span both the macro- and micro-scales.[5] However, the lasting effects of exercise on vascular stiffness after exercise cessation are unknown.

Here, aged mice underwent an 8-week exercise regimen and changes in PWV, subendothelial matrix stiffness, and cardiac ejection fraction were measured immediately following the exercise regimen and compared to values after an additional 8 weeks of rest. To investigate the underlying causes of changes in vascular stiffness, we examined collagen content in the intima and changes in advanced glycation end product (AGE) accumulation within the whole artery, as both collagen[6,9] and AGEs[10,11] are associated with arterial stiffening. To analyze AGEs, we specifically used a N(ε)-carboxymethyl-lysine (CML) ELISA kit to measure the content of this major AGE modification[23] which is known to be effected by key cardiovascular risk factors.[10,24] Our data indicate that exercise has a relatively short-lived impact on cardiovascular health when followed by exercise cessation, and these changes correlate with changes in collagen and AGEs.

4.3 Materials and Methods

Animal model: All animal experiments were carried out under approved Cornell University IACUC protocols. C57Bl/6 male mice were acquired from the National Institute on Aging at 18 months of age.

Swimming protocol: Mice were swum in groups of 2-5 mice per tank as previously described.[5] The animals were exposed to the swimming apparatus for three 3-minute swims to acclimate prior to beginning the 8-week exercise regimen. Mice swam five days a week for 10 minutes per day in week 1, 30 minutes per day in weeks 2 – 3, and 45 minutes per day for weeks 4 – 8. No animal data was collected within 12 hours after swimming.

Pulse wave velocity (PWV): A Vevo2100 ultrasound was used to measure the transit time between the thoracic and abdominal locations as previously described.[5] Each mouse was anesthetized using 0.5 – 2 % isoflurane, hair was removed, and an MS550D transducer was used to acquire Doppler images. The mouse was laid supine to acquire thoracic images and laid prone for abdominal images. The arrival times at each location were measured as the time from the peak of the R-wave on the ECG to the velocity upstroke, and the difference between arrival times was used as the transit time. A distance measurement was made over the animal's body using a ruler, and PWV was calculated as distance over time.

Ejection Fraction: Mice were anesthetized and isoflurane levels were monitored, as deep sedation can impact LVEF.[12] Following PWV measurement, the mice were laid supine and left

ventricle (LV) long-axis images were acquired at systole and diastole. The EKV (ECG-gated Kilohertz Visualization) imaging method was used to average many heart cycles and create a high-quality video of the LV expansion and contraction over one ECG cycle. Ejection fraction was determined using the Vevo2100 ultrasound after manual outlines of the chamber were made.

Blood pressure: Blood pressure was measured on a subgroup of mice using a non-invasive tail cuff (Kent Scientific) after acclimating them to a constraint cone. The cuff was set to a 20 second deflation time and the program software determined accepted measurements based on a minimum tail volume of 10 µL.

Thoracic aorta collection: At the time of animal sacrifice the thoracic aortas were collected as previously described.[5] Mice were anesthetized using 2 – 3.5 % isoflurane, the thoracic cavity was opened, and the heart was perfused with phosphate buffered saline (PBS). The thoracic aorta was excised, excess fat was removed, and the tissue was cut longitudinally and stored at 4°C in PBS until use.

Atomic force microscopy (AFM): An Asylum AFM (MFP-3D) was used to collect indentation data of the subendothelial matrix. Endothelial cells were scraped from the intima using a cotton swab as previously described,[13] and the tissue was glued to a petri dish (Loctite Super Glue). The tissue was submerged in a drop of PBS and indentations were made using a 0.12 N/m cantilever, as specified by the manufacturer (Novascan) and calibrated to 0.109 +/- 0.019 N/m before use.

Indentations were made 25 – 200 nm deep, and a range of loading rates was used to determine the force rate dependence on the elastic modulus of the tissue. The cantilever was affixed with a 10 µm diameter polystyrene bead, and the Hertz model was used to fit the force indentation curves to determine elastic modulus as previously described.[5,7,13] The tissue was assumed incompressible and a Poisson's ratio of 0.5 was used in calculations.

Collagen content: Sections of thoracic aorta were removed and fixed in 3.7 % formaldehyde for 15 minutes and stored in PBS at 4°C until use. The arteries were stained with a picrosirius red kit (Polysciences, Inc 24901) by soaking the tissue in solutions provided by the kit for 1 hour with Solution A, 3 hours with Solution B and 1 hour with Solution C. Samples were left to soak at 4°C in PBS overnight to remove any excess stain. A structured illumination microscope (SIM) built on an inverted Axiovert microscope (Zeiss) was used to measure the picrosirius red polarization signal of the intima layer. Briefly, a linear polarizer was rotated above the condenser by a linear motor actuator (Thorlabs). A 20 lines/mm Ronchi grid (Edmunds Optics) was positioned in the illumination plane above the linear polarizer and moved $2\pi/3$ for each image acquisition. A polarizer analyzer was positioned in the imaging plane with its optical axis turned 90 degree relative to the illumination polarizer (cross polarizer configuration). The intima location was determined by fluorescence signal of the VE-cadherin monolayer, stained with primary 1:100 (Santa Cruz) and secondary 1:200 (Alexaflour-488) both overnight. White light illumination was used and a sequence of 3 images under structured illumination were collected and processed by a MATLAB code to reconstruct a thin optical section of the picrosirius red polarization signal,[14] which correlates with collagen content.[15,16] The three color channels (red, green and blue) were

collected and their intensity values were measured with ImageJ software. The composite intensity value at each artery location was calculated using grayscale correction factors: 0.2989*red, 0.587*green, and 0.114*blue. Images taken on different days were normalized to a control artery and were range corrected. Data was log transformed prior to group comparisons.

Collagen content standard deviation: Composite images were created from the three grayscaled values of intima polarized signal, as described above. The standard deviation of values from within each image was measured using ImageJ software and compiled for each treatment group. Data was log transformed and values were normalized to the mean of the sedentary group for statistical analysis.

N(ε)-carboxymethyl-lysine (CML) ELISA: After thoracic aorta tissue collection, pieces of aorta approximately 1 cm long were flash frozen in liquid nitrogen and stored at -80°C until use. The night before the enzyme linked immunosorbent assay (ELISA) was run, the samples were ground using a cold mortar and pestle and dissolved in 300 µL of RIPA buffer containing 1:1000 protease inhibitor. Protein concentration of samples was assessed using a bicinchoninic acid (BCA) assay (Pierce, Thermo Scientific). Samples were evaluated for CML content using a competitive ELISA (Cell Biolabs STA-816) run according to manufacturer's instructions. CML concentration was normalized against protein concentration to determine weight percent (ng CML per mg protein for each sample).

Statistics: Data sets were assessed for normality using the Shapiro-Wilks test and a p-value of 0.05. Two groups were compared according to each time point using a Student's t-test and a p-value of 0.05 was determined to be significant. Factors were determined to be linearly correlated with a Pearson Correlation p value less than 0.05. Error bars are presented as standard error of the mean (SEM).

4.4 Results

Pulse wave velocity decreases following an 8-week exercise regimen and returns to baseline following exercise cessation

To examine the effects of exercise and subsequent exercise cessation on arterial stiffness, mice underwent an 8-week exercise regimen followed by an 8-week rest period (Figure 4.1A). Before, during, and following these periods, PWV values were recorded. At time of sacrifice, the thoracic aorta was removed and used for atomic force microscopy (AFM), AGE, and collagen analysis. Even though the mice were advanced in aged, mouse body weight remained constant over the study (Figure 4.1B), a marker of good health.

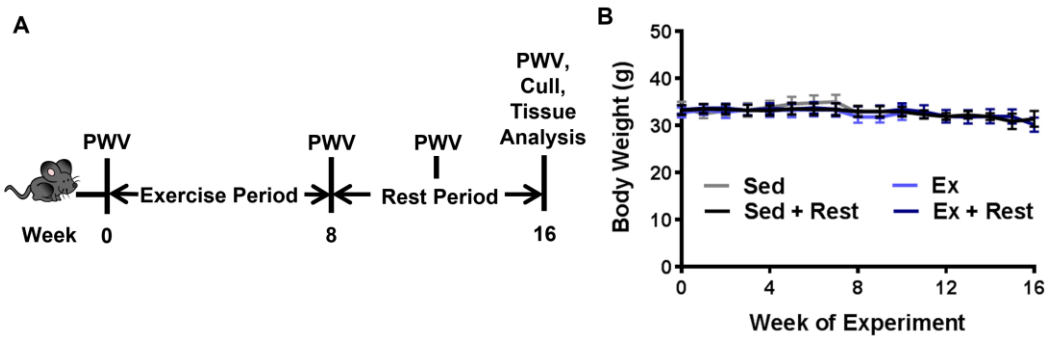

Figure 4.1: Mice undergo an exercise regimen and a rest period while body weight is monitored. (A) Aged C57Bl/6 mice swim for 8 weeks during the exercise period, and then rest for 8 weeks. Pulse wave velocity (PWV) is measured throughout the study, and at week 16 the mice are culled and their aortas are removed for further analysis. (B) Mouse body weight remains steady over the study in all groups; n = 4 – 7 mice per group; error bars are SEM. Body weight data was collected by Shweta Modi, Jenny Ma, and Julian Azar.

The 8-week exercise period did not cause significant changes in blood pressure (Figure 4.2A), a factor that is known to affect PWV readings,[17] indicating that blood pressure was not a factor in measured PWV changes. As expected, PWV values of the exercised mice significantly decreased compared to the sedentary cohort following 8-weeks of exercise. However, after 4 weeks of post-exercise rest, PWV increased to the level of the sedentary counterparts and remained elevated for the remainder of the 8-week rest period (Figure 4.2B).

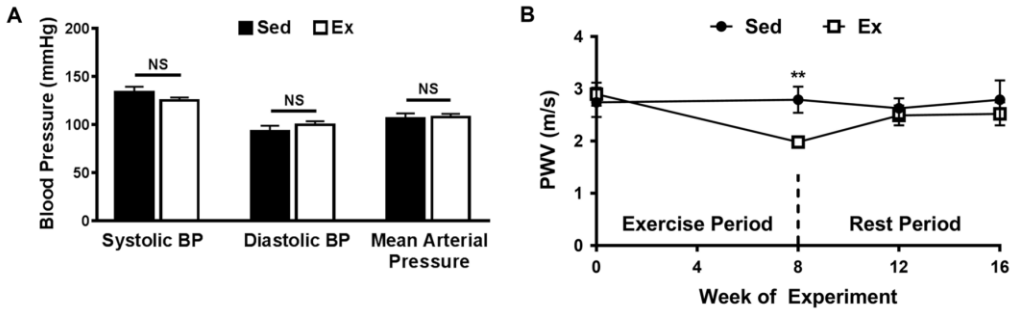

Figure 4.2: Pulse wave velocity (PWV) decreases following exercise and returns to baseline during the rest period. (A) Blood pressure was unchanged with the exercise regimen; n = 4 – 5 mice per group, NS = not statistically significant. (B) PWV from aged mice decreases after 8 weeks of exercise and increases to baseline following 4 weeks of rest; ** $p < 0.005$ (Student's t-test), n = 7 – 12 mice per data point. Error bars are SEM in the whole figure.

Subendothelial matrix stiffness is loading rate dependent

To further investigate stiffening following exercise cessation, the subendothelial matrix was probed with AFM to compare the micro-scale elastic moduli between mice cohorts that were either sedentary for 16 weeks or exercised for 8 weeks followed by 8 weeks of sedentary rest. We found that the moduli measured using AFM are loading rate dependent (Figure 4.3A). A positive correlation exists between the apparent elastic modulus and the loading rate. Representative force versus indentation curves demonstrate an increased slope at higher loading rates (Figure 4.3B). To confirm this holds true across other artery samples, measurements from several studies were plotted on the same graph (Figure 4.3C). The relationship we found between loading rate and moduli correlates with data reported from other studies measuring the subendothelial matrix elastic modulus of bovine and murine tissue.[5,7,13]

Subendothelial matrix stiffness decreases following exercise and returns to baseline following rest

To compare the micro-scale elastic moduli between mice cohorts that were either sedentary for 16 weeks or exercised for 8 weeks followed by 8 weeks of sedentary rest, we used a loading rate of approximately 16 nN/s. This loading rate was chosen because it places a maximum force of approximately 2 nN on the tissue, which is within the range of traction forces that an endothelial cell applies per contact.[18] The modulus of the subendothelial matrix decreased after exercise and re-stiffened following the rest period (Figure 4.3D). Together, the combined PWV and AFM measurements demonstrate that both macro- and micro-scale stiffness changes in the aorta due to exercise are transient.

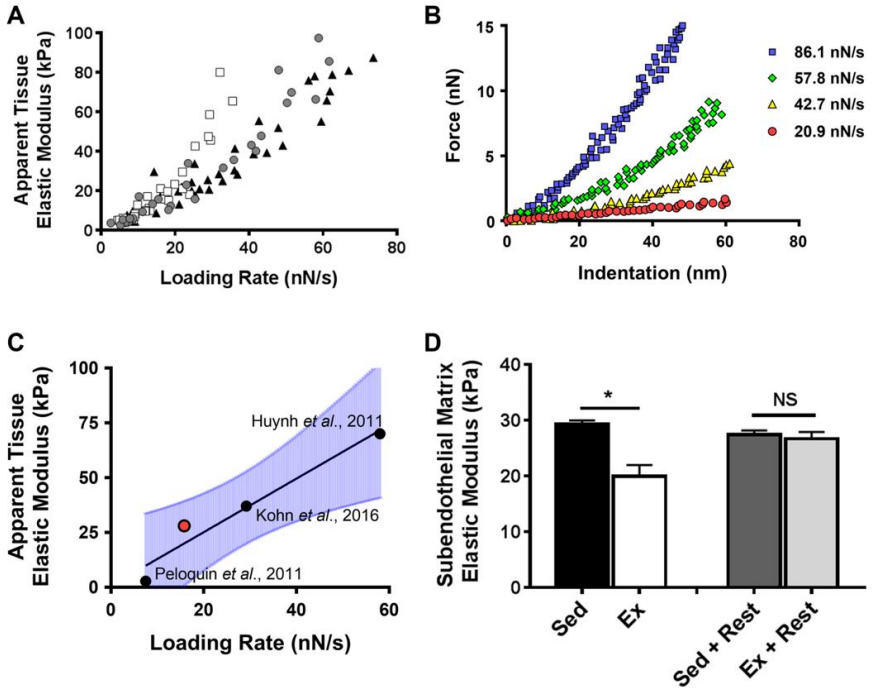

Figure 4.3: The elastic modulus of the murine aorta subendothelial matrix is loading rate dependent and is affected by exercise and rest. (A) The apparent elastic modulus of the

subendothelial matrix increases with higher loading rates, as shown in three different mice; points collected from 10 locations on each aorta, $p < 0.0005$ (Pearson Correlation). (B) Atomic force microscopy (AFM) force versus indentation curves at a representative location on a mouse aorta demonstrate a steeper slope with higher loading rates. (C) Independent studies of subendothelial matrix stiffness of the aortic intima demonstrate its loading rate dependence; white point represents data from this study. Aged murine aorta data were used for Kohn *et al*., 2016 and Huynh *et al*., 2011, and mature bovine aorta data were used for Peloquin *et al.*, 2011; significant linear trend with 95% confidence interval bands, $p < 0.05$ (Pearson Correlation). (D) Intimal stiffness decreases following an exercise regimen and returns to baseline following a rest period; * $p < 0.05$ (Student's t-test), $n = 4 – 7$ mice per group. Error bars are SEM, NS = not statistically significant.

Cardiac function improves with exercise and decreases to baseline following rest

Since cardiovascular stiffness returned to baseline rapidly after exercise cessation, we also investigated the lasting effects of exercise on other markers of cardiovascular function, including left ventricular ejection fraction (LVEF). To determine LVEF, high-resolution ultrasound EKV images were acquired and the left ventricle cross-sectional areas were measured at systole and diastole (Figure 4.4A). Exercise increased LVEF, and following the 8-week rest period, the heart returned to lower baseline function (Figure 4.4B). Following the rest period both macro-scale and micro-scale stiffness of the aorta show a negative linear correlation with LVEF (Figures 4.4C and 4.4D).

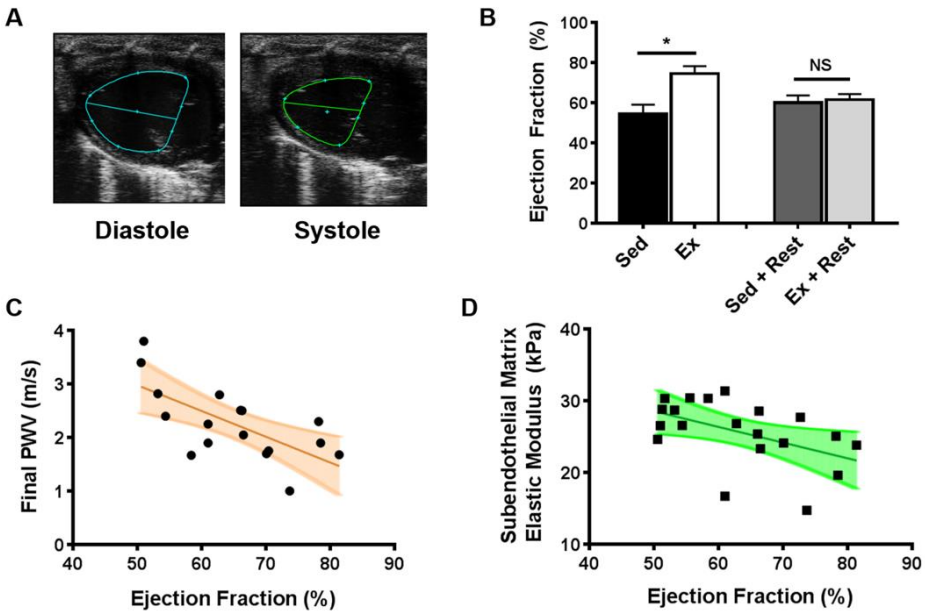

Figure 4.4: Left ventricular ejection fraction is inversely correlated with arterial stiffness. (A) Representative ultrasound images of the long-axis view of the left ventricle, used to calculate ejection fraction. (B) Ejection fraction increases with exercise and returns to baseline following a rest period; * $p < 0.05$ (Student's t-test), n = 5 – 7 mice per group, error bars are SEM. (C) There is a significant inverse correlation between PWV and ejection fraction; $p < 0.005$ (Pearson Correlation). (D) There is a significant inverse correlation between the subendothelial matrix elastic modulus and ejection fraction; $p < 0.05$ (Pearson Correlation).

Intima collagen content follows the trends of vascular stiffness

To assess the underlying causes responsible for changes in stiffness, collagen and AGE content in the thoracic aortas was assessed. Increased collagen is a major cause of increased arterial stiffness associated with advanced age,[6,9,19] and is orders of magnitude stiffer than elastin, the other major arterial extracellular matrix (ECM) protein.[20] Intimal collagen content was assessed based on the picrosirius red polarization signal assessed using structured illumination microscopy

(Figure 4.5A), which measures collagen signal from a defined tissue layer based on the birefringent nature of collagen structure.[21] Although the thick media layer contains a strong collagen signal, by using structured illumination microscopy, *en face* images of collagen in the thin intima layer alone can be acquired. Staining for vascular endothelial-cadherin (VE-cadherin) was used to identify the intima (Figure 4.5B). A color camera was used to capture the red, green and blue channel signals at the VE-cadherin z-plane, and intensity values were used to assess the intimal collagen content. Collagen content within the intima decreases following exercise and begins to increase following rest (Figure 4.5C). The standard deviation of intima collagen values within each image decreases following exercise, and returns to baseline after rest (Figure 4.5D). This represents that collagen micro-heterogeneities are impacted by exercise and rest.

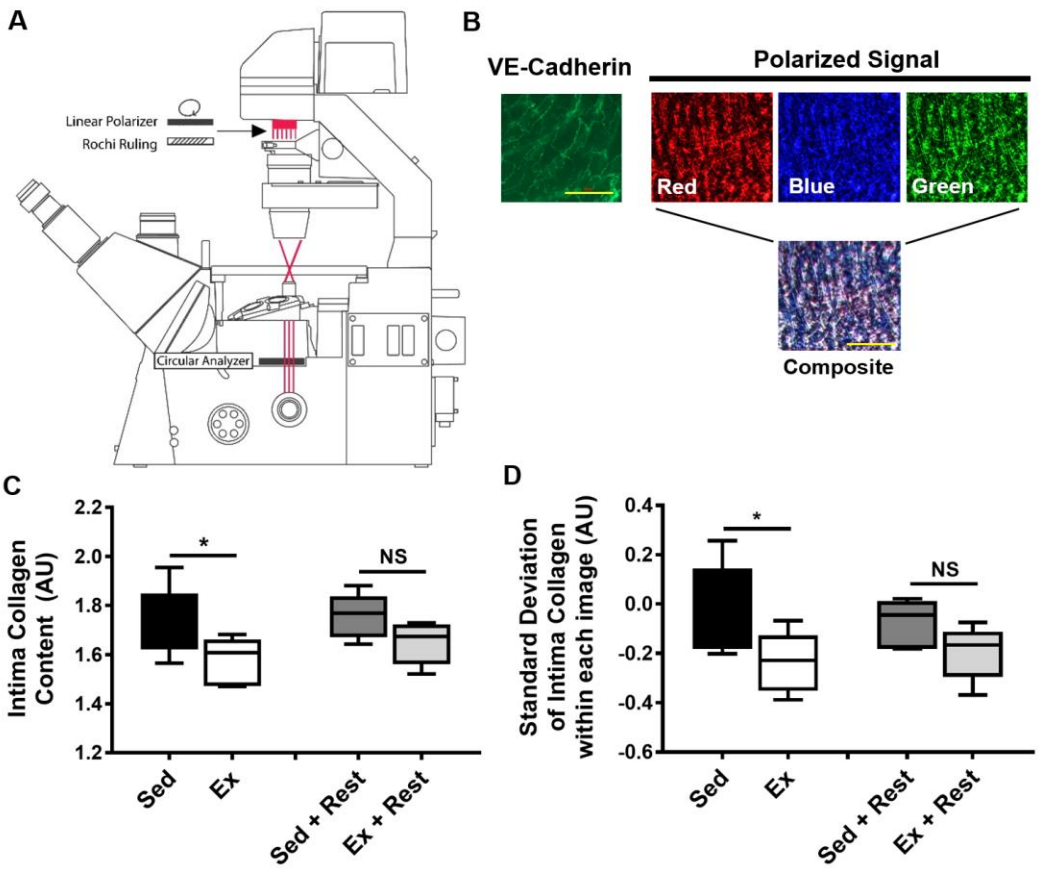

Figure 4.5: Collagen content in the intima and CML content in the aorta are affected by exercise and rest. (A) Schematic of the structured illumination microscope used to measure intimal collagen content. (B) The VE-cadherin layer was used to locate the intimal plane and the polarized signal from the intima was captured in three color channels for analysis; scale bar is 50 µm. (C) Intimal collagen content decreases with exercise and begins to increase following a rest period; n = 5 – 8 mice per group, error bars are minimum and maximum values. (D) Standard deviation of intima collagen content decreases with exercise and begins to increase following a rest period, * $p < 0.05$ (Student's t-test), n = 5 – 8 mice per group, error bars are SEM. NS = not statistically significant. The structured illumination microscope figure was created by Joseph Miller.

Aortic advanced glycation end product content follows the trends of vascular stiffness

AGEs are also associated with vascular stiffening[11] and can stimulate the crosslinking of collagen.[22] Here, we measured the aortic content of N(ε)-carboxymethyl-lysine (CML), which is a dominant protein modification found *in vivo*,[23] and increases with cardiovascular risk factors such as poor diet, sedentary lifestyle, and increased age.[10,24] CML is a Maillard reaction product that forms from glycolysis and oxidation reactions and accumulates with age.[23] CML is also a ligand for the receptor for advanced glycation end products, which triggers vascular inflammation cascades.[25] CML AGE content in the vessel decreases following exercise and returns to baseline after the rest period (Figure 4.6). These data demonstrate that not only is the ECM content of the intima altered following exercise cessation, but that AGEs (an ECM effector) are also affected.

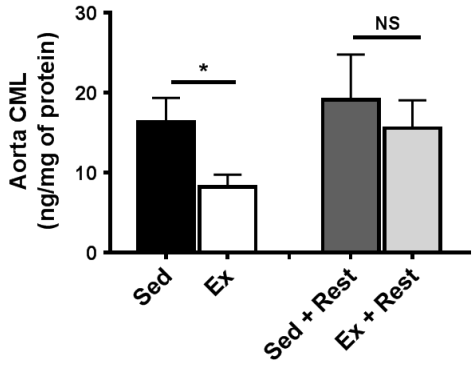

Figure 4.6: Aortic CML content decreases with exercise and increases following a rest period; * $p < 0.05$ (Student's t-test), n = 5 – 9 mice per group, error bars are SEM. NS = not statistically significant. The CML ELISA kit was run by Hannah Watkins.

4.5 Discussion

Prior studies have demonstrated that exercise modulates arterial compliance,[26,27] and arterial stiffness is decreased following exercise when compared to more sedentary age-matched peers.[26] Here, we examine changes in the beneficial effects of cardiac exercise following the cessation of an exercise regimen. Bulk and micro-scale stiffening deceased after exercise and increased back to baseline following a rest period. Importantly, PWV values returned to the level of those from sedentary peers after 4 weeks post-exercise, underscoring the importance of maintenance of a healthy and active lifestyle.

Our macro-scale data indicate that cardiac function, as assessed by LVEF, is inversely correlated with PWV. Other studies have also shown that higher LVEF is associated with lower rates of death due to cardiovascular disease,[28] and that bulk arterial stiffness is associated with systolic and diastolic dysfunction, independent of ejection fraction.[29] On the micro-scale, we demonstrate that LVEF is inversely correlated with micro-scale subendothelial matrix stiffness. Previously, LVEF has been correlated with endothelial function,[30] and interestingly, endothelial dysfunction plays a dominant role in heart failure patients with preserved LVEF.[31] Habitual aerobic exercise, through increased blood flow and shear stress, can reduce age-associated increases in bulk arterial stiffening, oxidative stress, inflammation and endothelial dysfunction.[32,33] These data together point to a relationship between macro-scale cardiac health, micro-scale arterial health, and the importance of habitual exercise.

While it is known that age-induced whole vessel[34] or diet-induced medial[35] collagen content is decreased following exercise, here we examined the role of collagen in the intimal layer. We imaged collagen in the intimal layer alone by examining *ex vivo* aorta sections *en face* under structured illumination microscopy. This new technique enabled measurement of the birefringence in the intima, which correlates with collagen content in the vessel. In the whole artery, aortic CML has been shown to increase with age and decrease with exercise.[10] Since CML and collagen levels follow similar trends to PWV and micro-scale subendothelial matrix stiffness measurements, and are both known factors in arterial stiffness modulation, we propose that CML and collagen content play a role in modulating arterial stiffness following exercise and exercise cessation on the macro- and micro-scales.

One possible cause for the relatively quick changes in intima collagen content may be due to increased collagen degradation with exercise, such as through matrix metalloproteinases (MMPs), which can degrade ECM proteins. Specifically, MMP-2 and MMP-9 are known to degrade basement membrane type IV collagen,[36] and MMP-1 can degrade type 1 collagen,[37] which are collagen types present in the intima ECM.[38] As MMP-1, -2, and -9 are also implicated in atherosclerosis initiation and plaque instability, and are effected by aerobic exercise training,[37] they may play a role in the transient collagen changes observed in our study. In fact, previous studies have found coincident changes in MMP-2 and MMP-9 with bulk vascular stiffening.[39,40] Future studies should examine the different factors that mediate intima collagen content with exercise treatment.

Our data also indicate that the elastic modulus of the subendothelial matrix in the mouse thoracic aorta is loading-rate dependent. It is well known that the artery is viscoelastic[41] as it is a composite material composed of 60% collagen and 30% elastin.[42,43] The intima layer itself is a complex tissue that contains type I collagen and type IV basement membrane collagen[38] and is bordered by the internal elastic lamina.[44] The complexity of the intimal components likely contributes to the viscous and elastic components of the material. The intima collagen also demonstrates complexity in its heterogeneity.

The subendothelial matrix is heterogeneous in elastic modulus, and recently we have shown that heterogeneity increases with age and is medicated with exercise.[5] Here, our data also demonstrate that intima collagen heterogeneity is influenced by age and exercise. We demonstrate that exercise reduces collagen standard deviation throughout intima images, and that this returns to baseline following rest. We propose that one possible cause for intima elastic modulus heterogeneities may be a change in collagen heterogeneity, and leave this as an avenue for future research.

4.6 Conclusions

Overall, our data indicate that exercise effectively decreases arterial stiffening on the macro- and micro-scale, but these effects do not persist. Arterial re-stiffening occurs within 8 weeks of rest following an exercise regimen of the same length. These findings underscore the importance of future studies to analyze the roles of ECM proteins and their effectors in the intima layer to further understand the mechanisms of intima stiffening. We also present intima collagen

heterogeneity as a possible avenue for future research in causes for micro-scale stiffness heterogeneities. Overall, our study demonstrates that continued exercise is important to maintaining cardiovascular health with respect to arterial stiffness, and the maintenance of a cardiovascular exercise regimen is critical.

4.7 References

1. Kohn, J. C. *et al.* Beneficial effects of exercise on arterial stiffness are short-lived. *In revision*.
2. Mitchell, G. F. *et al.* Arterial stiffness and cardiovascular events: the Framingham Heart Study. *Circulation* **121,** 505–511 (2010).
3. Fletcher, G. F. *et al.* Statement on exercise: benefits and recommendations for physical activity programs for all Americans. *Circulation* **94,** 857–862 (1996).
4. Grundy, S. M., Pasternak, R., Greenland, P., Smith, S. & Fuster, V. Assessment of cardiovascular risk by use of multiple-risk-factor assessment equations. *Circulation* **100,** 1481–1492 (1999).
5. Kohn, J. C. *et al.* Mechanical heterogeneities in the subendothelial matrix develop with age and decrease with exercise. *J. Biomech.* **49,** 1447–1453 (2016).
6. Gu, Q. *et al.* Chronic aerobic exercise training attenuates aortic stiffening and endothelial dysfunction through preserving aortic mitochondrial function in aged rats. *Exp. Gerontol.* **56,** 37–44 (2014).
7. Huynh, J. *et al.* Age-related intimal stiffening enhances endothelial permeability and leukocyte transmigration. *Sci. Transl. Med.* **3,** 112ra122 (2011).
8. Krishnan, R. *et al.* Substrate stiffening promotes endothelial monolayer disruption through

enhanced physical forces. *Am. J. Physiol. Cell Physiol.* **300,** C146–C154 (2011).

9. Fleenor, B. S. & Berrones, A. J. in *Arterial Stiffness: Implications and Interventions* 19–20 (Springer Internaional Publishing, 2015).
10. Gu, Q. *et al.* Contribution of receptor for advanced glycation end products to vasculature-protecting effects of exercise training in aged rats. *Eur. J. Pharmacol.* **741,** 186–194 (2014).
11. Fleenor, B. S. *et al.* Sodium nitrite de-stiffening of large elastic arteries with aging: Role of normalization of advanced glycation end-products. *Exp. Gerontol.* **47,** 588–594 (2012).
12. Berry, C. J. *et al.* Effects of deep sedation or general anesthesia on cardiac function in mice undergoing cardiovascular magnetic resonance. *J. Cardiovasc. Magn. Reson.* **11,** 16 (2009).
13. Peloquin, J., Huynh, J., Williams, R. M. & Reinhart-King, C. A. Indentation measurements of the subendothelial matrix in bovine carotid arteries. *J. Biomech.* **44,** 815–821 (2011).
14. Neil, M. A., Juskaitis, R. & Wilson, T. Method of obtaining optical sectioning by using structured light in a conventional microscope. *Opt. Lett.* **22,** 1905–1907 (1997).
15. Jalil, J. E. *et al.* Structural vs. contractile protein remodeling and myocardial stiffness in hypertrophied rat left ventricle. *J. Mol. Cell. Cardiol.* **20,** 1179–1187 (1988).
16. Rich, L. & Whittaker, P. Collagen and picrosirius red staining: a polarized light assessment of fibrillar hue and spatial distribution. *Brazilian J. Morphol. Sci.* **22,** 97–104 (2005).
17. Sacre, J. W., Jennings, G. L. R. & Kingwell, B. A. Exercise and dietary influences on arterial stiffness in cardiometabolic disease. *Hypertension* **63,** 888–893 (2014).
18. Conway, D. E. *et al.* Fluid shear stress on endothelial cells modulates mechanical tension across VE-cadherin and PECAM-1. *Curr. Biol.* **23,** 1024–1030 (2013).
19. Kohn, J. C., Lampi, M. C. & Reinhart-King, C. A. Age-related vascular stiffening: causes and

consequences. *Front. Genet.* **6,** 112 (2015).

20. Shadwick, R. E. Mechanical design in arteries. *J. Exp. Biol.* **202,** 3305–3313 (1999).
21. Wolman, M. & Kasten, F. H. Polarized light microscopy in the study of the molecular structure of collagen and reticulin. *Histochemistry* **85,** 41–49 (1986).
22. Sajithlal, G. B., Chithra, P. & Chandrakasan, G. Advanced glycation end products induce crosslinking of collagen in vitro. *Biochim. Biophys. Acta* **1407,** 215–224 (1998).
23. Dyer, D. G. *et al.* Accumulation of Maillard reaction products in skin collagen in diabetes and aging. *J. Clin. Invest.* **91,** 2463–2469 (1993).
24. Grossin, N. *et al.* Dietary CML-enriched protein induces functional arterial aging in a RAGE-dependent manner in mice. *Mol. Nutr. Food Res.* **59,** 927–938 (2015).
25. Kislinger, T. *et al.* N(episoln)-carboxymethyl lysine adducts of proteins are ligands for receptor for advanced glycation end products that activate cell signaling pathways and modulate gene expression. *J. Biol. Chem.* **274,** 31740–31749 (1999).
26. Santos-Parker, J. R., LaRocca, T. J. & Seals, D. R. Aerobic exercise and other healthy lifestyle factors that influence vascular aging. *Adv. Physiol. Educ.* **38,** 296–307 (2014).
27. Tanaka, H. *et al.* Aging, habitual exercise, and dynamic arterial compliance. *Circulation* **102,** 1270–1275 (2000).
28. Regnault, V. *et al.* Opposite predictive value of pulse pressure and aortic pulse wave velocity on heart failure with reduced left ventricular ejection fraction. *Hypertension* **63,** 105–111 (2014).
29. Weber, T. *et al.* Arterial stiffness and arterial wave reflections are associated with systolic and diastolic function in patients with normal ejection fraction. *Am. J. Hypertens.* **21,** 1194–1202

(2008).

30. Bae, J. *et al.* Impact of left ventricular ejection fraction on endothelial function in patients with coronary artery disease. *Clin. Cardiol.* **27,** 333–337 (2004).
31. Giamouzis, G., Schelbert, E. B. & Butler, J. Growing evidence linking microvascular dysfunction with heart failure with preserved ejection fraction. *J. Am. Heart Assoc.* **5,** e003259 (2016).
32. Seals, D. R., Desouza, C. A., Donato, A. J. & Tanaka, H. Habitual exercise and arterial aging. *J. Appl. Physiol.* **105,** 1323–1332 (2008).
33. Seals, D. R. Edward F. Adolph Distinguished Lecture: The remarkable anti-aging effects of aerobic exercise on systemic arteries. *J. Appl. Physiol.* **117,** 425–439 (2014).
34. Fleenor, B. S., Marshall, K. D., Durrant, J. R., Lesniewski, L. A. & Seals, D. R. Arterial stiffening with ageing is associated with transforming growth factor-β1-related changes in adventitial collagen: reversal by aerobic exercise. *J. Physiol.* **588,** 3971–3982 (2010).
35. Padilla, J. *et al.* Regular exercise reduces endothelial cortical stiffness in Western diet – fed female mice. *Hypertension* **68,** 1236–1244 (2016).
36. Mook, O. R. F., Frederiks, W. M. & Noorden, C. J. F. Van. The role of gelatinases in colorectal cancer progression and metastasis. *Biochim. Biophys. Acta* **1705,** 69–89 (2004).
37. Jaoude, J. & Koh, Y. Matrix metalloproteinases in exercise and obesity. *Vasc. Health Risk Manag.* **12,** 287–295 (2016).
38. Murata, K., Motayama, T. & Kotake, C. Collagen types in various layers of the human aorta and their changes with the atherosclerotic process. *Atherosclerosis* **60,** 251–262 (1986).
39. Anea, C. B. *et al.* Matrix metalloproteinase 2 and 9 dysfunction underlie vascular stiffness in circadian clock mutant mice. *Arterioscler. Thromb. Vasc. Biol.* **30,** 2535–2543 (2010).

40. Yasmin *et al.* Matrix metalloproteinase-9 (MMP-9), MMP-2, and serum elastase activity are associated with systolic hypertension and arterial stiffness. *Arterioscler. Thromb. Vasc. Biol.* **25,** 372–378 (2005).

41. Learoyd, B. M. & Taylor, M. G. Alterations with age in the viscoelastic properties of human arterial walls. *Circ. Res.* **18,** 278–292 (1966).

42. Powell, J., Vine, N. & Crossman, M. On the accumulation of D-aspartate in elastin and other proteins of the ageing aorta. *Atherosclerosis* **97,** 201–208 (1992).

43. Rizzo, R. *et al.* Collagen types and matrix protein content in human abdominal aortic aneurysms. *J. Vasc. Surg.* **10,** 365–373 (1989).

44. Gerrity, R. G. & Cliff, W. J. The aortic tunica intima in young and aging rats. *Exp. Mol. Pathol.* **16,** 382–402 (1972).

CHAPTER 5

WESTERN DIET-INDUCED SUBENDOTHELIAL MATRIX STIFFENING IS MITIGATED BY EXERCISE

This chapter includes sections from a manuscript currently in preparation. Mouse body weight was recorded by Julian Azar. The structured illumination microscope was setup by François Bordeleau. The CML ELISA kit was run by Hannah Watkins.

5.1 Abstract

Consumption of a Western (high-fat, high-sugar) diet and sedentary lifestyle are correlated with bulk arterial stiffening. While measurements of bulk arterial stiffening are used as the gold standard to assess cardiovascular health clinically, they cannot account for changes on the cellular scale. The compliance of the subendothelial matrix in the intima mediates vascular permeability, an initiating step in atherosclerosis. Western diet consumption and a sedentary lifestyle both cause micro-scale subendothelial matrix stiffening, but the impact of these factors in concert remains unknown. In this study, mice on a Western diet were treated with exercise or a change to a normal diet. Western diet-induced micro-scale stiffening can be mitigated by exercise, and while diet reversal decreases macro- and micro-scale stiffness, exercise only significantly decreases micro-scale stiffness. These data underscore the need for both healthy diet and exercise to maintain vascular health but also indicate that exercise may serve as a key

lifestyle modification to reverse the deleterious impacts of Western diet consumption, even while macro-scale stiffness indicators do not change.

5.2 Introduction

Cardiovascular disease (CVD) is a leading cause of death worldwide, and atherosclerosis, the development of lipid-rich plaques in the major arteries, is a primary contributor to CVD.[1] Arterial stiffening is an independent predictor of CVD onset, and is often measured clinically by pulse wave velocity (PWV), a measurement of a pressure wave as it travels down the atrial tree.[2] CVD risk factors, such as consumption of a Western diet, advanced age, and lack of exercise, promote bulk arterial stiffening.[3–5] Specifically, mice that consume a Western (high-fat, high-sugar or HFHS) diet exhibit an increase in macro-scale arterial stiffness[3,6–8] and reversal to a normal diet can return the vessel to its original compliance.[8] After consumption of a Western diet, implementation of an exercise regimen has been shown to decrease[7] or to cause no effect[9] on bulk arterial stiffness, however less is known about the specific mechanics of the arterial intima.[5]

Endothelial cells respond to the micro-scale extracellular mechanical cues of the subendothelial matrix. Subendothelial matrix stiffening due to aging causes a loss of endothelial cell-cell junctional integrity, increased vascular permeability, and leukocyte transmigration;[10–12] subsequent cholesterol accumulation in the arterial wall is an initiating step in atherosclerotic plaque progression.[13] Given the rise of CVD and obesity in recent decades,[14] there is a need to understand the impact of lifestyle factors such as diet and exercise on arterial health. Here, we

investigate the combined effects of the Western diet and an exercise regimen on bulk arterial and subendothelial matrix stiffness.

5.3 Materials and Methods

Animal model: All animal work was conducted under an approved Cornell University IACUC protocol and with the least harm to the animals possible. C57Bl/6 male mice (Jackson Labs, #00664) were obtained at 8 weeks old and given ear punches to differentiate each animal. Mice were allowed to eat *ad labium* and maintained in a 12-hour light/dark cycle while in their cages. In the diet-period (first two months), mice were given a HFHS ('Western' diet) with 35.5% fat and 18.2% sucrose, or a ND with 4.5% fat and 0% sucrose (D09071702 and D09071703 from Research Diets, respectively). In the exercise-period, mice maintained their initial diet, changed diets, or underwent an exercise regimen. Exercise and sedentary mice were house together and different diet group mice were housed in separate cages. Animals were weighed approximately three times each week and their weights were normalized to their pre-diet weight.

Swimming exercise regimen: An exercise regimen was employed as previously described.[15] Briefly, mice swam in groups of 2 to 5 over an 8-week period. Mice were first acclimated to the environment with three 3-minute swim sessions. Sedentary control mice were kept in their cages while their exercised cage-mates were swimming in the same room. The swimming regimen employed swimming 5 days a week for 10 minutes a day in week 1, 30 minutes a day in weeks 2 – 3, and 45 minutes a day in weeks 4 – 8. After swimming the mice were dried off with a paper

towel before placing them in the cage and were monitored. Mice did not swim on days where blood collection or anesthetization took place.

Blood pressure: A non-invasive blood pressure tail cuff (Kent Scientific) was used to measure blood pressure on non-sedated mice based on their user guidelines. Mice were acclimated to the constraint tubes in days prior to the blood pressure measurements. During the procedure, constraint tubes held the mice, the tail cuff was placed on, and 10 cycles were captured with a 20 second cuff deflation time for each animal. The software was used to determine accepted versus rejected cycles based on a minimum of 10 µL of blood tail volume.

Pulse wave velocity (PWV): A Vevo 2100 ultrasound was used to measure bulk stiffness in the abdominal aorta as previously described.[8] Briefly, mice were anaesthetized using 0.5 – 2% isoflurane, laid supine on a heating platform, and hair was removed with cream (Nair). The renal vein was used as a location reference, and stretches of the abdominal aorta from 5 to 9 mm long were imaged using a MS550D ultrasound transducer at approximately 4 – 6 mm beneath the skin surface, collecting at least 5 heart beat cycles. Vevo software was used to measure the distance along the artery, and the arrival time at each location was measured from the peak of the R wave to the velocity upstroke. PWV was calculated as the distance divided by the difference of the two arrival times (transit time).

Subendothelial matrix mechanics: The subendothelial matrix elastic modulus was measured using atomic force microscopy (AFM) (Asylum MFP-3D) on the fresh thoracic aorta intima layer as

previously published.[15] Briefly, after the animal was anaesthetized and sacrificed through a heart perfusion of ice-cold phosphate buffered saline (PBS), the thoracic aorta was removed and the was fat cleaned off of the tissue. The tissue was cut longitudinally, glued onto a petri dish (Loctite Super Glue), and covered in room temperature PBS. The endothelial cells were scraped off as previously described[16] to expose the underlying subendothelial matrix. A cantilever (Novascan) was used with a spring constant of 0.12 N/m as calibrated by the manufacturer and calibrated before the experiment at 0.11 ± 0.05 N/m, with a 10 μm diameter polystyrene bead. Indentations of the tissue were made using a velocity of approximately 1 μm/sec and a loading rate of approximately 40 nN/sec, providing an indentation depth of approximately 75 nm. The data was fit to the Hertz Model as previously shown[10,15,16] assuming a Poisson's ratio of 0.5 by using the provided Asylum software to determine the elastic modulus.

N(ε)-carboxymethyl lysine (CML) ELISA: Following mouse sacrifice, sections of the thoracic aortas were flash frozen with liquid nitrogen and stored at -80°C. The aortas were crushed using a cold mortar and pestle and 300 μL of RIPA buffer with 1:1000 protease inhibitor was used to solubilize the pieces. The competitive CML ELISA kit (Cell Biolabs STA-816) was run according to manufacturer's specifications and total protein concentration was measured using a bicinchoninic acid (BCA) assay (Pierce, Thermo Scientific), as in our previous study.[17] A weight fraction was determined by dividing the CML concentration by the total protein concentration (ng CML per mg protein). For group comparisons, data were normalized based on mouse body weight.

Intima collagen content: At the time of mouse sacrifice, thoracic aorta sections were removed and fixed in 3.7% formaldehyde for 15 minutes and then soaked in phosphate buffered saline. Initma collagen content was measured as previously described using structured illumination.[17] Briefly, picrosirius red (Polysciences, Inc 24901) was used to stain the samples and a structured illumination microscope (SIM), was used to detect sample birefringence. The intima layer was identified by VE-Cadherin staining, using a primary antibody (1:100, Cell Signaling) and secondary (1:200 Alexaflour-488) overnight. Images of birefringence were analyzed for intensity using ImageJ software, corrected with grayscale factors, and total intensity were compared between groups.

Statistical Analysis: Data were analyzed on Prism software and tested for normality using a Shapiro-Wilk test. For two groups being compared, a Student's t-test was used and for group comparisons, one-way analysis of variance (ANOVA) with Dunnett's multiple comparisons test comparing to the ND group were used, with p-values of less than 0.05 as significant. Linear correlations were found to be significant with a Pearson Correlation p-value of less than 0.05 for all data groups combined in the figure. Error bars are presented as standard error of the mean (SEM).

5.4 Results

Mouse body weight and blood pressure increase on a Western diet

Mice were fed a normal diet (ND) or a HFHS diet during a two-month period, followed by either 8 weeks of exercise or sedentation while either on a ND or HFHS diet (Figure 5.1A). Mouse body

weight increased on the HFHS diet and returned to baseline within two weeks of switching to the ND and remaining sedentary (Figure 5.1B). The body weight of mice that remained on a HFHS diet remained elevated, even following the exercise regimen. Since PWV increases during exercise with high stress levels,[18] and previous studies emphasize the importance of monitoring blood pressure when measuring bulk stiffness,[19–21] we recorded blood pressure to provide a more complete understanding of bulk destiffening. Systolic and diastolic blood pressure, as well as mean arterial pressure (MAP) were higher in mice that remained on the HFHS diet for the duration of the study, regardless of whether or not they exercised (Figure 5.1C). While change to a ND was effective at reducing blood pressure and body weight, the exercise regimen did not affect these metrics.

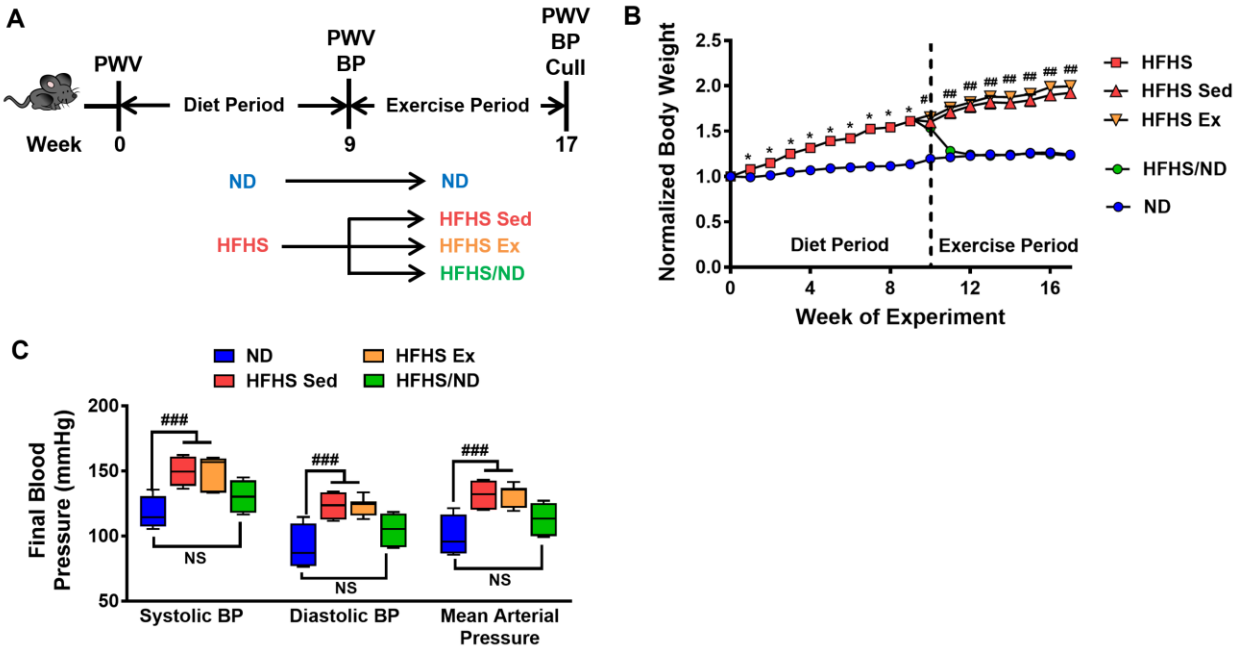

Figure 5.1: Mouse body weight and blood pressure increase after high-fat, high-sugar (HFHS) diet consumption. (A) During the diet period, mice consumed a normal diet (ND) or HFHS diet for two

months. During the exercise period, the mice maintained their initial diet and remained sedentary (ND and HFHS Sed), underwent an 8-week exercise regimen (HFHS Ex) or switched diets while remaining sedentary (HFHS/ND). (B) Normalized mouse body weight was significantly increased with HFHS diet and decreased after return to ND, * $p < 0.05$ (Student's t-test); # $p < 0.05$ (ANOVA, all groups are significantly different from ND); ## $p < 0.05$ (ANOVA, HFHS Sed and HFHS Ex groups are significantly different from ND). (C) Systolic and diastolic blood pressure, as well as mean arterial pressure, increased in the HFHS Sed and HFHS Ex groups by the conclusion of the study, ### $p < 0.005$ (ANOVA, HFHS Sed and HFHS Ex groups are significantly different from ND); NS = not significantly different, during the diet period n = 8 mice for ND and 27 mice for HFHS group, during the exercise period n = 4 to 7 mice per diet/exercise group. Body weights were recorded by Julian Azar.

PWV increases after 2 months on HFHS diet, irrespective of blood pressure

Blood pressure values were recorded throughout the experiment to provide a more thorough understanding of cardiovascular health. Diastolic blood pressure and mean arterial pressure increased following the first two months on the HFHS diet, although there was no detectable change in systolic blood pressure (Figure 5.2A). To assess if the diet treatment increased bulk stiffness and not simply blood pressure, PWV data were graphed versus MAP values for the same animal as previously shown.[20-21] At this time point, mice at a given MAP generally experienced higher PWV after HFHS diet consumption compared to those on the ND (Figure 5.2B). This figure panel demonstrates an upward shift in the stiffness versus blood pressure linear trends, indicating higher PWV values for the HFHS diet group at the same MAP value.

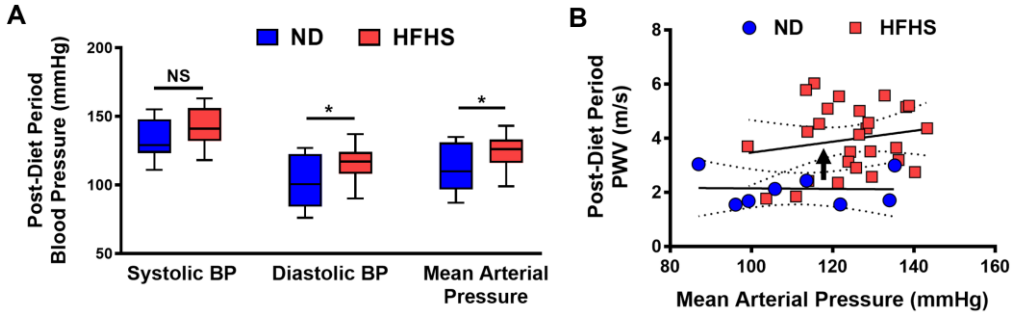

Figure 5.2: Post diet-period pulse wave velocity (PWV) and blood pressure increase in response to a high-fat, high-sugar (HFHS) diet. (A) Diastolic blood pressure (BP) and mean arterial pressure (MAP) increased after two months on a HFHS diet compared to a ND, but systolic BP did not significantly increase; box and whisker plots with min/max error bars; * $p < 0.05$ (Student's t-test); NS = not significantly different. (B) PWV versus MAP plot indicates an upward shift in PWV for HFHS diet mice at a given MAP value; each data point is one mouse, linear regressions displayed with 95% confidence interval bands. Arrow indicates upward shift in PWV for a given MAP value from the ND to HFHS diet group; n = 8 mice for ND and 27 mice for HFHS group.

Western diet-induced bulk arterial stiffening is mitigated by diet reversal, but not by exercise

To track the progression of macro-scale vascular health throughout the study, non-invasive PWV and blood pressure measurements were collected after the diet period and at the end of the study. In the first two months, PWV increased in mice on a HFHS diet compared to their counterparts on a ND (Figure 5.3A). At the end of the time course, PWV returned to baseline in HFHS diet mice that changed to the ND. However, PWV in the HFHS diet mice after the exercise regimen remained elevated by 60% compared to the ND cohort (Figure 5.3B).

Western diet-induced subendothelial matrix stiffening is mitigated by diet reversal and exercise

Using atomic force microscopy, the subendothelial matrix stiffness was measured at the end of the time course to determine the effects of diet and exercise on micro-scale arterial health. HFHS diet-induced subendothelial matrix stiffening was mitigated by diet reversal or, to a similar extent, by the exercise regimen (Figures 5.3C and 5.3D). While macro-scale stiffness significantly returned to baseline only after diet reversal, the subendothelial matrix stiffness returned to baseline after diet reversal or the exercise regimen. These data indicate that exercise while on a HFHS diet has a significant effect on subendothelial matrix de-stiffening, but does not affect bulk arterial de-stiffening.

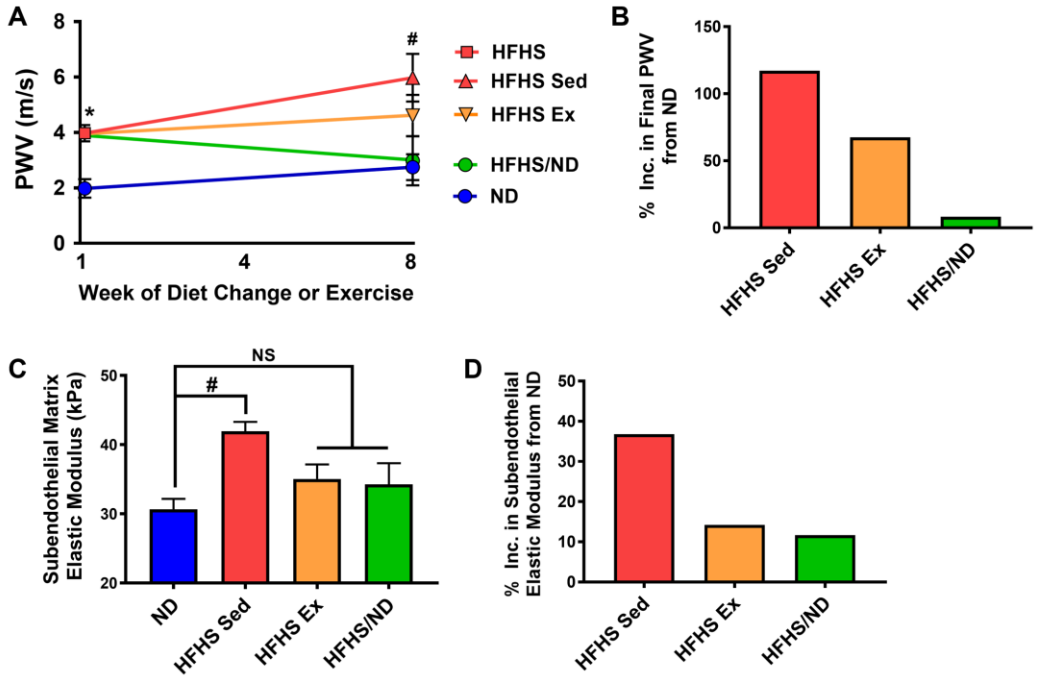

Figure 5.3: Arterial stiffness is affected by diet consumption and exercise. (A) At the start of the exercise period, macro-scale pulse wave velocity (PWV) increased in mice on a high-fat, high-sugar (HFHS) diet compared to those on a normal diet (ND). After 8 weeks, PWV decreased in

mice that switched to a ND, while PWV remained elevated for HFHS exercise mice; * $p < 0.05$ (Student's t-test); # $p < 0.05$ (ANOVA, HFHS Sed and HFHS Ex groups are significantly different from ND). (B) The HFHS Sed and HFHS Ex groups maintain a high percent increase in PWV compared to ND, while the HFHS/ND group returns almost to baseline. (C) Micro-scale subendothelial matrix elastic modulus measured with AFM increased after a HFHS diet, and was recovered with diet reversal or an exercise regimen; # $p < 0.05$ (ANOVA, HFHS Sed group is significantly different from ND); NS = not significantly different. (D) The HFHS Sed group has the largest percent increase in subendothelial matrix elastic modulus compared to ND; during the diet period n = 8 mice for ND and 27 mice for HFHS group, during the exercise period n = 4 to 7 mice per diet/exercise group.

Arterial stiffness, body weight, and blood pressure are correlated

Data sets were collected from all treatment groups and analyzed for significant correlations between arterial stiffness, body weight and blood pressure. At the end of the study, PWV was linearly correlated with normalized mouse body weight (Figure 5.4A). However, subendothelial matrix elastic modulus did not demonstrate a significant linear Pearson Correlation to normalized body weight (Figure 5.4B). Next, we examined correlations between macro- and micro-scale stiffness and final MAP. Both PWV and subendothelial matrix elastic modulus are linearly correlated with MAP (Figures 5.4C and 5.4D).

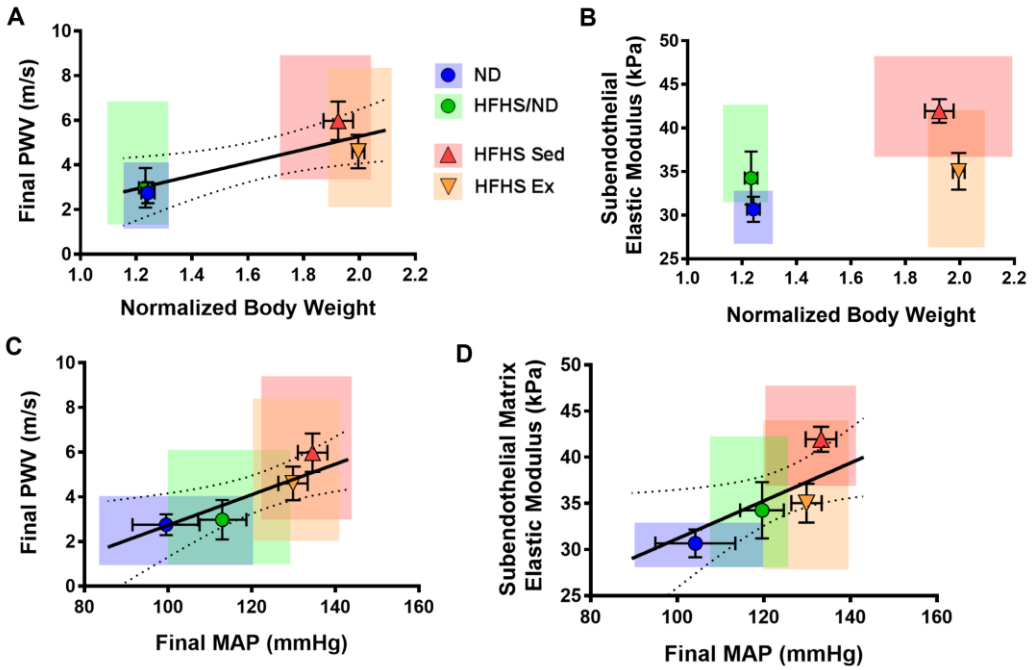

Figure 5.4: Positive linear correlations are measured between pulse wave velocity (PWV), subendothelial matrix stiffness, mouse body weight and mean arterial pressure (MAP). There is a significant positive correlation between (A) mouse body weight and PWV, but not between (B) mouse body weight and subendothelial elastic modulus. MAP is linearly correlated with (C) PWV and (D) subendothelial matrix elastic modulus. For all graphs, the error bars are SEM and colored boxes represent the full range of values, statistically significant correlations were determined by Pearson Correlation, $p < 0.05$, linear regressions displayed with 95% confidence interval bands; n = 4 to 7 mice per diet/exercise group.

No significant change was detected in arterial advanced glycation end product content after HFHS diet consumption or interventional treatments

To examine possible causes for increased bulk arterial stiffness, we measured aortic advanced glycation end product content at the conclusion of the time course. N(ε)-carboxymethyl lysine

(CML) is a common *in vivo* advanced glycation end product[22] known to contribute to arterial stiffening.[23] We used a CML ELISA to assess whole vessel CML content, as CML can cause endothelial cell dysfunction and vessel stiffening through diet.[23] While we observed a downward trend in aortic CML content in exercised mice on a HFHS diet compared to the ND cohort, no significant decrease was measured (Figure 5.5A).

No significant change was detected in intima collagen content after HFHS diet consumption or interventional treatments

Intimal collagen content was measured at the end of the study as a possible cause of micro-scale arterial stiffening. Collagen is a common extracellular matrix protein involved in arterial stiffness[5,9,24] and intima collagen levels decrease following exercise in aged mice.[17] At the end of the study, thoracic aorta sections were stained and imaged to detect collagen content in the intima layer alone. However, our data indicate that there are no significant changes in intimal collagen content due to HFHS diet or exercise (Figure 5.5B).

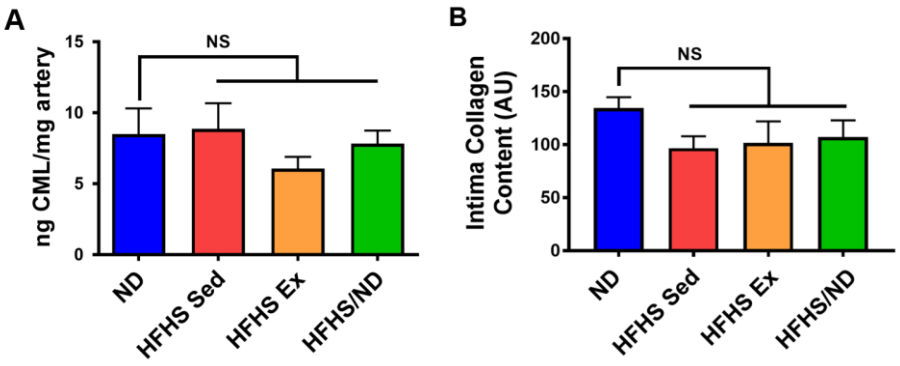

Figure 5.5: Diet and exercise did not have a significant effect on arterial advanced glycation end product or intima collagen content. (A) Aortic advanced glycation end product N(ε)-

carboxymethyl lysine (CML) content was not significantly altered by the experimental treatments (ANOVA, compared to ND). (B) No significant difference in intimal collagen content was found compared to the ND cohort (ANOVA, compared to ND), NS = not significantly different; n = 4 to 7 mice per diet/exercise group.

5.5 Discussion

Together, our data indicate that exercise can mitigate Western diet-induced subendothelial matrix stiffening, but it does not affect macro-scale stiffness. These data suggest that mechanical changes in the intima layer are not occurring to the same extent in the larger vessel. Previously, we found that macro-scale stiffness, measured through PWV, mirrored the same trends as micro-scale stiffening. Following consumption of a Western diet, PWV and subendothelial matrix stiffness increased, and both were reversed after return to a normal diet.[8] This same trend exists in aged mice that have exercised, where exercise-mediated destiffening occurs in aged mice on both the macro- and micro-scale and PWV and subendothelial matrix stiffness are linearly correlated.[15] While indicators of bulk stiffness, such as PWV, remain the main clinical assessment of arterial health,[2] our study here indicates that changes may occur on the micro-scale which are not detectable by only measuring bulk arterial stiffness.

Interestingly, changes in endothelial cell phenotype have also been observed in the absence of significant changes to macro-scale arterial stiffness.[7,9] After exercise, Western diet-fed young mice show improvement in cellular stiffness and contractility,[9] and improvement in endothelium-dependent dilation.[7] As previous work demonstrates that micro-scale stiffness also affects

endothelial cell function,[10,11] these data suggest that exercise, even in the absence of changes in macro-scale stiffness, may improve vascular cell health. As such, one possible explanation for the changes to endothelial cell phenotype indicated by these other groups[7,9] is through altered subendothelial matrix stiffness. Together with previous studies, our data further emphasize the necessity of understanding the different roles of subendothelial matrix mechanics and whole vessel stiffening in cardiovascular health.

Based on our data, Western diet-induced stiffening is best mitigated through diet reversal, as this has the largest effect on both micro- and macro-scale stiffness. We previously demonstrated that changing diet from a Western diet to a ND can mitigate elevated PWV and subendothelial matrix stiffening.[8] On the other hand, exercise after poor diet consumption has a complex relationship with arterial stiffness. Patient studies show that PWV decreases following a hypocaloric diet, but does not change after low-intensity resistance exercise training alone,[25] and that PWV may not show a significant change after exercise and diet lifestyle modifications.[26] These studies, along with our data here, suggest that change in diet is more effective for decreasing PWV than exercise and has the added impact of reducing subendothelial matrix stiffening.

To determine the cause of macro-scale stiffening, we assessed arterial wall advanced glycation end product content. Specifically, we measured aortic content of CML, a dominant advanced glycation end product found *in vivo*.[22] Previously, exercise in aged[27] or obese and diabetic[28] rats decreased advanced glycation end product levels. In our study, we did not find any significant change in CML content in arteries of exercised mice on a HFHS diet, although we note a decreased

trend in this group. Other factors, such as blood insulin levels and structural protein content, may have also played a role in the consistent elevated PWV displayed by the HFHS diet exercised mice.

Artery wall structural components, such as collagen and elastin, are associated with arterial stiffening.[9,29] To further investigate the possible causes of subendothelial matrix stiffening with HFHS diet, we examined intimal collagen content but found no change after HFHS diet or exercise. This confirms previous work demonstrating no change in total arterial collagen following a high-fat[30] or HFHS diet.[8] It is possible that elastin, rather than collagen, may play a role in inducing mechanical changes in the murine subendothelial matrix, as elastin content decreases as a result of high-fat diet[30] and increases in response to exercise in Western diet-fed mice.[9] While many studies examine the causes of arterial stiffening, the stiffening mechanisms of the subendothelial matrix layer alone are yet to be determined.

The exercise period used in this study was successful at micro-scale arterial destiffening, but did not cause bulk arterial destiffening following Western diet consumption. PWV may further decrease if given a longer swim period, or a different type of exercise, although the literature demonstrates different outcomes from exercise regimens.[7,9] In apolipoprotein-E deficient mice on a high-fat diet, swimming for 8 or 16 weeks has proven to be effective in reducing fatty streaks or fibrofatty plaques, respectively.[31] However, in our study, swimming for 8 weeks was sufficient to reduce subendothelial matrix stiffness, but not reduce PWV statistically for mice remaining on a HFHS diet. Together, these data suggest that even in the absence of changes to the macro-

scale stiffness of the vessel, exercise may help reduce atherosclerosis through changes to the intimal stiffness.

5.6 Conclusions

We demonstrate that both exercise and return to a healthy diet affect subendothelial matrix stiffness, while only diet reversal decreases bulk stiffening. The mechanical properties of the intima are influenced by factors that may not be detected by bulk arterial stiffness measurements; continued research with focus on the intima is needed in addition to bulk artery measurements since intimal mechanics directly influences endothelial cell function and atherogenesis.

5.7 References

1. Frostegård, J. Immunity, atherosclerosis and cardiovascular disease. *BMC Med.* **11,** 117 (2013).
2. Mitchell, G. F. *et al.* Arterial stiffness and cardiovascular events: the Framingham Heart Study. *Circulation* **121,** 505–511 (2010).
3. Bender, S. B. B. *et al.* Regional variation in arterial stiffening and dysfunction in Western diet-induced obesity. *Am. J. Physiol. Hear. Circ. Physiol.* **309,** H574-582 (2015).
4. Grundy, S. M., Pasternak, R., Greenland, P., Smith, S. & Fuster, V. Assessment of cardiovascular risk by use of multiple-risk-factor assessment equations. *Circulation* **100,** 1481–1492 (1999).
5. Kohn, J. C., Lampi, M. C. & Reinhart-King, C. A. Age-related vascular stiffening: causes and

consequences. *Front. Genet.* **6,** 112 (2015).

6. Foote, C. A. *et al.* Arterial stiffening in Western diet-fed mice is associated with increased vascular elastin, transforming growth factor-β, and plasma neuraminidase. *Front. Physiol.* **7,** 285 (2016).
7. Lesniewski, L. A. *et al.* Aging compounds western diet-associated large artery endothelial dysfunction in mice: prevention by voluntary aerobic exercise. *Exp. Gerontol.* **48,** 1218–1225 (2013).
8. Weisbrod, R. M. *et al.* Arterial stiffening precedes systolic hypertension in diet-induced obesity. *Hypertension* **62,** 1105–1110 (2013).
9. Padilla, J. *et al.* Regular exercise reduces endothelial cortical stiffness in Western diet – fed female mice. *Hypertension* **68,** 1236–1244 (2016).
10. Huynh, J. *et al.* Age-related intimal stiffening enhances endothelial permeability and leukocyte transmigration. *Sci. Transl. Med.* **3,** 112ra122 (2011).
11. Krishnan, R. *et al.* Substrate stiffening promotes endothelial monolayer disruption through enhanced physical forces. *Am. J. Physiol. Cell Physiol.* **300,** C146–C154 (2011).
12. Stroka, K. M. & Aranda-Espinoza, H. Endothelial cell substrate stiffness influences neutrophil transmigration via myosin light chain kinase-dependent cell contraction. *Blood* **118,** 1632–1640 (2011).
13. Lusis, A. Atherosclerosis. *Nature* **407,** 233–241 (2000).
14. Mozaffarian, D. *et al.* Heart disease and stroke statistics—2016 Update. *Circulation* **133,** e38–e360 (2016).
15. Kohn, J. C. *et al.* Mechanical heterogeneities in the subendothelial matrix develop with age

and decrease with exercise. *J. Biomech.* **49,** 1447–1453 (2016).

16. Peloquin, J., Huynh, J., Williams, R. M. & Reinhart-King, C. A. Indentation measurements of the subendothelial matrix in bovine carotid arteries. *J. Biomech.* **44,** 815–821 (2011).
17. Kohn, J. C. *et al.* Beneficial effects of exercise on arterial stiffness are short-lived. Submitted.
18. Roberts, P. A. *et al.* Real-time aortic pulse wave velocity measurement during exercise stress testing. *J. Cardiovasc. Magn. Reson.* **17,** 86 (2015).
19. Niederhoffer, N. *et al.* Physical exercise, aortic blood pressure, and aortic wall elasticity and composition in rats. *Hypertension* **35,** 919–924 (2000).
20. Steppan, J. *et al.* Exercise, vascular stiffness, and tissue transglutaminase. *J. Am. Heart Assoc.* **3,** e000599 (2014).
21. Sacre, J. W., Jennings, G. L. R. & Kingwell, B. A. Exercise and dietary influences on arterial stiffness in cardiometabolic disease. *Hypertension* **63,** 888–893 (2014).
22. Dyer, D. G. *et al.* Accumulation of Maillard reaction products in skin collagen in diabetes and aging. *J. Clin. Invest.* **91,** 2463–2469 (1993).
23. Grossin, N. *et al.* Dietary CML-enriched protein induces functional arterial aging in a RAGE-dependent manner in mice. *Mol. Nutr. Food Res.* **59,** 927–938 (2015).
24. Fleenor, B. S., Marshall, K. D., Durrant, J. R., Lesniewski, L. A. & Seals, D. R. Arterial stiffening with ageing is associated with transforming growth factor-β1-related changes in adventitial collagen: reversal by aerobic exercise. *J. Physiol.* **588,** 3971–3982 (2010).
25. Figueroa, A. *et al.* Effects of diet and/or low-intensity resistance exercise training on arterial stiffness, adiposity, and lean mass in obese postmenopausal women. *Am. J. Hypertens.* **26,** 416–423 (2013).

26. Miyatake, N., Sakano, N., Saito, T. & Numata, T. Changes in exercise habits and pulse wave velocity with lifestyle modification in Japanese. *Open J. Epidemiol.* **2,** 50–54 (2012).
27. Gu, Q. *et al.* Contribution of receptor for advanced glycation end products to vasculature-protecting effects of exercise training in aged rats. *Eur. J. Pharmacol.* **741,** 186–194 (2014).
28. Boor, P. *et al.* Regular moderate exercise reduces advanced glycation and ameliorates early diabetic nephropathy in obese Zucker rats. *Metabolism* **58,** 1669–1677 (2009).
29. Fleenor, B. S. *et al.* Sodium nitrite de-stiffening of large elastic arteries with aging: role of normalization of advanced glycation end-products. *Exp. Gerontol.* **47,** 588–594 (2012).
30. Henson, G. D., Walker, A. E., Reihl, K. D., Donato, A. J. & Lesniewski, L. A. Dichotomous mechanisms of aortic stiffening in high-fat diet fed young and old B6D2F1 mice. *Physiol. Rep.* **2,** e00268 (2014).
31. Okabe, T. *et al.* Swimming reduces the severity of atherosclerosis in apolipoprotein E deficient mice by antioxidant effects. *Cardiovasc. Res.* **74,** 537–545 (2007).

CHAPTER 6

SUBENDOTHELIAL MATRIX HETEROGENEITIES INDUCE HETEROGENEOUS BASAL CELL STRAIN

This chapter includes sections from a manuscript currently in preparation.

6.1 Abstract

Within the artery intima, endothelial cells respond to mechanical cues and changes in subendothelial matrix stiffening. Recently, we found that the aging subendothelial matrix stiffens heterogeneously on the micro-scale. However, the impacts of these complex mechanical micro-heterogeneities on endothelial cells has not been fully understood. Here, we simulate the effects of homogeneous and heterogenous substrates, as well matrices that mimic young and aged vessels, on single and multi-cell endothelial cell models. More heterogeneous basal strain distributions are present in the single and multi-cell models on the substrate mimicking an aged artery over those exhibited on the young artery. Overall, our data indicate that micro-scale arterial mechanics present in the subendothelial matrix, as are found *in vivo*, can induce heterogeneous strain profiles in endothelial cells.

6.2 Introduction

Arterial stiffening occurs with advanced age in the artery intima,[1,2] the innermost layer composed of the endothelial cell (EC) monolayer and subendothelial matrix. On stiffer substrates, ECs

experience decreased cell-cell junction stability, monolayer disruption, and increased permeability.[2,3] Cholesterol permeabilization into the artery wall is an initiating step in atherosclerosis,[4] and the response of ECs to physiological mechanical cues can be disease-promoting. The forces exhibited in the basal layer of cells play a vital role in cellular function; traction forces, arising from actomyosin interactions, are altered by substrate stiffness,[5] and instability in traction forces is a predictor for endothelial cell-cell junctional gaps.[6] EC monolayers exhibit more complex mechanics, as cells can detect traction stresses exerted by neighboring cells,[7] and forces exerted in one area of an EC monolayer can be transduced across vascular endothelial (VE)-cadherin, a cell-cell junctional protein.[8] In fact, mechanotransduction mediated through VE-cadherin can trigger signals for focal adhesion and cell-cell junctional disruption.[8]

Many mechanical forces are at play in arteries, including intraluminal pressure, which causes circumferential artery stretch, and axial fluid shear stress due to blood flow.[9–11] Cyclic stretch of the artery also plays a role in vascular health, such as through the mediation of vascular smooth muscle cell phenotype[11] and collagen synthesis.[12] ECs respond to stretch by reorganization of the cytoskeleton, where actin filaments align perpendicular to the direction of stretching,[13] and through modified signal transduction[14] and altered gene expression.[15] Importantly, cyclic stretch also induces nitric oxide production through Akt and endothelial nitric oxide synthase (eNOS) signaling in ECs,[16,17] and important factor in vascular dilation.[18] The combined mechanical forces of cyclic stretch and shear stress mediate EC orientation, with elongation along the direction of shear stress and perpendicular to substrate stretch.[9]

While stiffness micro-heterogeneities occur in the subendothelial matrix,[1] and cells are known to respond to complex mechanical cues,[19] the direct impacts of complex patterns of heterogeneity on ECs is unknown. Here, we use computational modeling to simulate the response of a single EC and an EC monolayer to substrate stiffness heterogeneities, and we measure EC basal strain distributions. To best simulate *in vivo* mechanical forces in the artery, substrate displacement and apical cell shear stress were both used as a loading conditions for the model to represent cyclic stretch and blood flow, respectively. EC cytoplasmic strains can be measured *in vitro*, and have been measured previously following substrate stretch and fluid shear stress application.[20,21] However, the EC cytoplasmic strain patterns resulting from complex stiffness micro-heterogeneities found in aged *in vivo* arteries have not been elucidated. Here, we found that heterogeneous substrate stiffness cues, such as are found in aging arteries, can cause increased heterogeneity in basal EC strain.

6.3 Materials and Methods

Ex vivo artery imaging: C57Bl/6 male mice were sacrificed and the thoracic aortas were removed as in our previous study.[1] Arteries were cut longitudinally so that the intima could be imaged *en face*. ECs were stained for VE-cadherin with a primary antibody (Santa Cruz) and a secondary Alexa-Flour 488 (Thermo Fisher). Nuclei were stained with 4',6-diamidino-2-phenylindole (DAPI) (Molecular Probes). A Zeiss laser-scanning confocal microscope was used to image the tissue, and z-stacks were acquired throughout the entire VE-cadherin layer.

Development of single cell and multi-cell models: Confocal images were loaded into Simpleware ScanIP software and used to reconstruct the cell geometries. A representative z-stack was chosen that provided geometries of aligned ECs with minimal imaging artefacts. The representative section also displayed ECs in a relatively 'flat' tissue section to provide the most realistic cell geometries for the model. Three masks were developed to model the three distinct materials: the cytoplasm, nucleus, and VE-cadherin. The middle z-stack image of VE-cadherin was imported into ScanIP software to develop cytoplasm and VE-cadherin masks, copied throughout the full cell thickness. The nuclei geometries were created individually at each z-slice and the final mask was smoothed. The resulting geometries were rotated so that the cells were elongated along the y-axis, and cropped to achieve a rectangular tissue with approximately 15 cells for the multi-cell model. The single cell geometry is approximately 94 μm long, while the multi-cell model is about 160 μm long, and they are both 8-9 μm high in the z-axis. The single cell model was fit with about 17,000 and the multi-cell model with 200,000 tetrahedral elements and the mesh was exported from ScanIP. In Abaqus, the basal surfaces of the cell models were tied node-to-node from the cell to the substrate.

Development of the subendothelial matrix: The subendothelial matrix was created as 3 μm thick, 500 by 500 μm rectangular prism. Substrate material properties were taken from our previous study, where *ex vivo* murine thoracic aortas were probed with atomic force microscopy to determine the spatial profile of micro-scale stiffness of the subendothelial matrix.[1] Mean stiffness values from the young (24.5 kPa) and aged (30 kPa) arteries[1] were used to create the 'compliant' and 'stiff' homogeneous substrates. The simulated heterogeneous substrate was

created as a checkerboard pattern every 10 μm of the compliant (24.5 kPa) and stiff (30 kPa) values. Simulated 'young' and 'aged' matrices were created from the 100 by 100 μm stiffness maps from our previous study,[1] and the maps were repeated in a 5 by 5 pattern to create 500 by 500 μm matrices.

Stretch displacement: The right face of the matrix was displaced 14.2% in the +x direction, as this is the circumferential strain imposed during a cardiac cycle in the mouse aorta.[22] The left face of the matrix was fixed in all directions, and the top and bottom faces were fixed in all directions besides x. The back of the matrix was fixed in the z direction so that the EC(s) would not be displaced downwards through the matrix during loading.

Shear load: To simulate blood shear stress over the EC(s), a perpendicular force of 12 dyn/cm^2, as used in our previous shear experiments,[23] was placed on the apical side of the cell(s) along the direction of elongation, in the -y direction. All apical cell elements received shear stress, and these were hand selected on the rounded top surface in the single cell model.

Cell material properties: Cell material property assumptions were made based on previous experimental and computational studies. The cell cytoplasm, nuclei, and VE-cadherin were all modeled as separate linear elastic materials, and their exact material property inputs were taken from previous studies, as noted in Table 1.[2,8,24-27]

Table 1: Material properties of the endothelial cell and subendothelial matrix linear elastic constitutive models.

Material	Elastic Modulus (kPa)	Poisson's ratio	References
Cell Cytoplasm	0.775	0.495	24–26
Cell Nuclei	5.1	0.3	24–26
VE-cadherin	0.374	0.495	2,8,27
Compliant subendothelial matrix	24.5	0.495	1
Stiff subendothelial matrix	30	0.495	1

Effects of the 'young' and 'aged' matrices on ECs: To test the effects of 'young' and 'aged' matrix stiffness heterogeneities, the single cell and multi-cell models were placed on 30 and 20 different locations throughout the substrates, respectively. Histogram profiles of EC basal strain were created for each location. The mean value at each bin was used to create one histogram profile for each type of matrix and is reported in the figures.

Data analysis: Maximum principal logarithmic strain and von Mises stress values from the substrates and EC(s) at integration points of each element were exported from Abaqus. Prism software (GraphPad) was used to plot the data and perform statistical analysis. To assess heterogeneity, Gaussian distributions were fit to histograms of stress and strain of the young and aged matrices and the strain values at all locations of the cell(s) on the matrix, using Prism

software. Full width at half maximum (FWHM) calculations were calculated from the standard deviations of the Gaussian curves as:

$FWHM = 2\sqrt{2\ln(2)} * standard\ deviation$ [reference 28]

Statistical analysis: Data were assessed for normality using the Shapiro-Wilk normality test. Parametric data were analyzed by Student's t-test for two groups. Non-parametric data were analyzed using the Kruskal-Wallis test for three comparison groups with non-paired data and the Friedman test for three comparison groups with paired data sets all with Dunn's post-hoc analysis to compare all groups. Percent difference between the means was calculated as the difference in means over the average in the means and expressed as a percentage. Error bars are presented as standard error of the mean (SEM) unless otherwise noted.

6.4 Results

Single cell and multi-cell endothelial cell models were created from confocal images and placed on substrates with different stiffness profiles

Confocal z-stacked images were taken of the *ex vivo* murine intima to visualize endothelial cell-cell junctions with VE-cadherin as well as the nuclei (Figure 6.1A). These images were uploaded into Simpleware ScanIP software, and single and multi-cell models were created to geometrically represent the murine tissue (Figure 6.1B). Using Abaqus software, both single and multi-cell models were placed in the middle of a large (500 x 500 μm) substrate, and tied node-to-node to the substrate. Two loading conditions, shear stress parallel to the cell elongation and stretch perpendicular to elongation, were administered at physiological values in the model (Figure

6.1C). Compliant and stiff homogeneous substrates, as well as a heterogeneous checkerboard-patterned substrate, were used to test the effects of heterogeneity on EC strain profiles (Figure 6.1D). Matrices representing 'young' and 'aged' murine tissue, with complex stiffness patterns taken from *ex vivo* tissue data,[1] were also created to represent physiological stiffness substrates.

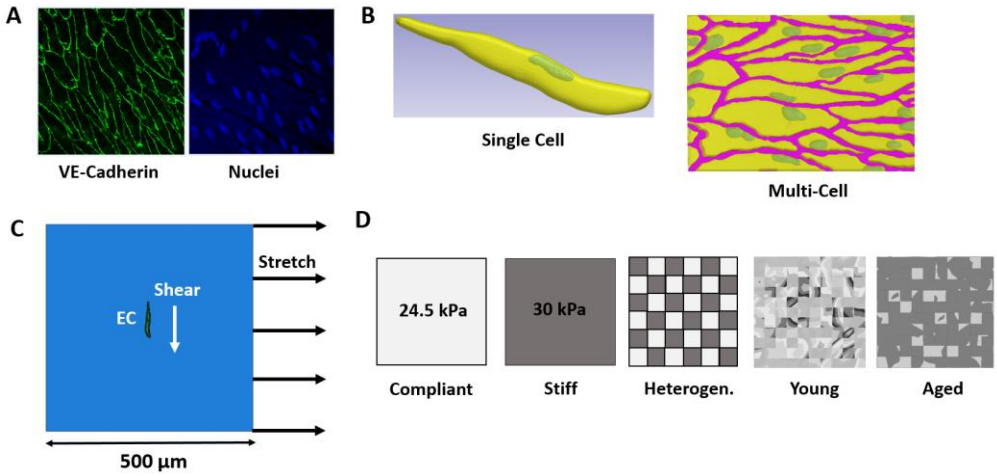

Figure 6.1: Single and multi-cell models were created from confocal images and loaded by substrate deformation and shear stress. (A) *Ex vivo* murine confocal images stained for VE-cadherin and nuclei were used to create (B) single and multi-cell geometries. (C) The cell models were placed on the substrates and the basal cell surface was tied to the top of the substrate. The matrix was stretched perpendicular to the direction of cell elongation and shear was applied parallel to cell elongation on the apical surface. (D) Compliant and stiff substrates as well as a checkerboard heterogeneous substrate were used as characteristic substrates. Matrices representing young and aged tissue were created to represent physiological stiffness heterogeneities.

Substrate stretch has a larger effect on cell strain and stress than apical shear stress

The single cell model was placed on the homogeneous compliant substrate and different loading conditions were applied: substrate stretch and shear flow, or each of these loads alone. Overall, the impact of shear on cell strain and stress was an order of magnitude less than that of substrate stress (Figure 6.2A), most likely due to the node-to-node ties between the basal cell surface and the substrate, and the lack of ties on the apical cell surface. Element strain values from the full thickness of the cell are increased with the application of both substrate stretch and apical cell shear loading. Cellular strains due to stretch only are still an order of magnitude higher than those imposed by shear alone. Lower strains are present in the nucleus due to the higher stiffness of the material. A middle z-plane cut of the cell shows regions of low strain in the nucleus and the order of magnitude difference in the color bar scales for the shear only condition compared to stretch only (Figure 6.2B). Full cell stress patterns demonstrate low values due to shear only loading compared to the conditions that include substrate stretch (Figure 6.2C). The nucleus stresses are higher than the cytoplasm stresses, due to the higher stiffness of the material. Stress profiles of the cell middle z-plane demonstrate increased stress in the nucleus and stresses due to shear only loading an order of magnitude lower than the stretch only condition (Figure 6.2D). While stretch and shear loading are used in concert for the remainder of the study, these data show the relative importance of matrix stretch over shear stress in our model.

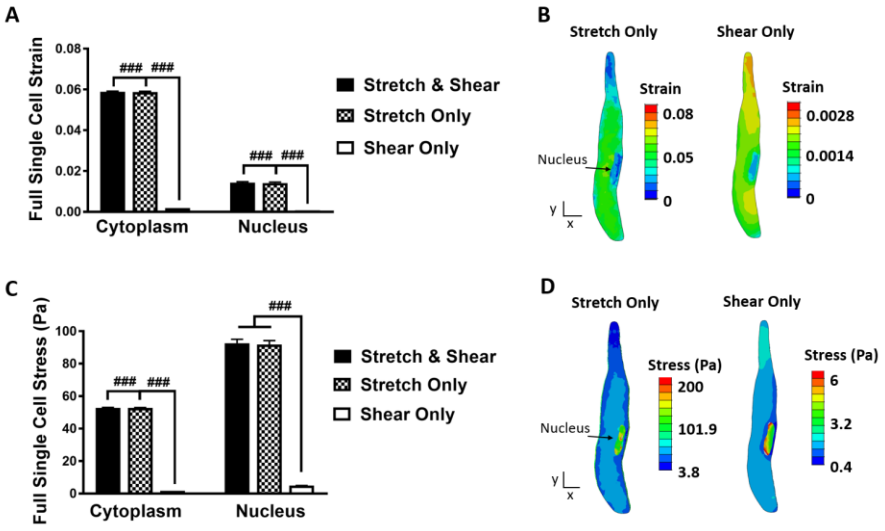

Figure 6.2: Substrate stretch has a larger effect on cellular stress and strain than shear stress on the apical cell surface. (A) The single cell model on the compliant substrate run with different loading conditions shows strains are an order of magnitude higher for loading conditions with substrate stretch than of with shear alone, and this is present in both the cytoplasm and nucleus. (B) Strain profiles in the single cell model from the middle z-plane, indicating the low nucleus strain, and highlights the difference in the range of values in the color scales. (C) Single cell stresses are also an order of magnitude higher for those loading conditions that include substrate stretch, for both the cytoplasm and nucleus. (D) Stress profiles from the middle z-plane in the single cell show the area of high stress in the nucleus and demonstrate difference in magnitude in the color bar scales. Error bars are SEM, ### $p < 0.0005$, Friedman test with Dunn's post-hoc.

After applied displacement, the heterogeneous substrate exhibits a bimodal stress distribution

A physiological stretch of 14.2% was administered to compliant homogeneous (24.5 kPa), stiff homogeneous (30 kPa) and heterogeneous checkerboard-patterned (24.5 / 30 kPa) substrates. While the compliant and stiff homogenous substrates exhibited uniform strain and stress

profiles, the heterogeneous substrates demonstrate a checkerboard pattern (Figures 6.3 A and B). Substrate stiffness caused increased substrate stress, due to the uniform displacement loading, and the mean heterogeneous stress remained in between the two homogeneous substrates (Figure 6.3C). Histograms of substrate stresses demonstrate a rightward shift for the stiff matrix and a bimodal stress distribution for the heterogeneous substrate (Figure 6.3D). These data serve as a proof of concept that the substrates behave as characteristic homogeneous and heterogeneous substrates after displacement, and can be used to model different levels of matrix heterogeneity.

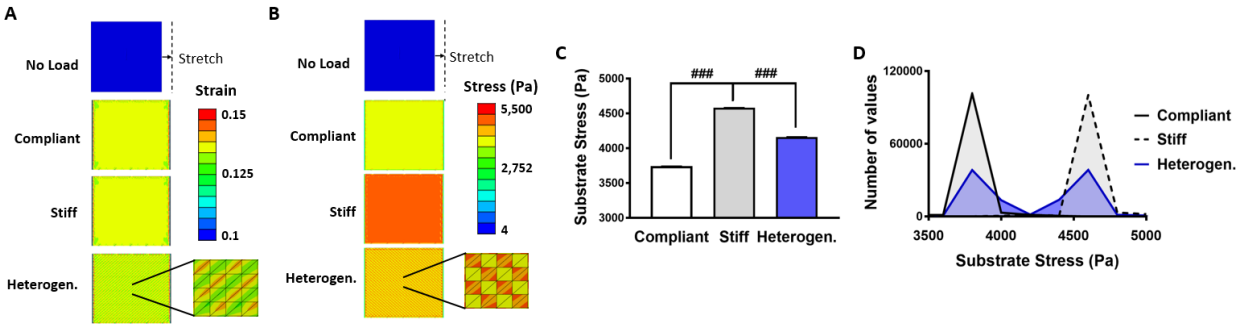

Figure 6.3: Stretched characteristic substrate models demonstrate change in substrate stress with stiffness and heterogeneity. (A) Homogeneous compliant and stiff substrates, and the heterogeneous checkerboard-patterned substrate were stretched using a uniform uniaxial displacement. The checkerboard pattern of stiffness can be detected in the heterogeneous substrate. (B) Substrate stresses were uniform on the homogeneous substrates, and the heterogeneous substrate exhibits its checkerboard pattern. (C) Mean matrix stress increased on the stiff substrate and decreased on the compliant substrate, compared to the heterogenous substrate. (D) Histogram plots demonstrate the rightward shift for substrate stress in the stiff

substrate and a biomodal distribution for the heterogeneous substrate. Error bars are SEM, ### $p < 0.0005$, Kruskal-Wallis test with Dunn's post-hoc.

Substrate heterogeneity causes increased heterogeneity in multi-cell basal strains

Both the single and multi-cell models were placed on the compliant, stiff, and heterogeneous characteristic substrates, and apical shear and substrate stretch were applied. Single cell basal strains increased near the edges and decreased near the rear of the cell (Figure 6.4A). Due to the high edge effects in the multi-cell model, the outer sections of the model were cropped off, and the inner sections were used for analysis (Figure 6.4B). Strain distributions on the multi-cell model demonstrate a stripped pattern in the cytoplasm for cells placed over the checkerboard-patterned heterogeneous substrate (Figure 6.4C). The mean basal strains in the single cell model do not differ between the substrates. However, multi-cell basal cytoplasm strains increased with substrate stiffness and decreased on the complaint substrate, compared to the heterogeneous substrate (Figure 6.4D). Strains from the cropped multi-cell model demonstrate the same pattern of stiffness dependence. As shown by the histogram plots of cell basal cytoplasm strains, while there were no changes in strain heterogeneities in the single cell model (Figure 6.4E), the multi-cell strains increased in heterogeneity on the checkerboard-patterned matrix (Figure 6.4F). Here, we show that cells placed on the heterogeneous checkerboard matrix display a wider range of basal strains.

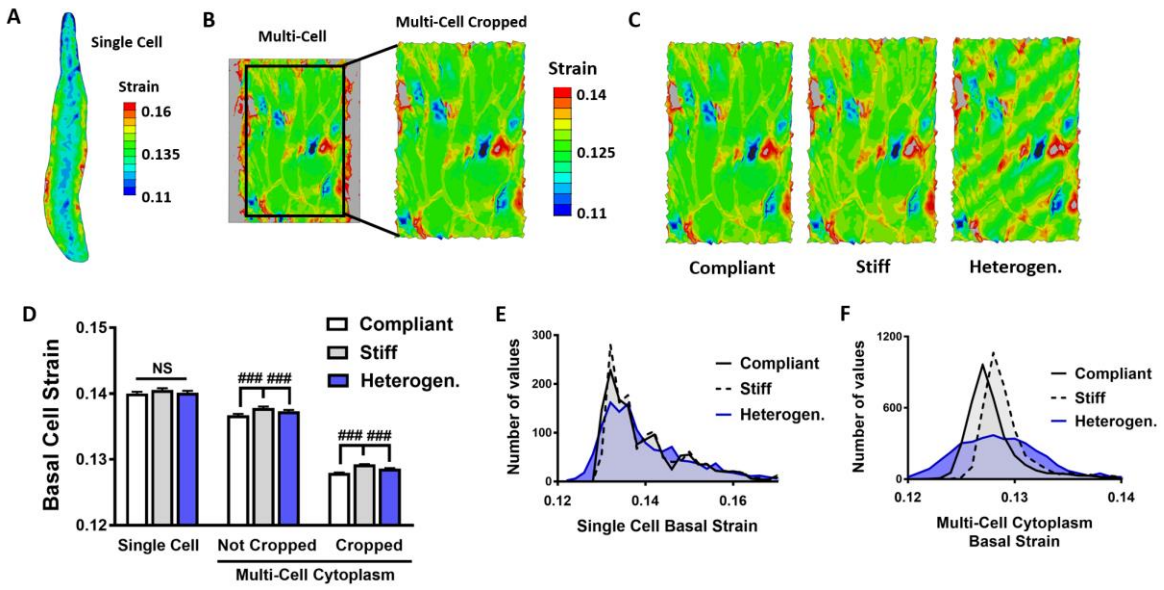

Figure 6.4: The multi-cell model exhibits changes in cytoplasm basal strains due to matrix stiffness and heterogeneity. (A) Patterns of basal strain demonstrate higher values near the edges of the single cell, (B) and especially in the multi-cell model, which was cropped so that only the inner values were analyzed. (C) Stripped regions of strain were displayed in the multi-cell model on the heterogeneous stiffness matrix. (D) The mean basal cytoplasm strains do not change in the single cell model, but change in the multi-cell model, where strain is increased on the stiff matrix and decreased on the compliant matrix in comparison on the heterogeneous matrix. The same trend holds for both the full and cropped multi-cell model values. (E) Histogram plots of single cell cytoplasm strains demonstrate no change in heterogeneity between substrate types, whereas (F) histogram plots of multi-cell cytoplasm strains show a shift to increased values for the stiff matrix and a wider spread of values for the heterogeneous matrix. Error bars are SEM, ### $p < 0.0005$, Kruskal-Wallis test with Dunn's post-hoc.

Matrix mimicking an aged artery exhibits increased heterogeneity compared to the young matrix

Matrices mimicking young and aged murine subendothelial matrix stiffness patterns underwent stretch. After deformation, the matrices displayed complex patterns of heterogeneity where the aged matrix displayed more 'hotspot' regions of strain and stress (Figure 6.5 A and B). Histogram plots of matrix strains and stresses (Figures 6.5 C and D) were fit to Gaussian curves (Figures 6.5 E and F). While the mean strains between the matrices are similar, the mean stresses shift rightward in the aged matrix due to the higher stiffnesses present in the aged matrix. The full width at half maximum (FWHM) values were calculated from the Gaussian distributions and serve as a measure of heterogeneity. The aged matrix was found to exhibit higher FWHM values for both matrix strain and stress (Figure 6.5G). These data indicate that the aged matrix is composed of a more heterogeneous profile of mechanical properties.

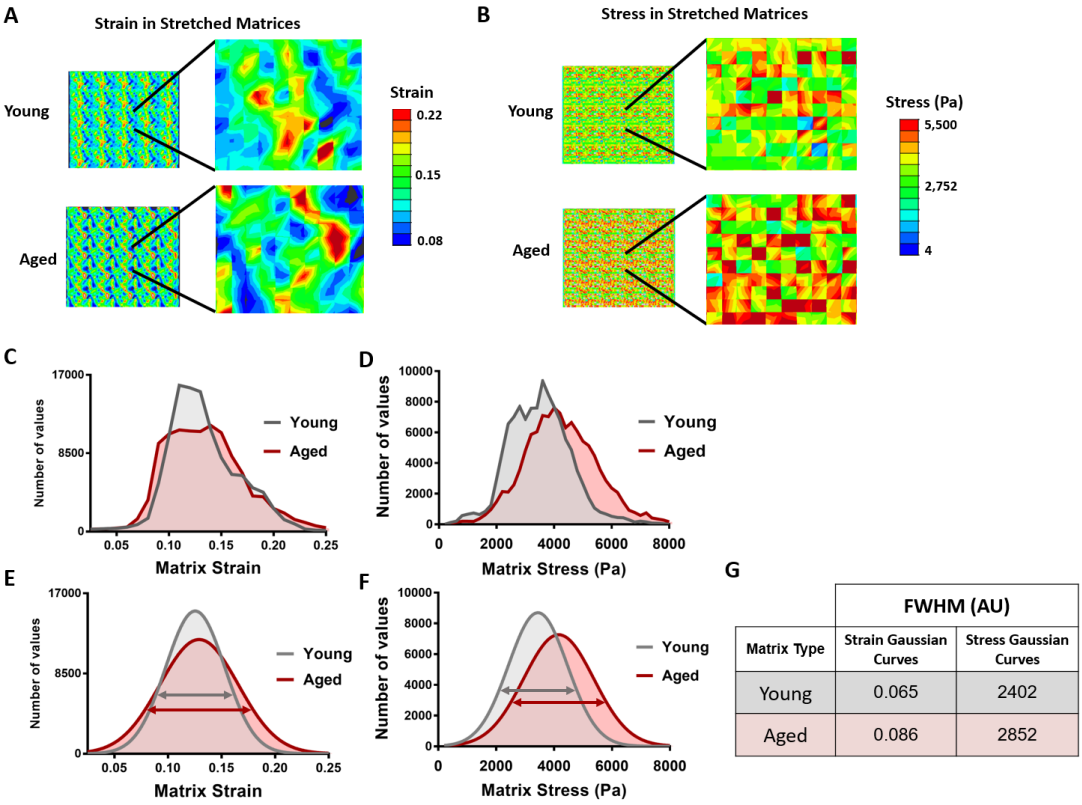

G

	FWHM (AU)	
Matrix Type	Strain Gaussian Curves	Stress Gaussian Curves
Young	0.065	2402
Aged	0.086	2852

Figure 6.5: Matrices representing young and aged murine vessels display higher strain and stiffness heterogeneity in the aged vessel after stretch. The profiles of (A) strain and (B) stress in the stretched matrices indicate complex patterns of heterogeneity, with more 'hotspot' regions in the aged matrix. (C) Histogram profiles of matrix strain and (D) stress, (E,F) were fit with Gaussian curves, showing a rightward shift in matrix stress in the aged matrix. Full width at half maximum (FWHM) values were calculated from the Gaussian distributions as indicated by the arrows. (G) The FWHM values indicate higher heterogeneity in the aged matrix for both strain and stress.

Endothelial cells display more heterogeneous basal strains on an aged matrix

Single and multi-cell models were placed on substrates mimicking 'young' and 'aged' murine subendothelial matrices, and were subjected to substrate stretch and apical cell shear stress. Representative cells show the complex patterns of strain in both models, where the cells on the aged matrix display an increase in 'hotspot' regions (Figures 6.6 A and B). Both models were also placed in 20 – 30 different locations on the young and aged matrices, and the basal cell cytoplasm strain values were recorded in each location and averaged to create histogram plots. Mean histogram plots demonstrate the increased heterogeneity of basal cell strains on the aged matrix (Figures 6.6 C and D). Gaussian curves were fit to the histograms, and heterogeneity was quantified using FWHM, demonstrating increased heterogeneity in EC basal strains on the aged matrix for both models (Figure 6.6E). These data indicate that micro-stiffness heterogeneities present *in vivo* induce heterogeneous basal cell strains.

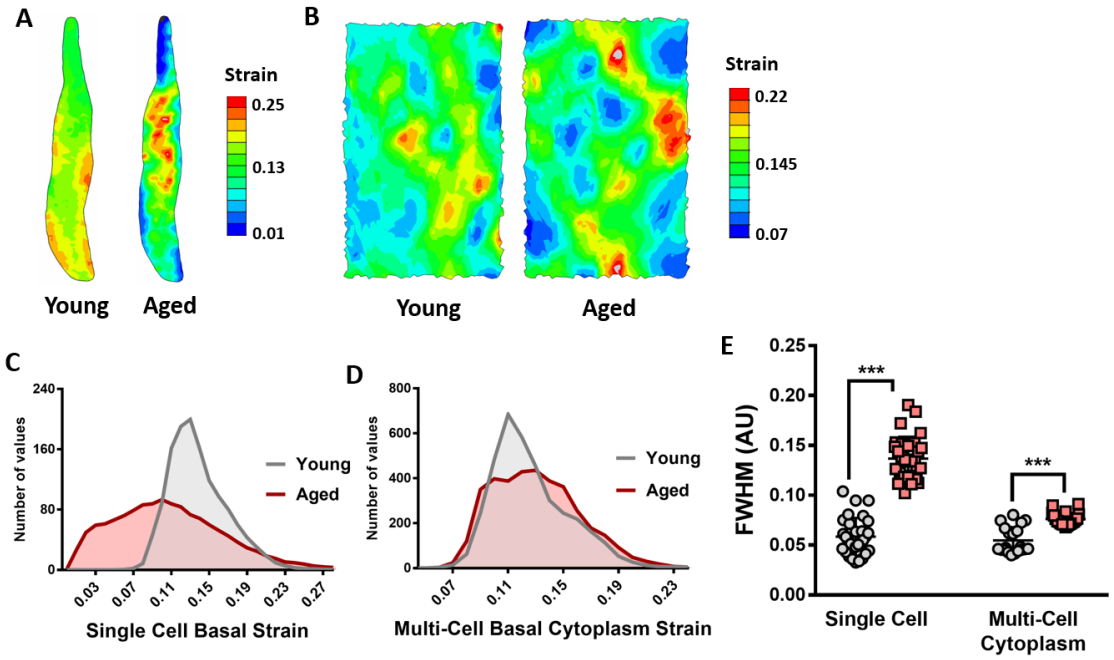

Figure 6.6: Cell strains increase in heterogeneity on an aged matrix. (A) Basal strains in a representative single cell display more strain 'hotspots' in the aged cell, and (B) these 'hotspots' are also exhibited in a representative multi-cell. The mean histogram plots of (C) single and (D) multi-cell basal cytoplasm strains display increased heterogeneity on the aged matrix. Histogram data is represented as mean plots of 30 different matrix locations for the single cell and 20 different locations for the multi-cell. (E) Heterogeneity is quantified by full width at half maximum (FWHM) after histograms were fit to Gaussian distributions, and indicate increased heterogeneity for both cell models placed on the aged matrix. *** $p < 0.0005$, Student's t-test.

Micro-stiffness substrate heterogeneities cause local heterogeneous cell strain and stress profiles

The aged murine subendothelial matrix displays increased micro-scale stiffness heterogeneity,[1] but the effects of these micro-heterogeneities on ECs is unknown. Here, we placed single and multi-cell models on substrates with heterogeneous stiffness, representing 'young' and 'aged'

vessels based on previous data.[1] A representative region with high heterogeneity was selected to demonstrate the local effects of matrix stiffness heterogeneities on ECs (Figure 6.7A). An area of local matrix compliance caused local deformation or 'bulging' of the tissue in this location. An area of high matrix stiffness caused low strain in the matrix, and subsequent low localized cell strain (Figure 6.7B). The same region of high stiffness also causes high stress in the matrix, but low stress in the cell (Figure 6.7C). The reverse is true of a compliant matrix region, where high strain and low stress were present in the matrix, and high strain and stress are present in the cell. These same trends are found for the multi-cell model when placed on the same heterogeneous stiffness region (Figures 6.7 D and E). However, the effects of these stiff and compliant regions are more muted in the multi-cell model, as evidenced by the presence of more moderate values in the color scale in the ECs (see corresponding areas in the pink and navy circles in Figure 6.7). Overall, these data demonstrate that micro-stiffness heterogeneities in the matrix influence the local strain and stress distributions in ECs.

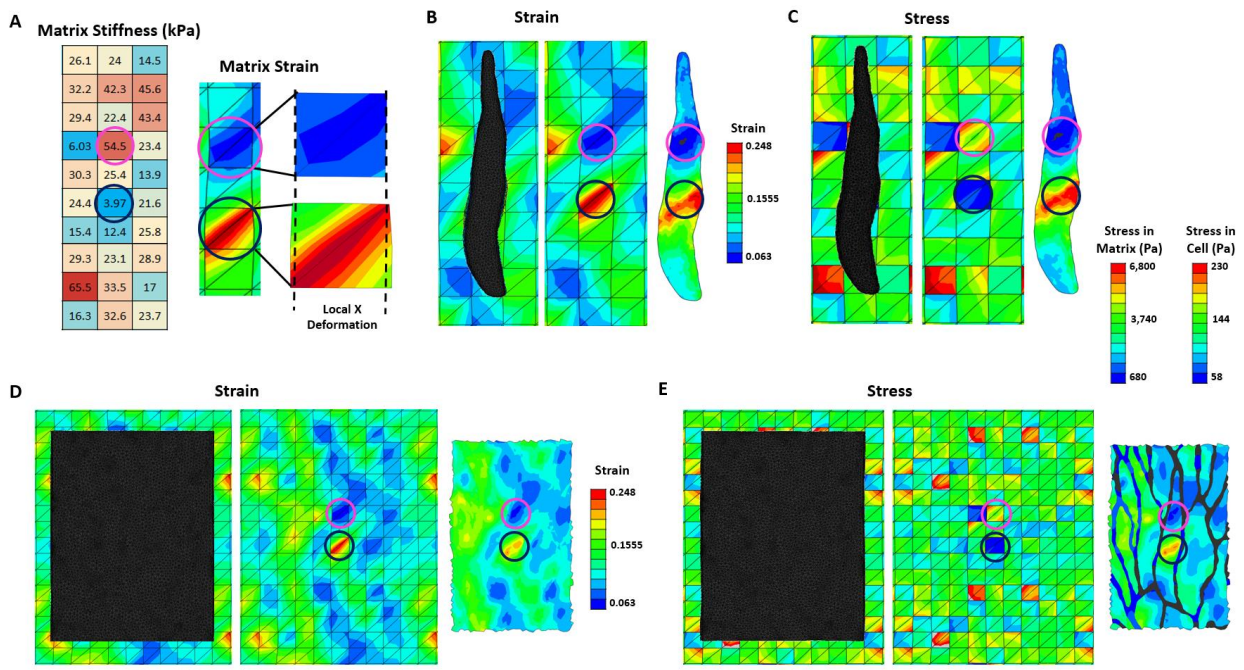

Figure 6.7: Micro-stiffness heterogeneities present in the matrix cause local heterogeneous cell strain and stress. (A) A heterogeneous subendothelial matrix stiffness region from a previous study[1] was chosen. The area of increased substrate stiffness (outlined in the pink circle), induces decreased matrix strain. The area of matrix compliance (outlined in the black circle), induces increased matrix strain and local x deformation, where this region bulges due to the high strain. For the region of high local stiffness, (B) matrix and cell strain decreased, whereas (C) matrix stress increased, and cell stress decreased. The region of matrix compliance induces opposite strain and stress profiles. (D) Multi-cell models were placed in the same matrix location, and demonstrated the same strain and (E) stress patterns.

The same cell in the single or multi-cell models displays similar strain profiles

The single cell model was originally created by cropping out the center cell of the multi-cell model, and therefore the same cell geometry is present in the center of the multi-cell model as

is used in the single cell model. As seen in Figure 6.7, both models were placed on a matrix region with high stiffness heterogeneity, and the local basal strains were examined. Here, we compare the strains exhibited in the same cell geometry when it is placed alone or surrounded by other cells on the region of high heterogeneity. Between the two models, cell basal strains and stresses display a similar range of values; the mean basal strains are 12.2% different, and the mean stresses 8.5% different between the same cell in both models (Figures 6.8 A and B). Basal cell strain and stress profiles are similar between the two models, although values are slightly lower in the cell when it is in the multi-cell model (Figures 6.8 C and D). The slight geometrical differences in the cell is due to the addition of VE-cadherin in the multi-cell model. These results indicate that the single and multi-cell models result in similar cell strain and stress outputs.

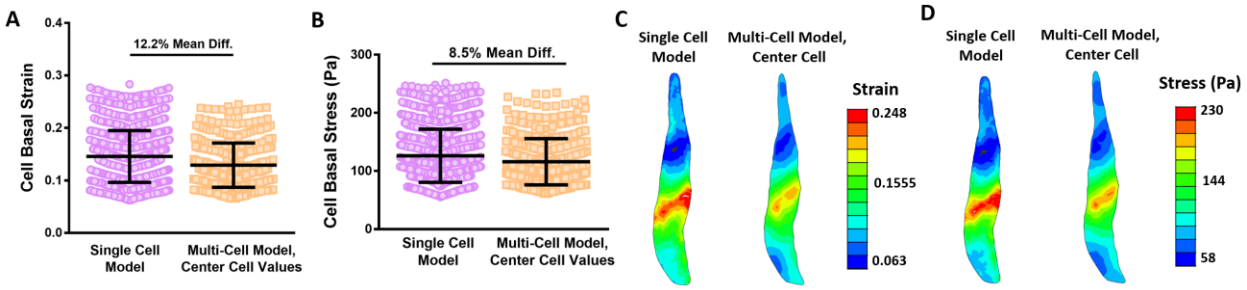

Figure 6.8: The same cell geometry used in the single or multi-cell model demonstrates similar basal strain and stress profiles. (A) For the same cell geometry in both models, the mean strain and (B) stress differences between the single and multi-cell models differ by only 12.2% and 8.5%, respectively. The profiles of (C) strain and (D) stress throughout the cell indicate similar regions of high and low values in both models.

6.5 Discussion

Here, we demonstrate in a computational model that stiffness heterogeneities in the substrate induce increased heterogeneity in basal EC strains. Previously, the artery has been shown to increase in heterogeneous stiffness with age,[29] and this specifically occurs in the subendothelial matrix.[1] Recently, in one study of the effects of heterogeneous substrate cues, stem cells placed on dual-rigidity micropillars displayed heterogeneous traction forces *in vitro*.[19] However, the effects of complex patterns of stiffness micro-heterogeneities on ECs had not been elucidated. Our main finding is that ECs on a simulated aged subendothelial matrix display increased EC strain heterogeneity. These data, demonstrating the effects of complex substrate mechanics on EC strains, are a starting point for the assessment of EC mechanical responses and possible phenotypic changes to complex physiological stiffness profiles.

Our results indicate a close connection between local substrate deformation and local EC strain, which is most apparent in regions of high stiffness heterogeneity. Previously, analysis of ECs after cyclic stretch indicated that the cell cytoskeletal strains closely follow those exhibited by the deformation of the substrate.[21] We expand on this knowledge by assessing the cellular response to local regions of increased and decreased matrix deformation. In our simulation of cells on a high-heterogeneity region, a small patch of local matrix compliance exhibited increased matrix strain and deformation, which translated into increased local EC strain. Moreover, we also indicate that intracellular strains in the multi-cell model are similar to those in the single cell model, indicating that the effects of complex patterns of substrate deformation also effect cells in larger cell monolayers.

Our work uses substrate stretch and shear stress as the loading conditions to understand EC response to substrate stiffness heterogeneities. Interestingly, the combined effects of substrate stiffness and stretch on cellular mechanotransduction has recently been studied *in vitro*. In a study by Quinlan *et al.* (2011), cells remained rounded on a compliant gel until induction of cyclic stretch, which caused them to spread to the size of static cells on a stiff substrate. The authors propose that the mechanism of cellular mechanosensing may be similar for detecting substrate stiffness and substrate stretch.[30] This hypothesis was tested in a computational model by Parameswaran *et al*. (2014), which indicates that active reorganization of actomyosin structures allows for both substrate stiffness and stretch mechanotransduction by cells.[31] These studies, along with our results here, indicate the importance of understanding the effects of multiple mechanical cues on cellular mechanotransduction.

Our data indicate that cell strain, transferred through substrate stretch into the EC, is dependent on substrate stiffness in localized regions. However, the possible implications of these intracellular strain profiles on vascular function have not been determined. Interestingly, a recent study by Dan *et al.* (2016) revealed that substrate stiffness and cyclic stretch in concert mediate EC monolayer disruption to thrombin-induced barrier disruption.[32] In this study, ECs plated on 15 kPa hydrogels also exhibited larger cell-cell gaps than those on 5 kPa gels, but this effect was attenuated by cyclic strain application. While EC barrier integrity is known to be mediated by substrate stiffness-dependent actomyosin contractility,[3,33] and now by stiffness and cyclic stretch in concert,[32] the effects of complex heterogeneous patterns of stiffness remains unknown. Future

studies should examine the effects of local regions of stiffness heterogeneity on monolayer function and barrier integrity, as we indicate that these regions display heterogeneous basal strain profiles.

In our study, shear stress was minimally impactful on EC strains and stresses, as values due to shear stress alone were an order of magnitude lower than those caused by substrate displacement. This is most likely due to the node-to-node ties between the substrate and the cell, whereas no such ties were placed on the apical surface of the cell. However, shear plays a vital role in vascular health through the mechanosensitivity of ECs and their proteins. Shear flow on an EC monolayer orients the direction of EC elongation,[23] and can cause small cytoplasmic deformations.[25] We have previously demonstrated that the combined effects of shear stress and substrate rigidity affect EC junctional stability and nitric oxide production through changes in RhoA and eNOS activation.[23] Flow can also induce cytoskeletal remodeling and mediate the mechanical tension across cell-cell junctions through proteins such as platelet-endothelial cell adhesion molecule-1 (PECAM-1) and VE-cadherin.[34] Therefore, given the importance of shear stress in mechanical loading of ECs, our experiments were carried out under conditions of combined substrate stretch and shear stress.

Careful consideration was taken into precise loading displacement for our model of the murine aorta. The human aorta experiences about 10% strain,[35] and many cyclic stretch studies use 5 – 12% stretch, representing the low physiologic regime.[10,36] Stretch values above 20% are considered pathological, representing hypertension, and can damage cells.[37,38] Other studies will

use a range of strain values, from 2 – 25,[9,21] providing the effects for different conditions of intraluminal pressure. In fact, in one study, while 24% strain stimulated eNOS activity, 10% strain did not have the same effect.[16] Given that our model uses subendothelial matrix stiffness profiles from C57Bl/6 thoracic aortas,[1] we decided to impose a uniaxial 14.2% displacement on the substrate to mimic the circumferential strain in the mouse aorta of C57Bl/6-background mice.[22]

6.6 Conclusions

To assess the impact of substrate stiffness heterogeneities on endothelial cell strain, computational models were created of single and multiple endothelial cells on substrates with different patterns of stiffness heterogeneities. Upon substrate stretch and apical cell shear stress loading, the substrate mimicking an aged artery experienced an increased heterogeneous strain distribution, which resulted in increased heterogeneous strain distributions within the cells themselves. Overall, our data demonstrate that endothelial cells respond to the subendothelial matrix stiffness heterogeneities present in aged arteries.

6.7 References

1. Kohn, J. C. *et al.* Mechanical heterogeneities in the subendothelial matrix develop with age and decrease with exercise. *J. Biomech.* **49,** 1447–1453 (2016).
2. Huynh, J. *et al.* Age-related intimal stiffening enhances endothelial permeability and leukocyte transmigration. *Sci. Transl. Med.* **3,** 112ra122 (2011).
3. Krishnan, R. *et al.* Substrate stiffening promotes endothelial monolayer disruption through enhanced physical forces. *Am. J. Physiol. Cell Physiol.* **300,** C146–C154 (2011).

4. Lusis, A. Atherosclerosis. *Nature* **407,** 233–241 (2000).
5. Lo, C. M., Wang, H. B., Dembo, M. & Wang, Y. L. Cell movement is guided by the rigidity of the substrate. *Biophys. J.* **79,** 144–152 (2000).
6. Valent, E. T., van Nieuw Amerongen, G. P., van Hinsbergh, V. W. M. & Hordijk, P. L. Traction force dynamics predict gap formation in activated endothelium. *Exp. Cell Res.* (2016).
7. Reinhart-King, C. A., Dembo, M. & Hammer, D. A. Cell-cell mechanical communication through compliant substrates. *Biophys. J.* **95,** 6044–6051 (2008).
8. Barry, A. K., Wang, N. & Leckband, D. E. Local VE-cadherin mechanotransduction triggers long-ranged remodeling of endothelial monolayers. *J. Cell Sci.* **128,** 1341–1351 (2015).
9. Sinha, R. *et al.* Endothelial cell alignment as a result of anisotropic strain and flow induced shear stress combinations. *Sci. Rep.* **6,** 29510 (2016).
10. Birukov, K. G. Cyclic stretch, reactive oxygen species, and vascular remodeling. *Antioxid. Redox Signal.* **11,** 1651–67 (2009).
11. Birukov, K. G. *et al.* Intraluminal pressure is essential for the maintenance of smooth muscle caldesmon and filamin content in aortic organ culture. *Arterioscler. Thromb. Vasc. Biol.* **18,** 922–927 (1998).
12. Leung, D. Y., Glagov, S. & Mathews, M. B. Cyclic stretching stimulates synthesis of matrix components by arterial smooth muscle cells in vitro. *Science* **191,** 475–477 (1976).
13. Civelekoglu, G., Tardy, Y. & Meister, J. J. Modeling actin filament reorganization in endothelial cells subjected to cyclic stretch. *Bull. Math. Biol.* **60,** 1017–1037 (1998).
14. Von Offenberg Sweeney, N. *et al.* Cyclic strain-mediated regulation of endothelial matrix metalloproteinase-2 expression and activity. *Cardiovasc. Res.* **63,** 625–634 (2004).

15. Du, W., Mills, I. & Sumpio, B. E. Cyclic strain causes heterogeneous induction of transcription factors, AP-1, CRE binding protein and NF-kB, in endothelial cells: Species and vascular bed diversity. *J. Biomech.* **28,** 1485–1491 (1995).
16. Awolesi, M., Widmann, M., Sessa, W. & Sumpio, B. Cyclic strain increases endothelial nitric oxide synthase activity. *Surgery* **116,** 439–444 (1994).
17. Kuebler, W. M. *et al.* Stretch activates nitric oxide production in pulmonary vascular endothelial cells in situ. *Am. J. Respir. Crit. Care Med.* **168,** 1391–1398 (2003).
18. Cohen, R. A. *et al.* Mechanism of nitric oxide–induced vasodilatation. *Circ. Res.* **84,** 210–219 (1999).
19. Breckenridge, M. T., Desai, R. A., Yang, M. T., Fu, J. & Chen, C. S. Substrates with engineered step changes in rigidity induce traction force polarity and durotaxis. *Cell. Mol. Bioeng.* **7,** 26–34 (2014).
20. Helmke, B. P., Rosen, A. B. & Davies, P. F. Mapping mechanical strain of an endogenous cytoskeletal network in living endothelial cells. *Biophys. J.* **84,** 2691–2699 (2003).
21. Caille, N., Tardy, Y. & Meister, J. J. Assessment of strain field in endothelial cells subjected to uniaxial deformation of their substrate. *Ann. Biomed. Eng.* **26,** 409–416 (1998).
22. Trachet, B. *et al.* Performance comparison of ultrasound-based methods to assess aortic diameter and stiffness in normal and aneurysmal mice. *PLoS One* **10,** e0129007 (2015).
23. Kohn, J. C. *et al.* Cooperative effects of matrix stiffness and fluid shear stress on endothelial cell behavior. *Biophys. J.* **108,** 471–478 (2015).
24. Caille, N., Thoumine, O., Tardy, Y. & Meister, J.-J. Contribution of the nucleus to the mechanical properties of endothelial cells. *J. Biomech.* **35,** 177–187 (2002).

25. Ferko, M. C., Bhatnagar, A., Garcia, M. B. & Butler, P. J. Finite-element stress analysis of a multicomponent model of sheared and focally-adhered endothelial cells. *Ann. Biomed. Eng.* **35,** 208–223 (2007).

26. Yao, Y., Lacroix, D. & Mak, A. F. T. Effects of oxidative stress-induced changes in the actin cytoskeletal structure on myoblast damage under compressive stress: confocal-based cell-specific finite element analysis. *Biomech. Model. Mechanobiol.* **15,** 1–14 (2016).

27. Nelson, C. M. *et al.* Emergent patterns of growth controlled by multicellular form and mechanics. *Proc. Natl. Acad. Sci. U. S. A.* **102,** 11594–11599 (2005).

28. Weisstein, E. W. Full Width at Half Maximum. *MathWorld--A Wolfram Web Resource* Available at: http://mathworld.wolfram.com/FullWidthatHalfMaximum.html. (Accessed: 21st April 2017)

29. Graham, H. K. *et al.* Localised micro-mechanical stiffening in the ageing aorta. *Mech. Ageing Dev.* **132,** 459–467 (2011).

30. Quinlan, A. M., Sierad, L. N., Capulli, A. K., Firstenberg, L. E. & Billiar, K. L. Combining dynamic stretch and tunable stiffness to probe cell mechanobiology in vitro. *PLoS One* **6,** e23272 (2011).

31. Parameswaran, H., Lutchen, K. R. & Suki, B. A computational model of the response of adherent cells to stretch and changes in substrate stiffness. *J. Appl. Physiol.* **116,** 825–834 (2014).

32. Dan, A., Huang, R. B. & Leckband, D. E. Dynamic Imaging Reveals Coordinate Effects of Cyclic Stretch and Substrate Stiffness on Endothelial Integrity. *Ann. Biomed. Eng.* 1–13 (2016).

33. Huynh, J. *et al.* Age-related intimal stiffening enhances endothelial permeability and

leukocyte transmigration. *Sci. Transl. Med.* **3,** 112ra122 (2011).

34. Conway, D. E. *et al.* Fluid shear stress on endothelial cells modulates mechanical tension across VE-cadherin and PECAM-1. *Curr. Biol.* **23,** 1024–1030 (2013).
35. Isnard, R. N. *et al.* Pulsatile diameter and elastic modulus of the aortic arch in essential hypertension: A noninvasive study. *J. Am. Coll. Cardiol.* **13,** 399–405 (1989).
36. Jufri, N. F., Mohamedali, A., Avolio, A. & Baker, M. S. Mechanical stretch: physiological and pathological implications for human vascular endothelial cells. *Vasc. Cell* **7,** 8 (2015).
37. Anwar, M. A., Shalhoub, J., Lim, C. S., Gohel, M. S. & Davies, A. H. The effect of pressure-induced mechanical stretch on vascular wall differential gene expression. *J. Vasc. Res.* **49,** 463–478 (2012).
38. Haga, J. H., Li, Y.-S. J. & Chien, S. Molecular basis of the effects of mechanical stretch on vascular smooth muscle cells. *J. Biomech.* **40,** 947–960 (2007).

CHAPTER 7

CONCLUSIONS AND FUTURE DIRECTIONS

7.1 Conclusions

As our understanding of cardiovascular stiffness continues to evolve, the impacts of micro-scale subendothelial matrix rigidity will become more apparent. Our studies expand on the understanding of how substrate stiffness impacts endothelial cells (ECs) through the combined effects of physiological shear stress and matrix rigidity on EC function. Also, while in vivo most studies currently focus on bulk mechanical properties of the aorta to assess cardiovascular risk, we expanded upon the knowledge of the subendothelial matrix under these conditions. Specifically, we determined the impacts of cardiovascular risk factors such as increased age, lack of exercise, and poor diet consumption on subendothelial matrix mechanics. We also developed an *in silico* model which indicates that ECs are influenced by heterogeneous patterns of micro-scale stiffness. Taken together, the data emphasize the importance of subendothelial matrix mechanics on cardiovascular health.

In Chapter 2, we demonstrated that shear stress and substrate stiffness can work in concert to impact EC monolayers. Using an in vitro platform, ECs were placed on matrices of different rigidities and were exposed to fluid shear stress. We found that after an hour of shear induction, Rho A activation was upregulated in ECs placed on stiff matrices compared to those on compliant matrices. Shear stress also induced nitric oxide production on EC monolayers, which was

attenuated by increased matrix rigidity. Our data indicate that the duel effect of fluid shear stress in the atheroprotective regime and a compliant subendothelial matrix reduces Rho A activity and promotes nitric oxide availability.

In Chapter 3, a murine model was used to demonstrate the mechanical heterogeneities in the subendothelial matrix. This study used atomic force microscopy to probe the subendothelial matrix to create maps of matrix stiffness, which demonstrated an increase in overall stiffness and increased stiffness heterogeneity with age. In this study, we also found that the gold standard bulk mechanical stiffness measurement, pulse wave velocity, was correlated to subendothelial matrix stiffness in these mice cohorts. The subendothelial matrix is a complex tissue, and importantly, this layer increases in overall stiffness heterogeneity and spatial stiffness heterogeneity with age. We also discovered that overall stiffening and the presence of stiffness heterogeneities can be mediated through the application of a swimming exercise regimen.

Given the importance of the exercise regimen in the Chapter 3 study, we then asked the question: how long do the positive benefits of exercise on the subendothelial matrix last? In Chapter 4, aged mice performed an exercise regimen and then a rest period of the same length. Here, we found that bulk arterial stiffness decreased with exercise, but returned to baseline after only half the amount of time of the exercise regimen. The exercise regimen also improved subendothelial matrix rigidity and cardiac function, but after the full rest period, these values returned to baseline. These results indicate the importance of continued exercise to maintain proper cardiovascular health. During this study, we also discovered that the subendothelial matrix elastic

modulus is loading-rate dependent. In terms of cardiac health, ejection fraction followed the same trends as vascular stiffness with exercise and rest. Finally, we also examined possible causes of arterial stiffening, and indicated that intimal collagen and aortic advanced glycation end product content follow the same trends as micro- and macro-scale stiffness in these mice cohorts. The distribution of intimal collagen values within each tissue also increased in sedentary animals compared to exercised animals, which may indicate a possible association between subendothelial matrix stiffness heterogeneities and intima collagen content.

In Chapter 5, we expanded our murine studies to include consumption of a Western diet as a cause of increased subendothelial matrix stiffening. In this study, we found that Western diet consumption not only increased mouse body weight and blood pressure, but also caused macro- and micro-scale arterial stiffening. A swimming exercise regimen mitigated subendothelial matrix stiffness, but did not effectively decrease bulk arterial stiffness. A change back to a normal diet reversed the effects of Western diet consumption on both the macro- and micro-scale, indicating that diet change had a larger effect on bulk arterial stiffness than exercise. This study was insightful, as it indicated that macro- and micro-scale stiffness do not always follow the same trends, unlike the correlation present in Chapter 3 between macro- and micro-scale stiffness with age and exercise.

Finally, in Chapter 6, we demonstrated in an *in silico* model that subendothelial matrix stiffness heterogeneities, as are found in aged mice, impact EC basal strains. Single and multi-cell computational models of ECs on homogeneous and heterogeneous matrices were mechanically

loaded by substrate stretch and apical cell shear. In this model, we found that cells on heterogeneous matrices displayed increased heterogeneity in basal strain. This trend also extended to the physiological tissue sample, where cells placed on a representative 'aged' murine subendothelial matrix, as measured in the Chapter 3 study, showed a resulting increase in heterogeneity of basal strains. In areas of high heterogeneity, detailed micro-scale analysis demonstrated that local regions of high matrix stiffness induce local regions of low strain in the cell. This study indicates that subendothelial matrix heterogeneities found in vivo, such as are caused by aging, may influence EC strain distributions.

In this thesis, we explored the effects of micro-scale arterial stiffening on ECs through our in vitro study of shear stress and substrate stiffness. Our in vivo studies provided a more complete picture of the impacts of age, exercise and diet on subendothelial matrix stiffness. Finally, we developed an *in silico* model to better understand the EC basal strains resulting from complex matrix stiffness patterns. Taken as a whole, this work places a strong emphasis on subendothelial matrix stiffness and stiffness heterogeneities and the impacts of these changes on an EC monolayer.

7.2 Future Directions

In this dissertation, we examined how the mechanics of the subendothelial matrix are altered by cardiovascular risk factors such as age, diet, and lack of exercise. We also found that ECs are influenced by shear stress and substrate stiffness in concert, and may be effected by heterogeneous substrate stiffness patterns. Although the work in this dissertation contributes to

the understanding of subendothelial matrix mechanics and its impact on ECs, there are questions that remained unanswered for future studies to investigate.

In Chapter 2, we used an *in vitro* platform to find that ECs are impacted by shear stress and substrate stiffness in concert and that these factors can impact the production of nitric oxide (NO). However, during the aging process, subendothelial matrix stiffening is not the only change occurring in the vessel. Previous work has demonstrated that aged ECs are more prone to senescence[1] and apoptosis,[2] and ECs aged in culture demonstrate decreased levels of endothelial nitric oxide synthase and S-nitric oxide.[3] Given these data, we hypothesize that aged ECs do not respond to matrix substrate cues to the same effect as they did when they were young cells. Future studies to test the impacts of age itself on EC mechanotransduction would elucidate the multiple impacts that aging has on EC function. Future studies could study this effect by removing young and aged *in vivo* ECs and measuring single and monolayer functionality of these cell groups. Another physiological circumstance that affects EC function is disrupted blood flow, especially at bifurcation points. Oscillating patterns of shear stress imposed on ECs can produce an atheroprone phenotype, where NO production is significantly decreased.[4,5] It is hypothesized that the combined effects of substrate stiffness and oscillating shear stress would further detriment single and monolayer EC function. Studies measuring the effects of additional physiological cues on EC function, such as through cellular aging or oscillating shear stress, would provide further insight into *in vivo* EC function and would complement this thesis work.

In Chapters 3, 4, and 5, we studied the impacts of common cardiovascular risk factors on subendothelial matrix stiffening. Specifically, we found that following exercise treatment, both decreased intimal collagen content and subendothelial matrix destiffening occurred. However, in our study of a high-fat, high-sugar diet, no changes were detected in intimal collagen content after Western diet consumption. Our data indicate that intima collagen content may play a role in micro-scale matrix stiffening in certain physiological settings. Although we present intima collagen as a possible cause for this stiffening in the context of exercise, the specific mechanisms for subendothelial matrix stiffening and heterogeneous stiffening remain unknown. Collagen is a major component of the intima extracellular matrix (ECM),[6] and it is known to modulate arterial stiffness on the macro-scale.[7–9] Therefore, these data lead to the hypothesis that changes in subendothelial matrix stiffness are caused by changes in collagen content in the intima layer. Elastin is another ECM component which may have an effect on subendothelial matrix stiffening, and should be investigated. However, given that the main contribution of elastin to the artery is in the elastic lamina, which is beyond the subendothelial matrix, we propose that collagen would play a larger role in changes to subendothelial matrix stiffness. Future studies examining the role of ECM proteins in subendothelial matrix stiffness with altered diet, exercise and aging would nicely supplement this dissertation work.

We demonstrated in Chapter 3 that increased heterogeneity in subendothelial matrix stiffness occurs with age. We also presented a technique in Chapter 4 to image collagen content in the intima *en face* using structured illumination microscopy. However, it remains unknown whether the small regions of increased collagen content displayed in the structured illumination

microscopy images directly correlate to stiff regions in the subendothelial matrix. These data lead us to hypothesize that changes in subendothelial matrix stiffness heterogeneity are caused by micro-scale regions of increased collagen content; future studies which examine these heterogeneous regions using imaging techniques would complement this dissertation work. Other imaging techniques, such as multi-photon imaging, and transmission electron microscopy may be used in additional studies to qualitatively examine changes in ECM components as the subendothelial matrix stiffens heterogeneously. Comparisons of indentation stiffness maps with the hotspots of intima ECM proteins would provide a possible correlation between micro-scale stiffness heterogeneities and ECM content. Another possible cause for heterogeneous stiffening is through heterogeneous ECM crosslinks such as advanced glycation end products (AGEs) and tissue transglutaminase, which are known to stiffen arteries.[10,11] Additional experiments targeting the causes of heterogeneous stiffening and correlations to ECM component structure would further enhance the findings presented in this dissertation.

In Chapter 5, we discovered an interesting trend in micro- versus macro-scale stiffness; while exercise after high-fat, high-sugar diet consumption mitigated subendothelial matrix stiffening, pulse wave velocity (PWV) did not significantly decrease. This is the first time we demonstrate a stiffness change on the micro-scale occurring prior to a macro-scale stiffness change. Other work has demonstrated that EC phenotype can be altered, such as through cellular de-stiffening,[12] and endothelium-dependent dilation,[13] without seeing a change in macro-scale stiffness. Therefore, these data lead to the hypothesis that changes are occurring in the EC monolayer prior to detection by macro-scale stiffness metrics. In addition, the coordination between structural and

functional properties of the arteries and how these influence clinical stiffness metrics, such as PWV, remains an area of active research.[14,15] Future studies should analyse the links between micro-scale structural changes, such as alterations in intima ECM proteins, functional changes, such as EC production of NO, and macro-scale stiffness measurements, such as PWV. Better detection systems for EC health and understanding its relation to macro-scale function will benefit the field and enhance this thesis work.

In Chapter 6, we found that age alters EC strain patterns. While we focus primarily on the cardiovascular risk factors of age, exercise, and diet in this thesis, hypertension, or increased blood pressure, is another major cardiovascular risk factor.[16] Recently, it was demonstrated *in vivo* that hypertension occurs following vessel stiffening,[17] although there is conflicting literature on the sequence of hypertension and arterial stiffness.[14] Therefore, studies examining the impacts of stiffness on ECs should also consider the effects of hypertension simultaneously. We hypothesize that hypertensive cyclic stretch would further enhance the disrupted strain patterns imposed by heterogeneous stiffness cues. Future studies using a computational model could alter the amount of cyclic stretch imposed on ECs and measure EC strain patterns formed in response. Future work examining the relationship between vascular stiffening, hypertension, and their dual effects on ECs would add to this thesis work.

Overall in this thesis, we underscored the importance of understanding subendothelial matrix mechanics. First, we examined the effects of substrate stiffness and shear stress in concert on ECs *in vitro*. Then, we demonstrated the changes in micro-scale stiffening of the subendothelial

matrix with age, exercise and diet, and found that the subendothelial matrix is a complex mechanical tissue. Finally, we used an *in silico* model of substrate stiffness heterogeneities to explore their effects on EC strain profiles. Future studies in this field may provide further insights into the causes for micro-scale heterogeneous stiffening and examine the response of ECs to different cardiovascular risk factors.

7.3 References

1. Donato, A. J., Morgan, R. G., Walker, A. E. & Lesniewski, L. A. Cellular and molecular biology of aging endothelial cells. *J. Mol. Cell. Cardiol.* 122–135 (2015). doi:10.1016/j.yjmcc.2015.01.021
2. Asai, K. *et al.* Peripheral vascular endothelial dysfunction and apoptosis in old monkeys. *Arterioscler. Thromb. Vasc. Biol.* **20,** 1493–1499 (2000).
3. Hoffmann, J. *et al.* Aging enhances the sensitivity of endothelial cells toward apoptotic stimuli: important role of nitric oxide. *Circ. Res.* **89,** 709–715 (2001).
4. Traub, O. & Berk, B. C. Laminar shear stress: mechanisms by which endothelial cells transduce an atheroprotective force. *Arterioscler. Thromb. Vasc. Biol.* **18,** 677–685 (1998).
5. Chien, S. Effects of disturbed flow on endothelial cells. *Ann. Biomed. Eng.* **36,** 554–562 (2008).
6. Murata, K., Motayama, T. & Kotake, C. Collagen types in various layers of the human aorta and their changes with the atherosclerotic process. *Atherosclerosis* **60,** 251–262 (1986).
7. Shadwick, R. E. Mechanical design in arteries. *J. Exp. Biol.* **202,** 3305–3313 (1999).
8. Fleenor, B. S., Marshall, K. D., Durrant, J. R., Lesniewski, L. A. & Seals, D. R. Arterial stiffening

with ageing is associated with transforming growth factor-β1-related changes in adventitial collagen: reversal by aerobic exercise. *J. Physiol.* **588,** 3971–3982 (2010).

9. Díez, J. in *Atherosclerosis, Large Arteries and Cardiovascular Risk* (eds. Safar, M. & Frohlich, E.) **44,** 76–95 (2007).

10. Steppan, J. *et al.* Exercise, vascular stiffness, and tissue transglutaminase. *J. Am. Heart Assoc.* **3,** e000599 (2014).

11. Goldin, A., Beckman, J. A., Schmidt, A. M. & Creager, M. A. Advanced glycation end products: sparking the development of diabetic vascular injury. *Circulation* **114,** 597–605 (2006).

12. Padilla, J. *et al.* Regular exercise reduces endothelial cortical stiffness in Western diet – fed female mice. *Hypertension* **68,** 1236–1244 (2016).

13. Lesniewski, L. A. *et al.* Aging compounds western diet-associated large artery endothelial dysfunction in mice: prevention by voluntary aerobic exercise. *Exp. Gerontol.* **48,** 1218–1225 (2013).

14. Mitchell, G. F. Arterial stiffness and hypertension: chicken or egg? *Hypertension* **64,** 210–214 (2014).

15. Sacre, J. W., Jennings, G. L. R. & Kingwell, B. A. Exercise and dietary influences on arterial stiffness in cardiometabolic disease. *Hypertension* **63,** 888–893 (2014).

16. World Heart Federation. *Cardiovascular disease risk factors*. (2017).

17. Weisbrod, R. M. *et al.* Arterial stiffening precedes systolic hypertension in diet-induced obesity. *Hypertension* **62,** 1105–1110 (2013).

CHAPTER 8

ADDITIONAL STUDIES

Parts of this chapter are published in PLOS ONE[1] and Biomacromolecules[2] or were presented in conference proceedings as a presentation[3] or a poster.[4]

For Figure 8.1 the podosome images and data were collected by Na Young Kim and were verified in an independent experiment by Julie Kohn. For Figure 8.5B, scanning electron microscopy samples were prepared by Julie Kohn and images were taken by Mingyu He. For Figure 8.7, junction width analysis was performed by Adeline Chen. For Figure 8.8, images were taken by Marsha Lampi.

8.1 Vascular smooth muscle cell matrix-degradation by podosomes

8.1.1 Introduction

Podosomes are dynamic actin-rich cellular structures capable of adhering to and degrading extracellular matrix (ECM).[5–7] As such, podosomes are largely found in invasive cell types, including macrophages, osteoclasts, and dendritic cells.[8,9] Podosomes are also found in vascular smooth muscle cells (VSMCs) and are thought to mediate VSMC migration[5,10–12] and may contribute to intimal hyperplasia in response to vascular injury or atherosclerosis. More recently, VSMCs have been shown to form podosomes when induced by phorbol esters[10] or growth factors.[11] Although the release of growth factors due to inflammation or other pathological

conditions has been regarded a critical factor inducing podosome formation,[11] very little is known about the physical cues in the vascular microenvironment that induce and mediate podosome formation.

During intimal hyperplasia, VSMCs convert from a contractile, quiescent phenotype to a synthetic, invasive phenotype and migrate from the media to the intima.[13] Many physiological factors are implicated in the initiation of VSMC migration, such as growth factor stimulation,[13,14] topography,[15,16] pressure,[17] and injury.[18] However, podosome formation in VSMCs are typically studied solely in response to phorbol esters or growth factors, which do not completely mimic the conditions within the native or diseased microenvironment. Since VSMCs are capable of sensing and responding to force and physical cues, we hypothesized that VSMC podosomes may be induced by these same stimuli. Using engineered platforms to recreate aspects of the microenvironment of the blood vessel, we show that static pressure and injury can trigger podosome formation. We also show that wound healing is impaired by inhibition of the Src pathway. Although our data is specific to VSMCs, these novel mechanisms of podosome formation could be applicable to other invasive cell types.

8.1.2 Materials and Methods

Cell culture: A7R5 rat aortic smooth muscle cells (ATCC, Manassas, VA) were maintained in DMEM (Invitrogen, Carlsbad, CA) supplemented with 10% fetal bovine serum (Invitrogen) and 100 units/ ml of penicillin/streptomycin (Invitrogen) at 37°C in a 5% CO_2 incubator. A7R5 were chosen as

they have been widely used in the literature and closely recapitulate podosomes found in humans.[12,19,20]

Pressure assay: A custom-built aluminum pressure chamber, as used previously,[21] was placed in a 37°C incubator. The oxygen level was controlled at an ambient level of 21% for both the pressure chamber and the incubator. A gas tank (95% air, 5% CO_2, Airgas, Salem, NH) was used for the experiment to induce pressure in the chamber. Cells seeded in 6-well plates were placed inside the chamber and pressurized to 100, 150, or 200 mmHg for 30 minutes. Cells were fixed and stained for cortactin, actin, and nuclei. For pSrc studies, cells were stained for actin and pSrc f (Tyr416) (Cell Signaling, Danvers, MA). Cells were imaged using a Zeiss LSM700 inverted laser scanning confocal microscope (Carl Zeiss, Oberkochen, Germany).

Immunofluorescent staining: Cells were fixed with 3.7% formaldehyde in PBS and permeabilized with 1% Triton-X. Cells were then immunostained with rabbit polyclonal cortactin primary antibody (H-191, Santa Cruz Biotechnology, Santa Cruz, CA) and Alexa Fluor 594 goat anti-rabbit secondary antibody (Invitrogen). F-actin was stained with Alexa Fluor 488 conjugated phalloidin (Invitrogen), and nuclei were stained with 40,6-diamidino-2-phenylindole (DAPI) (Sigma-Aldrich). Images were taken on a LSM 700 confocal microscope (Zeiss, Germany). The presence of podosomes was determined by co-localization (yellow) of F-actin (green) with cortactin (red), a common marker of podosomes.[12]

Wound healing assay: A7r5 cells were wounded by dragging a sterile 200 µl pipette tip across confluent monolayers to create cell-free zones. Fresh media was applied, and the cells were observed and imaged on a fluorescence microscope for the next two days, where images were taken every 6 hours. To inhibit the Src family, cells were incubated in 10 µM 4-amino-5-(4-methylphenyl)-7-(t-butyl)pyrazolo-d-3,4-pyrimidine (PP1) (Sigma-Aldrich, St. Louis, MO) diluted in DMSO for 30 min before wounding,[22,23] and control cells were treated with DMSO alone.

Statistical analysis: All experiments were performed at least in duplicate and data are reported as mean ± standard deviation (SD). All data were tested for normality using the Shapiro-Wilk goodness-of-fit test on JMP software. To compare two groups of data, statistical significance was determined by Student's t-test for normal data and with the Wilcoxon rank sum test for non-normal data. For multiple comparison tests where residual distributions failed normality tests, the Kruskal-Wallis one-way analysis of variance with Dunn's multiple comparison test was used to determine statistical significance. Both GraphPad Prism (v. 5.0) and JMP Pro (v. 11) software were used and p-values < 0.05 were considered statistically significant. Error bars are reported as standard deviation (SD).

8.1.3 Results

Podosome formation is induced by increased static pressure

We sought to investigate whether physical cues within the diseased vascular microenvironment known to induce migration, such as increased pressure, also induce podosomes in VSMCs. Evidence indicates hypertensive pressures can alter VSMC actin polymerization,[24] and because

of the key role of actin in podosome structure,[6,9,25] we examined the effect of elevated static pressure on podosome formation. Cells were stimulated with 200 mmHg of pressure, which mimics physiological, stage II hypertension pressure.[26] Non-pressurized cells served as a control. Notably, high pressure mimicking that found in hypertensive patients, induces podosome formation in VSMCs (Figure 8.1).

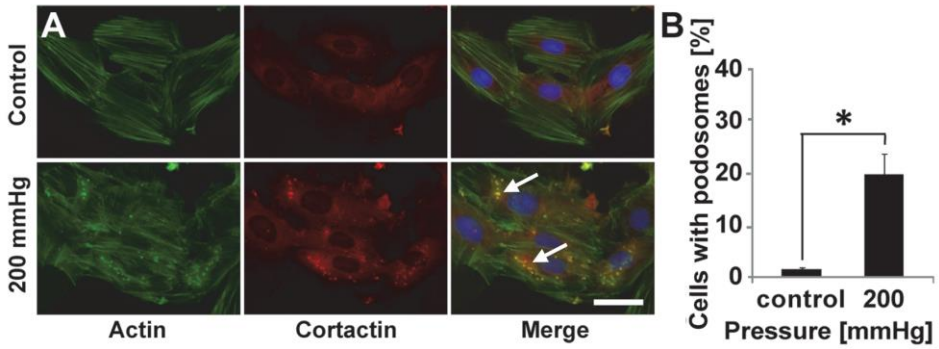

Figure 8.1: Podosomes are formed with a pressure stimulus. (A) Podosomes can be visualized as the co-localization of actin and cortactin (arrows indicate podosomes), and (B) a higher number are present after pressurization of 200 mmHg. Error bars are SD and * $p < 0.05$ (Kruskal-Wallis one-way analysis of variance with Dunn's multiple comparison test). The images and data shown here were collected by Na Young Kim and were verified in an independent experiment by Julie Kohn.

Podosome formation in response to physical cues is mediated by Src kinase

To corroborate the mechanism by which physical cues stimulate podosome formation, we further focused on the Src pathway. Src has been shown to activate cdc42, a Rho family GTPase required for podosome assembly.[27] As such, we investigated Src signaling as a possible

mechanism through which physical cues activate podosome formation. To inhibit Src, PP1, a selective and potent Src-family tyrosine kinase inhibitor was used.[28] Treatment with PP1 correlates with impaired wound healing (Figure 8.2).

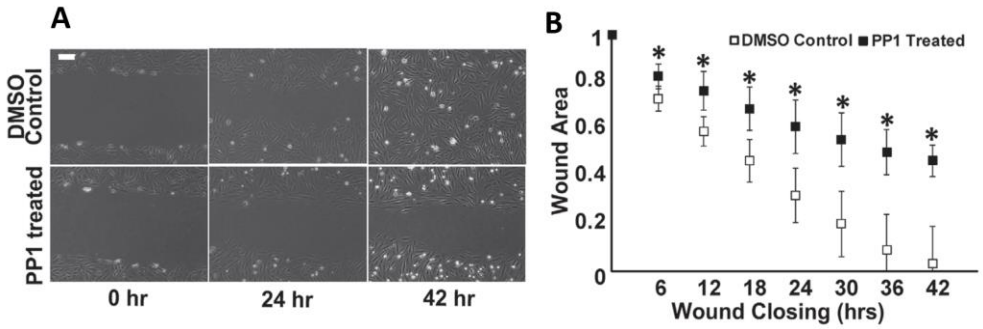

Figure 8.2: Podosome formation induced by wounding is dependent on Src activity. (A) VSMCs with/without PP1 treatment at 0, 24, 42 hours after wounding. Scale bar, 100 µm. (B) Wound closure rate comparison between VSMCs with/without PP1 treatment. Data are mean ± SD. Data were normalized to 0 hour values, *$p < 0.05$ (Wilcoxon rank sum test, n = 15).

8.1.4 Discussion

While numerous studies have investigated podosome formation and function, most have induced their formation using phorbol esters such as PDBu as agonists.[10] Preliminary studies demonstrate that PDBu can form podosomes in VSMCs on glass (Figure 8.3A). VSMCs transfected with Life-Act actin (mCherry) can be imaged in real-time using fluorescence microscopy, which shows that podosomes can be present for at least 30 minutes after PDBu induction (Figure 8.3B).

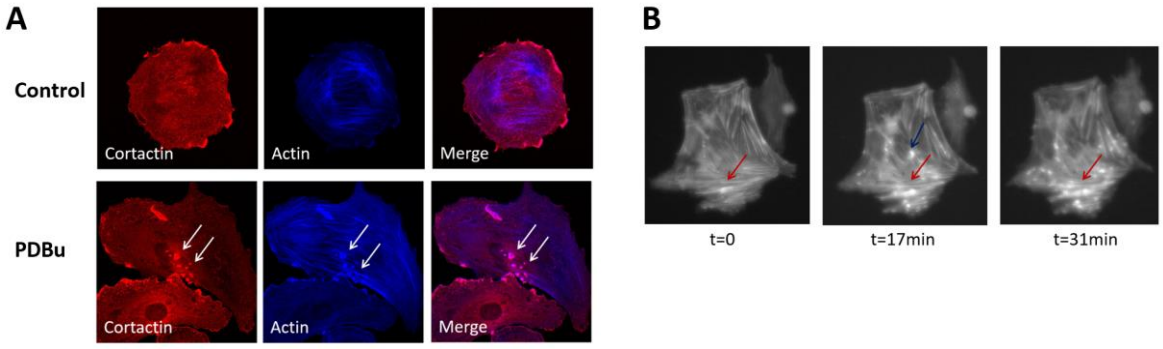

Figure 8.3: Podosomes can be formed from PDBu treatment in (A) VSMCs on glass, imaged by the co-localization of cortactin and actin (arrows). (B) Podosomes activated by PDBu can be imaged in real-time and are present after treatment for at least 30 minutes.

However, physiological, physical inducers of podosomes have generally been overlooked. Hypertensive pressure often occurs with atherosclerosis and is known to have deleterious effects on endothelial and vascular smooth muscle cell function.[29] Since previous studies show pulsatile[30,31] and static pressures[17] increase VSMC migration, we investigated pressure as a potential stimulator of VSMC podosome formation. Applied pressure of 200 mmHg, which mimics pressures found in stage II hypertension, significantly increased podosome formation compared to no pressure (Figure 8.1). These results are complementary to recent findings by Aga *et al*. (2008), who determined that trabecular meshwork cells may respond to increased intraocular pressure by forming podosomes capable of releasing MMPs and degrading their surrounding ECM.[32] Based on these findings, it is possible that VSMCs experiencing hypertensive pressures assemble podosomes to aid in their migration, contributing to disease progression. Future studies should investigate podosome formation *in vivo* in a hypertensive model.

Src is known to stimulate podosome formation as well as be involved in podosome disassembly in a variety of cells and systems.[6] Src is a component in a miRNA143/145 pathway that regulates podosome formation.[11] Here, we show that inhibition of the Src-family through PP1 decreases the ability to heal a wound in a monolayer of VSMCs (Figure 8.2). These data indicate the importance of Src in the response of cells to wounding. Other data from this paper (not shown here) indicate that Src regulates the formation of podosomes in response to the physical cues. These other data demonstrate that podosome formation in response to topography, wounding and hypertension studies was inhibited by a Src inhibitor or dominant negative cdc42. These data suggest that topography, wounding, and increased pressure upregulate Src and cdc42 activity, increasing podosome formation.

Vascular injury, like that which occurs during angioplasty or vein graft implantation,[13] also induces VSMC migration *in vivo*. Podosomes have been shown to actively degrade matrix *in vitro* and are hypothesized to aid in VSMC migration across tissue boundaries.[5] Recently, Quintavalle et al. (2010) observed podosome formation *ex vivo* in aortas of miRNA-143 (145) knockout mice,[11] further implicating podosomes as possible contributors to VSMC migration. Together with these studies, our results point to a potentially important role for podosomes in VSMC invasion during diseases such as atherosclerosis or vascular injury. In preliminary data, podosomes formed through pressure treatment were demonstrated to degrade their matrix (Figure 8.4). Here, the co-localization of cortactin and actin indicating podosome presence after pressure treatment is also the same location of matrix degradation. Fluorescent Oregon-Green gelatin was degraded by podosomes, as imaged with an LSM confocal microscope.

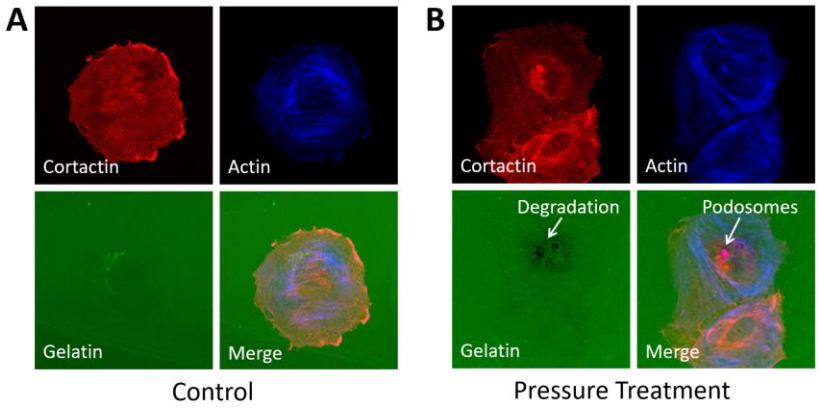

Figure 8.4: Pressure-induced podosomes actively degrade their matrix, shown in (A) a control cell with no pressure treatment that does not exhibit podosomes, and (B) cells undergoing pressure treatment that exhibit podosomes as well as gelatin degradation at the same locations.

Podosomes have been shown to form in a number of cell types including osteoclasts, macrophages, endothelial cells, and dendritic cells.[8,9,33] It remains unclear if the same physical cues identified here will also trigger podosomes in other cell types, which is of future interest. Additionally, it would be of significant interest to recapitulate these results *in vivo* or in human primary cells. Moreover, there are many parallels between podosomes and invadopodia, actin-based cellular structures present in cancer cells that are thought to enable metastasis by releasing MMPs to facilitate invasion.[34] Podosomes and invadopodia contain many of the same intracellular proteins and have matrix degrading ability, however podosomes are typically more transient, forming and receding in a matter of minutes, where invadopodia persist for longer periods.[35,36] It has been suggested that podosomes may be precurors to invadopodia.[34] As such, it is of future interest to determine if the same physical cues that trigger podosomes in VSMCs

also trigger invadopodia in cancer cells, since many of these same cues exist in the tumor microenvironment.

8.1.5 Conclusions

Our study identifies pressure as a novel, physiologically-relevant stimulator of podosome formation and Src inhibition as an inhibitor itself to wound healing. Preliminary data suggests that active podosomes degrade their matrix, and that pressure can induce active podosomes. Since podosomes form in many other cells types, it is possible that these same factors which influence podosomes here may also influence podosomes in a number of pathologies.

8.2 Endothelial cell viability on a new biomaterial (PEUU)

8.2.1 Introduction

Doxorubicin (DOX) is a highly-implemented chemotherapy drug,[37] although it is currently delivered in the body with significant leakage, non-specific distribution, and cytotoxicity side effects.[38,39] In this study, an Arg-Leu PEUU biomaterial was synthesized to deliver DOX as an anti-cancer therapeutic. Natural amino acids, such as arginine (Arg), are biocompatible, and can be used to create polymers to deliver drug nanoparticles to different sites around the body.[40–42] Cationic drug carrying particles are used due to their ability to bind to cell membranes and cause cellular uptake.[43–45] The family of Arg-PEUU materials is especially mechanically strong and has the ability to photo-crosslink,[46] making it a family of interest for these applications. Finally, Arg plays a role in macrophage activation,[47] which is important in wound healing and cancer inhibition.[48] Thereby, by using these polymers as drug delivery nanoparticles, the hypothesis is

that not only would drug-delivery of DOX take place, but there would be an augmenting effect due to the inflammatory activation of macrophages. Here, a neutral, hydrophobic amino acid, leucine (Leu), was added to the polymer to allow for self-assembled and stable nanoparticles, as it has been shown to do in other polymers.[49,50] One test for biocompatibility of this new polymer family used bovine aortic endothelial cells (BAECs). The normal BAEC cobblestone morphology and the presence attachment sites to the material demonstrates biocompatibility.

8.2.2 Materials and Methods

Adhesion Assay of Bovine Aortic Endothelial Cells (BAECs) on an Arg-Leu PEUU Substrate: First, 150 µL of 1 mg/mL 6-Arg-4-Leu-4 A/L-2/1 (Arg-Leu) PEUU solution in DMF was coated twice on circular glass coverslips (11 mm diameter), dried at room temperature in a fume hood, and sterilized by 30 min of UV radiation (265 nm). BAECs were seeded onto Arg-Leu PEUU coated glass coverslips as well as uncoated glass controls at 163 cells/mm^2. BAECs were cultured with M199 media supplemented with serum fetal clone III, penicillin−streptomycin, MEM amino acids, and vitamins. After 3 days in culture, the samples were fixed with 3.7% formaldehyde and prepared for scanning electron microscopy by dehydration in increasing concentrations of 50%, 70%, 90%, and 100% ethanol solution before freeze-drying. The samples were spin-coated with carbon and images were taken using an scanning electron microscopy (Tescan Mira 3). For fluorescence imaging, samples were fixed, permeabilized using 1% Triton and PBS/0.02% Tween washes, and blocked with PBS/0.02% Tween/3% bovine serum albumin. Primary vinculin antibody (1:100) and secondary antibody (1:200, Alexa Flour 488) were both incubated overnight. Actin was stained with phalloidin (1:100, Alexa Flour 568) for 1 h, and the nucleus was

stained with DAPI (1:100) for 10 min. Images were acquired on a laser scanning confocal microscope (Carl Zeiss LSM 700, Germany) using a 40x water-immersion objective.

8.2.3 Results and Discussion

BAECs were seeded onto both glass coverslips and Arg-Leu PEUU coated coverslips for 3 days, and cellular attachment was analyzed using fluorescence for actin and vinculin, and morphology by scanning electron microscopy imaging (Figure 8.5). Cell-matrix attachments on the Arg-Leu PEUU are clearly evident in the actin/vinculin merged image (Figure 8.5A) and cells on the Arg-Leu PEUU biomaterial exhibit a cobblestone morphology similar to those on the glass substrates (Figure 8.5B). These image data indicate that the Arg-Leu PEUU biomaterial allows for endothelial cell viability and adhesion.

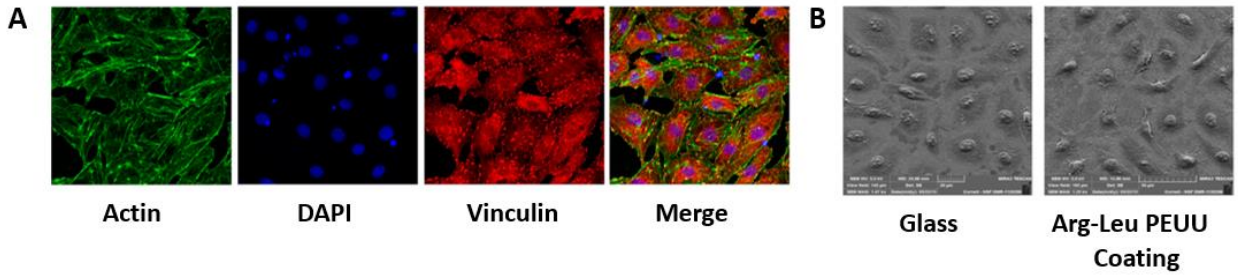

Figure 8.5: BAECs are adhered onto the Arg-Leu PEUU biomaterial after culture for 3 days. (A) Fluorescent images of BAECs adhered onto the Arg-Leu PEUU coated layer, stained for actin (green), DAPI (blue), and vinculin (red). (B) Scanning electron microscopy images, left: cells on cover glass; right: cells on glass coated with the Arg-Leu PEUU material. Scanning electron microscopy samples were prepared by Julie Kohn and images were taken by Mingyu He.

8.2.4 Conclusions

Here, we found that endothelial cells are viable on and adhere to the Arg-Leu PEUU biomaterial. This result is promising for practical application of this material. By altering the combinations of the building blocks, this polymer was tuned to be a drug delivery vehicle for anti-cancer therapies, which relies on biocompatibility. Successful viability with BAECs, as well as the cobblestone morphology and the attachment sites indicates that research into this material for drug delivery use should be continued.

8.3 Gender does not influence endothelial junction stability in an ex vivo artery model

8.3.1 Introduction

Atherosclerosis, the buildup of plaque in arteries, is the number one cause of death in the Western World and leads to stroke and heart attack.[51] Uptake of cholesterol into the artery initiates plaque development.[51] The inner layer of the artery is the intima, and is lined with endothelial cells (ECs), and the tight junctions between ECs modulate cholesterol uptake into the artery.[51] It is now known that increased junction width allows higher permeability of cholesterol, and aging itself is known to increase junction width and permeability of cholesterol.[52] However, the majority of cardiovascular studies only use male samples and it is unknown if endothelial cell-cell junction width changes based on sex. Due to the lack of female cardiovascular studies, we wish to determine if sex effects the junction widths between endothelial cells as a measure of cardiovascular health.

8.3.2 Materials and Methods

Murine aorta acquisition: Male and female C57Bl/6 mice were culled at 6 months of age by formaldehyde perfusion through left ventricle. The hearts and aortas were excised and fixed in paraformaldehyde and rinsed in phosphate buffered saline. Thoracic aortas were removed and cut longitudinally, allowing for staining and imaging of the intima layer.

Imaging EC junction width: fluorescent staining was performed using vascular endothelial cadherin (VE-cadherin) to stain the EC membrane and DAPI for the nucleus. The aorta samples were then imaged using a laser scanning confocal microscope (Figure 8.6) and ImageJ software was used to draw a line perpendicular to EC junctions at widest section. Intensity profiles were collected of VE-cadherin intensity along the line. The VE-cadherin intensity profiles were fit to one or two Gaussian curves using customized MATLAB code as shown previously,[52] and the junction width was measured as 20% above baseline intensity (Figure 8.6). Student's t-test were used to measure statistical significance with $p < 0.05$ as significant.

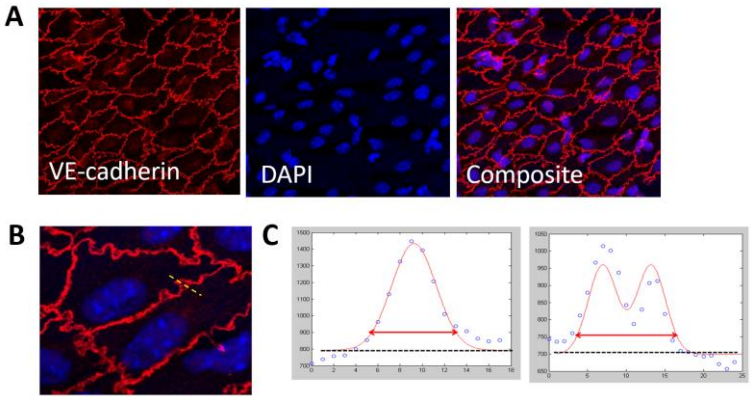

Figure 8.6: Measurement of endothelial cell-cell junction width. (A) Mouse aorta stained for the VE-cadherin membrane protein and the nucleus (DAPI). Junction width analysis using Image J software, (B) line is drawn perpendicular to the cell-cell junction, (C) MATLAB code fits the data as one or two peaks of intensity and measures junction width as 20% above baseline. Blue circles represent data and red line represents Gaussian fit.

Statistical analysis: The two groups were compared using Student's t-test where significance was determined at $p < 0.05$, and reported using box and whisker plots.

8.3.3 Results

The length of the junctions between two endothelial cells in the intima layer of *ex vivo* murine arteries was measured through fluorescence analysis. In this study, no significant difference was found between the endothelial cell-cell junction widths in the male and female mice (Figure 8.7).

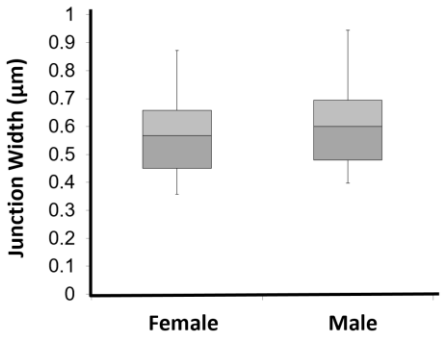

Figure 8.7: Gender does not have a significant effect on endothelial cell-cell junction width in C57Bl/6 mice. Data shown in box and whisker plots with n = 124 female and n = 119 male junction width measurements, using 3 mice for each group. A Student's t-test with a $p > 0.05$ demonstrated no statistical difference between the groups. Junction width analysis was performed by Adeline Chen.

8.3.4 Discussion

In future studies, a more complex analysis of the endothelial cell-cell junctions may be necessary to fully understand the three-dimensional architecture of the junctions. Other metrics for junctional integrity were tested. For example, scanning electron microscopy can be used to visualize this layer and measure the junction separations, as we have carried out *in vitro* with bovine ECs on glass (Figure 8.8). Endothelial cell body overlaps may cause increased junctional stability, and this imaging process could lead to a more accurate representation of these characteristics in *ex vivo* tissue.

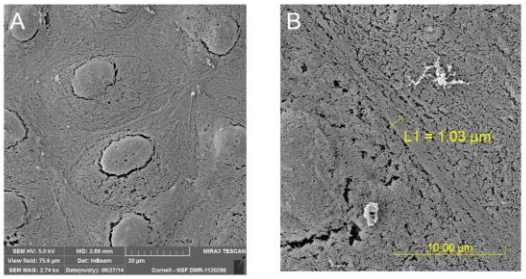

Figure 8.8: Scanning electron microscopy image of bovine aortic endothelial cells plated on glass coverslips. (A) Junctions between cells can be visualized and assist in further analysis of junction stability, and (B) junctions using this *in vitro* method demonstrate junctions from 0.8 – 1.5 µm long. Images were taken by Marsha Lampi.

Another approach to understanding junctional integrity is through Evan's Blue dye analysis, as shown previously. In this assay, the Evan's Blue dye is injected retro-orbitally into the vascular system of the mouse and allowed to circulate throughout the body. Then after a set time, the mouse is sacrificed and the amount of dye in the aorta is measured through images taken on a color camera (Figure 8.9). This assay can provide an *in vivo* assessment of endothelial cell-cell junctional integrity because higher permeability is known to be caused by leakier junctions. The scanning electron microscopy and Evan's Blue techniques could provide useful assessment of junctional integrity to help measure differences between males and females.

Figure 8.9: Evan's Blue dye assay allows for colormetric determination of endothelial cell-cell junctional integrity *in vivo*. A control aorta without dye (left) and an aorta with dye injection (right) are shown.

8.3.5 Conclusions

Male junction width measurements can be an important indicator of vascular health,[52] and in this study of 6 month C57Bl/6 mice, we did not find a significant difference with the junction widths measured in female mice. Male junction width measurements can be analyzed for other cardiovascular risk factors in the future, such as high fat, high sugar diet and a lack of exercise. We also showed that scanning electron microscopy may be used to visualize *ex vivo* artery junction widths. Using these data, we can identify novel pathways to intervene therapeutically, targeting EC junction stability.

8.4 Mouse aortic endothelial cells do not change size or packing density after aging *in vivo*

8.4.1 Introduction

Aged ECs exhibit an altered phenotype, and are more prone to apoptosis, and senescence.[53,54] Previous experiments studying aged ECs use cells cultured on tissue culture plastic for many passage cycles.[55] There is a strong interplay between EC age, phenotype and EC dysfunction.

Whereas aged ECs with shear stress stimulation do not upregulate NO production, when the aged cells are transfected with constitutively active eNOS, shear stress was shown to mitigate apoptosis.[55] Interestingly, eNOS and nitric oxide production have been shown to decrease in ECs aged by increased passage number.[55] However, these cells have remained in culture on stiff tissue culture plastic, which is orders of magnitude more stiff than *in vivo* vasculature. Therefore, the effects of aging ECs taken from a live animal on characteristics such as cell morphology has not been studied. Here, we seek to understand the importance of EC aging through culture of aged ECs on glass coverslips or on gels of physiological stiffness.

8.4.2 Materials and Methods

MAEC extraction onto PA gels: Male C57Bl/6 mice were sacrificed at 2-5 months or 18-24 months for the young and aged groups, respectively. Thoracic aortas were removed and cleaned on ice. Mouse aortic ECs (MAECs) were cultured by direct explant of thoracic aortic tissue onto PA gels of physiologically relevant stiffness or onto glass coverslips. The PA gels were synthesized and coated with collagen, as previously shown,[56,57] and modified from Wang and Pelham (1998).[58] PA gels from 2 to 25 kPa are commonly used to test the effects of stiffness on EC phenotype.[52,59] Explants were placed with the endothelium downwards onto the gel with a glass coverslip on top to flatten the curved aorta, and ECs migrated off of the tissue and onto the matrix over 48 hours based on preliminary experiments. Cells were supplemented with fresh media and cultured for two days as shown in Figure 8.10.

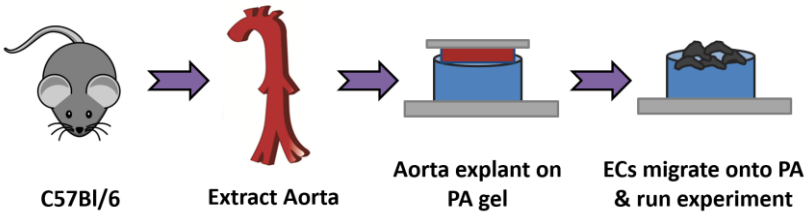

Figure 8.10: MAECs are extracted from the murine aorta which is explanted onto glass or a PA gel, and then allowed to culture directly on the gel.

Collagenase extraction of MAECs: For some experiments, MAECs were extracted by digestion of the artery in collagenase solution. The solution was spun in a centrifuge, and the cell pellet was resuspended in media, and seeded onto the applicable dish. See Appendix G for full methods for MAEC extraction, using three different methods.

Endothelial cell staining: Extraction of cells from the aorta produces heterogeneous cell populations. MAECs were differentiated from vascular smooth muscle cells by staining from DiI (DiI AcLDL, or acetylated low density lipoprotein, Thermo Fischer), which is an endothelial cell-specific marker through the mechanism of acetylated low density lipoprotein uptake in endothelial cells.[60] Fluorescence microscopy was used to image groups of cells and those stained with DiI were known to be ECs. The proof of concept for this method, shown in Figure 8.11 below, demonstrates no DiI fluorescence for A7r5 (rat vascular smooth muscle) cells and positive staining for BAECs (bovine aortic endothelial cells).

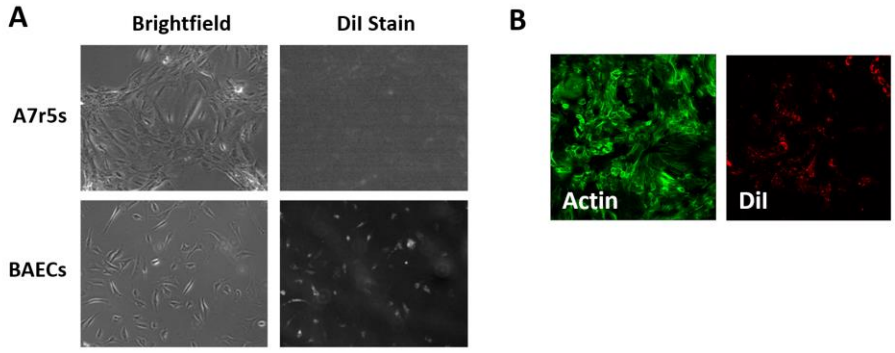

Figure 8.11: Heterogeneous cell populations were acquired from aortic explantation and DiI staining is used as a positive marker for ECs. (A) DiI stains BAECs (endothelial cells), but not A7r5 (smooth muscle cells). (B) Endothelial cells can be differentiated in a heterogeneous cell population with fluorescence of the DiI marker.

Traction force microscopy: Explanted cells were seeded onto polyacrylamide gels with fluorescent beads and traction force microscopy was performed as previously shown.[61] Briefly, cells were allowed to adhere to the gels for at least a day before they were placed in the traction chamber. Images were taken on a Zeiss Axio Observer.Z1m fluorescent microscope before and after trypsin, which was used to remove the cells. The magnitudes of the traction forces were measured using the LIBTRC analysis library from M. Dembo and Y-L. Wang.[62] ECs were identified on the gels based on their small size in comparison to the vascular smooth muscle cells.

Statistical analysis: Data was analyzed using Graphpad Prism 7 software. Student's t-tests were used to compare two groups with $p < 0.05$ for significance.

8.4.3 Results and Discussion

MAECs were extracted from young and aged mice to assess the direct effect of aging on characteristics such as cell area and clustering. ECs tended to form tight clusters of small cells, which were also identified using DiI staining (Figure 8.12A). Traction forces exerted by MAECs on PA gels ranged from 10-700 Pa (Figure 8.12B), where the highest tractions are at the exterior of the cell, and where the force range is consistent with EC traction forces from previous experiments.[52] Clusters of MAECs on glass extracted from young and aged mice, were compared and no difference was detected in single cell area (Figure 8.12C). The total size of MAEC clusters was plotted against the number of cells in each cluster, and no statistical differences were found between the density of clusters for young and aged MAECs.

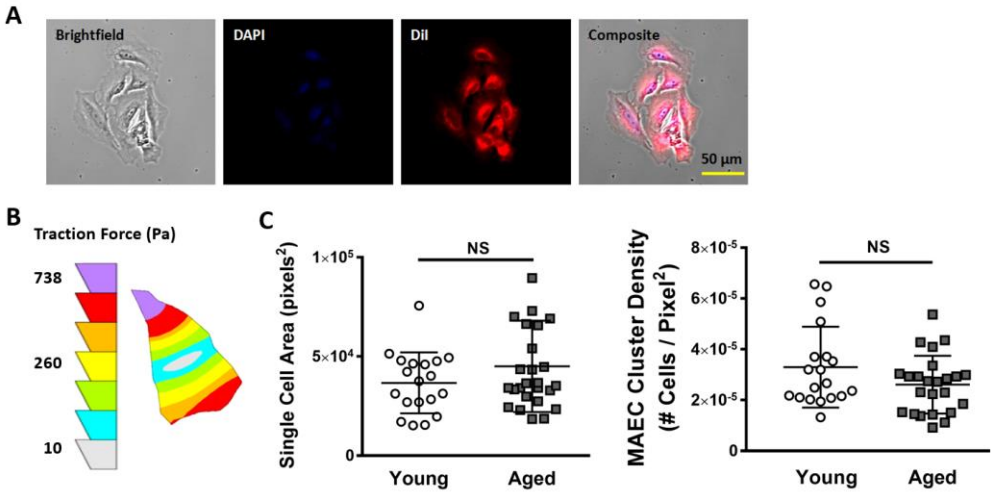

Figure 8.12: MAECs from young and aged mice. (A) DiI stain was used to identify MAECs *ex vivo* from both young and aged mice, scale bar is 50 µm. (B) Traction force microscopy of a representative MAEC demonstrates a traction force range of 10 to 730 Pa. MAECs on glass demonstrate no effect due to cellular aging in (C) single MAEC area, or (D) the packing density of

MAECs in clusters, n = 19 or 26 clusters analyzed per group, NS = not statistically significant (Student's t-test).

Here, we demonstrate that MAECs can be extracted from young and aged vessels, but present no differences in cell area or packing density. MAEC extraction purity was a challenge in the experimental setup, and a dissociation machine was used in later experiments. Due to propensity for ECs to stick to each other, it was also rare to find individual cells to analyze for assays such as traction force microscopy, and instead EC clusters were analyzed. Future experiments should be completed to determine the effect of age on MAEC traction forces and overall response to aging. It remains unknown whether MAECs respond to matrix stiffness differently after the cells have aged *in vivo*.

8.4.4 Conclusions

Mouse aortic endothelial cells were explanted from young and aged mice and were identified based on their small size and uptake of DiI stain. MAECs demonstrated traction forces in the range of other ECs, but were most often grouped in tight clusters. Analysis of MAEC clusters found that there was no effect in cell size or packing density due to age. Future studies to analyze the impact of aging on MAEC response to matrix stiffness should be performed.

8.5 Changes in micro-scale stiffness of the aortic arch and thoracic aorta due to age

8.5.1 Introduction

Ageing is known to increase the pule wave velocity (PWV) in humans[63] and murine models[64]. The most clinically relevant PWV is taken from the carotid to femoral vessels, and PWV measurements can change along vascular tree.[65] The aorta is a complex tissue, with different longitudinal segments: the aortic arch at the outflow from the heart, and the thoracic and abdominal aorta sections along the descending aorta. Reginal variations in aortic stiffness can be measured by non-invasive PWV.[66] In certain mammals, the aortic arch is equal in stiffness or may even be less stiff than the thoracic aorta.[67] In humans, atherosclerotic plaques primarily occur in the descending aorta and the aortic arch, and less so in the ascending aorta.[68] While macro-scale stiffness has been measured in different aorta segments,[66] the micro-scale subendothelial matrix stiffness is unknown in the aortic arch. Here, we measure micro-scale stiffness changes due to age in both the thoracic aorta and the aortic arch.

8.5.2 Materials and Methods

Animal study: Aortas were taken from C57Bl/6 mice used in a previous study.[64] Briefly, in this study young (2 months) or aged (18 months) mice were used to compare the effect of aging on subendothelial matrix stiffness. A subset of aged mice also underwent an exercise regimen of 8-weeks of forced swimming. All animal treatment was carried out under an approved Cornell University Institutional Animal Care and Use Committee protocol. At time of sacrifice, mice were anesthetized and the heart and aorta were removed and kept on ice.

Tissue preparation and indentations: For aortic arch measurements, the aortic arch was separated from the thoracic aorta, cut longitudinally, and two side incisions were made so the tissue could lay flat. Endothelial cells were scraped off the tissue, which has been shown to not affect the subendothelial matrix.[69] ECs were scraped off and the tissue was attached to a petri dish as stated above. Aorta sections were glued to a dry petri dish (Loctite Super Glue), and a bubble of phosphate buffered saline was placed on top. Contact mode atomic force microscopy (AFM) (Asylum MFP-3D) was used to indent the subendothelial matrix in random locations using a cantilever calibrated at 0.12 N/m with a 5 μm sphere radius polystyrene bead (Novascan Technologies). Following thoracic aorta mapping[64], indentations were made in the thoracic aorta at random locations on the tissue. Indentations were also made in random locations throughout the aortic arch tissue. The force versus indentation curves were fit to the Hertz model to determine elastic modulus values.[52,64,70]

Data analysis: Aortic arch indentations were taken in random locations throughout the tissue segment and the elastic moduli were compared to measurements from random locations on the thoracic aorta. Student's t-test was used to determine significance, with $p < 0.05$ as significant. Error bars are reported in standard error of the mean (SEM).

8.5.3 Results and Discussion

Thoracic aorta and aortic arch sections were taken from young mice, as well as aged mice with and without exercise treatment from a previous study.[64] The aortic arch was cut into an 'H' shape so that it could be glued flat the petri dish (Figure 8.13A). Indentations were taken with AFM in

random locations within each tissue section to record the subendothelial matrix of the tissue (Figure 8.13B). With increased age, the moduli of the thoracic aorta demonstrated a significant increase, while no change was found in the aortic arch.

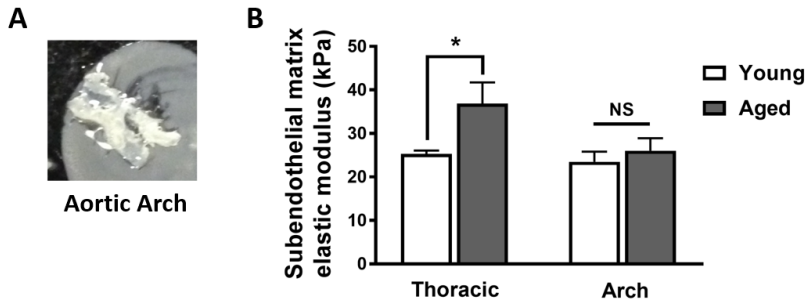

Figure 8.13: Age increases thoracic aorta subendothelial matrix stiffness, but not aortic arch stiffness. Random aorta indentations were made after laying the thoracic aorta and (A) aortic arch flat on a petri dish. (B) The subendothelial matrix elastic moduli are compared between the thoracic aorta and aortic arch locations in young, aged sedentary and aged exercised mice. * $p < 0.05$ (Student's t-test), NS = not statistically significant, error bars are SEM, n = 3 – 4 mice per group.

We found that the aortic arch subendothelial matrix stiffness did not increase with age while the thoracic aorta stiffness did increase with age. In humans, aortic PWV increases more in the abdominal and thoracic aorta from ageing than in the aortic arch; while the thoracic aorta increases by 0.7 m/s per decade lived, the aortic arch only increases 0.4 m/s per decade.[66] Therefore, our data agree with the larger increase in the thoracic aorta due to ageing than in the aortic arch. Another possible cause of our result may be due to the method used to measure the subendothelial elastic modulus. When cutting the aortic arch to lay flat on the dish, more

incisions in the tissue were made, releasing more hoop stresses than were required to indent the thoracic aorta.

8.5.4 Conclusions

Here, we measured the elastic moduli of the subendothelial matrix at both the thoracic aorta and aortic arch from young and aged mice. While micro-scale stiffness increased in the thoracic aorta, there was no increase found in the aortic arch due to ageing. These data match the trend demonstrated by increased PWV measured in humans due to ageing.

8.6 Changes in elastin and collagen content in the intima layer with age

8.6.1 Introduction

While the subendothelial matrix is known to increase in stiffness with age,[52] causes for this stiffening remain unknown. Collagen, a major component of the intima extracellular matrix (ECM),[71] is known to affect arterial stiffness on the macro-scale.[72–74] Another important ECM protein, elastin, is the key component in the internal elastic lamina, an area of the vascular wall near the intima which is known to degrade with age.[75–77] Here, we qualitatively examine elastin and collagen *en face* in the artery intima to assess changing ECM content and structure in young and aged arteries.

8.6.2 Materials and Methods

Aorta preparation: C57Bl/6 mice aortas were removed from young and aged mice, as detailed in Appendix D. Briefly, mice were anesthetized using isoflurane, and the thoracic aortas were

removed from the thoracic cavities. The tissues were cleaned under a dissection microscope, rinsed in phosphate buffered saline (PBS), and placed between two pieces of cover-glass. PBS was added between the glass to maintain moisture in the tissue.

Multi-photon Microscopy: Multi-photon microscopy was used to image elastin and collagen in the intima layer of *ex vivo* murine tissue. The samples were placed lumen side down, and images were taken at multiple z-depths within the range of the intima layer (up to 4 μm into the tissue). Auto-fluorescence was used to detect elastin and collagen was imaged using second harmonic generation. Young and aged arteries were qualitatively assessed for noticeable changes in elastin and/or collagen content and structure.

8.6.3 Results and Discussion

Multi-photon microscopy can be used to image elastin in the internal elastic lamina, as well as nearby collagen in the intima (Figure 8.14). In this study, young and aged murine aortas were imaged using multi-photon microscopy to qualitatively assess intima collagen and elastin content. Images were taken *en face* to assess structural changes in this thin layer. However, in this study, no qualitative differences were observed between young and aged samples. Although no differences were detected between the young and aged samples using this imaging technique, more samples should be tested and quantitative analysis should be performed.

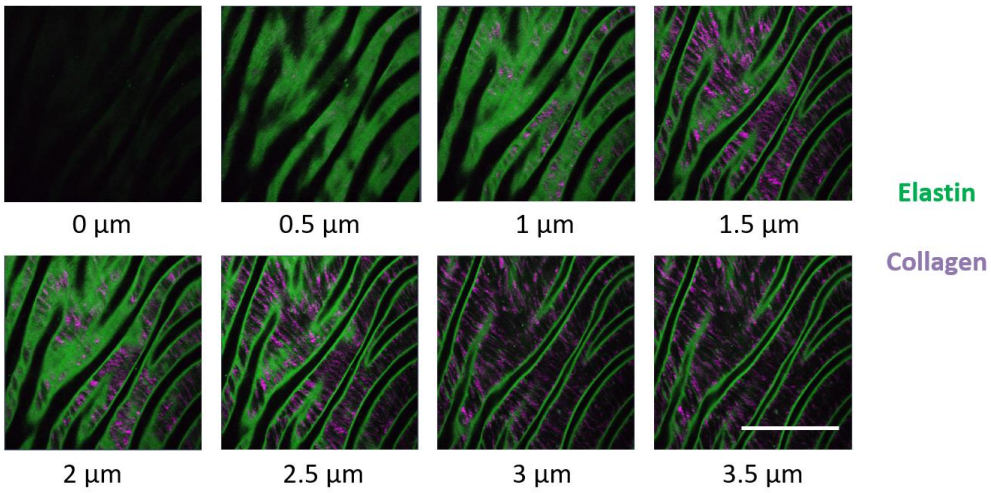

Figure 8.14: A multi-photon microscope was used to capture images of elastin by auto-fluorescence and collagen by second harmonic generation. *En face* murine aorta tissue section imaged, with z-slices ranging from 0 to 3.5 µm deep into the intima. Scale bar is 100 µm.

8.6.4 Conclusions

As collagen and elastin are thought to alter artery stiffness, the content and structure of these proteins in *ex vivo* intima tissue was assessed. No differences were qualitatively determined between young and aged arteries. However, this imaging technique was straightforward to perform, and warrants further examination with more samples and quantitative analysis.

8.7 References

1. Kim, N. Y. *et al.* Biophysical induction of vascular smooth muscle cell podosomes. *PLoS One* **10,** e0119008 (2015).
2. He, M. *et al.* Self-assembled cationic biodegradable nanoparticles from pH-responsive amino-acid-based poly(ester urea urethane)s and their application as a drug delivery vehicle.

Biomacromolecules **17,** 523–537 (2016).

3. Kohn, J. C., Bordeleau, F. & Reinhart-King, C. A. Vascular smooth muscle cell matrix-degradation by podosomes. in *39th Annual Northeast Bioengineering Conference* 5–6 (2013). doi:10.1109/nebec.2013.151
4. Kohn, J. C., Chen, A., Lampi, M. & Reinhart-King, C. Gender does not influence endothelial junction stability in an ex vivo artery model. in *World Congress of Biomechanics* Poster Presentation (2014).
5. Burgstaller, G. & Gimona, M. Podosome-mediated matrix resorption and cell motility in vascular smooth muscle cells. *Am. J. Physiol. Hear. Crculatory Physiol.* **288,** H3001–H3005 (2005).
6. Murphy, D. A. & Courtneidge, S. A. The 'ins' and 'outs' of podosomes and invadopodia: characteristics, formation and function. *Nat. Rev. Mol. Cell Biol.* **12,** 413–426 (2011).
7. Linder, S. The matrix corroded: podosomes and invadopodia in extracellular matrix degradation. *Trends Cell Biol.* **17,** 107–117 (2007).
8. Linder, S., Nelson, D., Weiss, M. & Aepfelbacher, M. Wiskott-Aldrich syndrome protein regulates podosomes in primary human macrophages. *Proc. Natl. Acad. Sci. U. S. A.* **96,** 9648–9653 (1999).
9. Buccione, R., Orth, J. D. & McNiven, M. A. Foot and mouth: podosomes, invadopodia and circular dorsal ruffles. *Nat. Rev. Mol. Cell Biol.* **5,** 647–657 (2004).
10. Hai, C.-M., Hahne, P., Harrington, E. O. & Gimona, M. Conventional protein Kinase C mediates phorbol-dibutyrate-induced cytoskeletal remodeling in A7r5 smooth muscle cells. *Exp. Cell Res.* **280,** 64–74 (2002).

11. Quintavalle, M., Elia, L., Condorelli, G. & Courtneidge, S. A. MicroRNA control of podosome formation in vascular smooth muscle cells in vivo and in vitro. *J. Cell Biol.* **189,** 13–22 (2010).
12. Mak, A. S. p53 regulation of podosome formation and cellular invasion in vascular smooth muscle cells. *Cell Adhes. Migr.* **5,** 144–149 (2011).
13. Gerthoffer, W. T. Mechanisms of vascular smooth muscle cell migration. *Circ. Res.* **100,** 607–621 (2007).
14. Abedi, H. & Zachary, I. Signalling mechanisms in the regulation of vascular cell migration. *Cardiovasc. Res.* **30,** 544–556 (1995).
15. Biela, S. A., Su, Y., Spatz, J. P. & Kemkemer, R. Different sensitivity of human endothelial cells, smooth muscle cells and fibroblasts to topography in the nano-micro range. *Acta Biomater.* **5,** 2460–2466 (2009).
16. Yim, E. K. F. *et al.* Nanopattern-induced changes in morphology and motility of smooth muscle cells. *Biomaterials* **26,** 5405–5413 (2005).
17. Onoue, N. *et al.* Increased static pressure promotes migration of vascular smooth muscle cells: involvement of the Rho-kinase pathway. *J. Cardiovasc. Pharmacol.* **51,** 55–61 (2008).
18. McDonald, R. A., Hata, A., MacLean, M. R., Morrell, N. W. & Baker, A. H. MicroRNA and vascular remodelling in acute vascular injury and pulmonary vascular remodelling. *Cardiovasc. Res.* **93,** 594–604 (2012).
19. Wang, J. *et al.* Phosphorylation of G protein-coupled receptor kinase 2-interacting protein 1 tyrosine 392 is required for phospholipase C-γ activation and podosome formation in vascular smooth muscle cells. *Arterioscler. Thromb. Vasc. Biol.* **30,** 1976–1982 (2010).
20. Gu, Z., Fonseca, V. & Hai, C.-M. Nicotinic acetylcholine receptor mediates nicotine-induced

actin cytoskeletal remodeling and extracellular matrix degradation by vascular smooth muscle cells. *Vascul. Pharmacol.* **58,** 87–97 (2013).

21. Vouyouka, A. G., Jiang, Y., Rastogi, R. & Basson, M. D. Ambient pressure upregulates nitric oxide synthase in a phosphorylated-extracellular regulated kinase- and protein kinase C-dependent manner. *J. Vasc. Surg.* **44,** 1076–1084 (2006).
22. Hanke, J. H. *et al.* Discovery of a novel, potent, and Src family-selective tyrosine kinase inhibitor. *J. Biol. Chem.* **271,** 695–701 (1996).
23. Schmitz, U., Thömmes, K., Beier, I. & Vetter, H. Lysophosphatidic acid stimulates p21-activated kinase in vascular smooth muscle cells. *Biochem. Biophys. Res. Commun.* **291,** 687–691 (2002).
24. Cipolla, M. J., Gokina, N. I. & Osol, G. Pressure-induced actin polymerization in vascular smooth muscle as a mechanism underlying myogenic behavior. *FASEB J.* **16,** 72–6 (2002).
25. Kaverina, I., Stradal, T. E. B. & Gimona, M. Podosome formation in cultured A7r5 vascular smooth muscle cells requires Arp2/3-dependent de-novo actin polymerization at discrete microdomains. *J. Cell Sci.* **116,** 4915–4924 (2003).
26. Chobanian, A. V *et al.* Seventh report of the Joint National Committee on Prevention, Detection, Evaluation, and Treatment of High Blood Pressure. *Hypertension* **42,** 1206–1252 (2003).
27. Tatin, F., Varon, C., Génot, E. & Moreau, V. A signalling cascade involving PKC, Src and Cdc42 regulates podosome assembly in cultured endothelial cells in response to phorbol ester. *J. Cell Sci.* **119,** 769–781 (2006).
28. Bain, J., McLauchlan, H., Elliott, M. & Cohen, P. The specificities of protein kinase inhibitors:

an update. *Biochem. J.* **371,** 199–204 (2003).

29. Hollander, W. Role of hypertension in atherosclerosis and cardiovascular disease. *Am. J. Cardiol.* **38,** 786–800 (1976).
30. Cullen, J. P. *et al.* Ethanol inhibits pulse pressure-induced vascular smooth muscle cell migration by differentially modulating plasminogen activator inhibitor type 1, matrix metalloproteinase-2 and -9. *Thromb. Haemost.* **94,** 639–645 (2005).
31. Redmond, E. *et al.* Effect of pulse pressure on vascular smooth muscle cell migration: the role of urokinase and matrix metalloproteinase. *Thromb. Haemost.* **81,** 293–300 (1999).
32. Aga, M., Bradley, J. M., Keller, K. E., Kelley, M. J. & Acott, T. S. Specialized podosome- or invadopodia-like structures (PILS) for focal trabecular meshwork extracellular matrix turnover. *Investig. Opthalmology Vis. Sci.* **49,** 5353–5365 (2008).
33. Prasad, A. *et al.* Slit2N/Robo1 inhibit HIV-gp120-induced migration and podosome formation in immature dendritic cells by sequestering LSP1 and WASp. *PLoS One* **7,** e48854 (2012).
34. Yamaguchi, H., Wyckoff, J. & Condeelis, J. Cell migration in tumors. *Curr. Opin. Cell Biol.* **17,** 559–564 (2005).
35. Balzer, E. M. *et al.* c-Src differentially regulates the functions of microtentacles and invadopodia. *Oncogene* **29,** 6402–6408 (2010).
36. Baldassarre, M. *et al.* Dynamin participates in focal extracellular matrix degradation by invasive cells. *Mol. Biol. Cell* **14,** 1074–1084 (2003).
37. Zacchigna, M., Cateni, F., Drioli, S. & Bonora, G. M. Multimeric, multifunctional derivatives of poly(ethylene glycol). *Polymers (Basel).* **3,** 1076–1090 (2011).
38. Skitzki, J. J. & Chang, A. E. Hepatic artery chemotherapy for colorectal liver metastases:

technical considerations and review of clinical trials. *Surg. Oncol.* **11,** 123–135 (2002).

39. Medina, S. H. *et al.* Enzyme-activated nanoconjugates for tunable release of doxorubicin in hepatic cancer cells. *Biomaterials* **34,** 4655–4666 (2013).
40. Wu, J., Wu, D., Mutschler, M. A. & Chu, C.-C. Cationic hybrid hydrogels from amino-acid-based poly(ester amide): Fabrication, characterization, and biological properties. *Adv. Funct. Mater.* **22,** 3815–3823 (2012).
41. Wu, J., Yamanouchi, D., Liu, B. & Chu, C.-C. Biodegradable arginine-based poly(ether ester amide)s as a non-viral DNA delivery vector and their structure–function study. *J. Mater. Chem.* **22,** 18983–18991 (2012).
42. Song, H. & Chu, C. C. Synthesis and characterization of a new family of cationic amino acid-based poly(ester amide)s and their biological properties. *J. Appl. Polym. Sci.* **124,** 3840–3853 (2012).
43. Liu, J. *et al.* Endocytic uptake of a large array of HPMA copolymers: Elucidation into the dependence on the physicochemical characteristics. *J. Control. Release* **143,** 71–79 (2010).
44. Varkouhi, A. K., Scholte, M., Storm, G. & Haisma, H. J. Endosomal escape pathways for delivery of biologicals. *J. Control. Release* **151,** 220–228 (2011).
45. He, M. & Chu, C. C. Dual stimuli responsive glycidyl methacrylate chitosan-quaternary ammonium hybrid hydrogel and its bovine serum albumin release. *J. Appl. Polym. Sci.* **130,** 3736–3745 (2013).
46. He, M. & Chu, C.-C. A new family of functional biodegradable arginine-based polyester urea urethanes: synthesis, chracterization and biodegradation. *Polymer (Guildf).* **54,** 4112–4125 (2013).

47. He, M., Potuck, A., Zhang, Y. & Chu, C.-C. Arginine-based polyester amide/polysaccharide hydrogels and their biological response. *Acta Biomater.* **10,** 2482–2494 (2014).

48. Mills, C. D. *et al.* Macrophage arginine metabolism and the inhibition or stimulation of cancer. *J. Immunol.* **142,** 2709–2714 (1992).

49. Bag, D. S., Dutta, D., Shami, T. C. & Bhasker Rao, K. U. Synthesis and characterization of L-leucine containing chiral vinyl monomer and its polymer, poly(2-(methacryloyloxyamino)-4-methyl pentanoic acid). *J. Polym. Sci. Part A Polym. Chem.* **47,** 2228–2242 (2009).

50. Bauri, K., Pant, S., Roy, S. G. & De, P. Dual pH and temperature responsive helical copolymer libraries with pendant chiral leucine moieties. *Polym. Chem.* **4,** 4052–4060 (2013).

51. Lusis, A. Atherosclerosis. *Nature* **407,** 233–241 (2000).

52. Huynh, J. *et al.* Age-related intimal stiffening enhances endothelial permeability and leukocyte transmigration. *Sci. Transl. Med.* **3,** 112ra122 (2011).

53. Donato, A. J., Morgan, R. G., Walker, A. E. & Lesniewski, L. A. Cellular and molecular biology of aging endothelial cells. *J. Mol. Cell. Cardiol.* 122–135 (2015). doi:10.1016/j.yjmcc.2015.01.021

54. Asai, K. *et al.* Peripheral vascular endothelial dysfunction and apoptosis in old monkeys. *Arterioscler. Thromb. Vasc. Biol.* **20,** 1493–1499 (2000).

55. Hoffmann, J. *et al.* Aging enhances the sensitivity of endothelial cells toward apoptotic stimuli: important role of nitric oxide. *Circ. Res.* **89,** 709–715 (2001).

56. Charest, J. M., Califano, J. P., Carey, S. P. & Reinhart-King, C. A. Fabrication of substrates with defined mechanical properties and topographical features for the study of cell migration. *Macromol. Biosci.* **12,** 12–20 (2012).

57. Califano, J. P. & Reinhart-King, C. A. A balance of substrate mechanics and matrix chemistry regulates endothelial cell network assembly. *Cell. Mol. Bioeng.* **1,** 122–132 (2008).

58. Wang, Y. L. & Pelham, R. J. J. Preparation of a flexible, porous polyacrylamide substrate for mechanical studies of cultured cells. *Methods in Enzymology* **298,** 489–496 (1998).

59. Klein, E. A. *et al.* Cell-cycle control by physiological matrix elasticity and in vivo tissue stiffening. *Curr. Biol.* **19,** 1511–1518 (2009).

60. Netland, P., Zetter, B., Via, D. & Voyta, J. In situ labelling of vascular endothelium with fluorescent acetylated low density lipoprotein. *Histochem. J.* **17,** 1309–1320 (1985).

61. Lampi, M. C. *et al.* Simvastatin ameliorates matrix stiffness-mediated endothelial monolayer disruption. *PLoS One* **11,** e0147033 (2016).

62. Dembo, M. & Wang, Y.-L. Stresses at the cell-to-substrate interface during locomotion of fibroblasts. *Biophys. J.* **76,** 2307–2316 (1999).

63. Hallock, P. Arterial elasticity in man in relation to age as evaluated by the pulse wave velocity method. *Arch. Intern. Med.* **54,** 770 (1934).

64. Kohn, J. C. *et al.* Mechanical heterogeneities in the subendothelial matrix develop with age and decrease with exercise. *J. Biomech.* **49,** 1447–1453 (2016).

65. Laurent, S. *et al.* Expert consensus document on arterial stiffness: methodological issues and clinical applications. *Eur. Heart J.* **27,** 2588–2605 (2006).

66. Hickson, S. S. *et al.* The relationship of age with regional aortic stiffness and diameter. *JACC Cardiovasc. Imaging* **3,** 1247–1255 (2010).

67. Shadwick, R. & Gosline, J. Arterial Windkessels in marine mammals. *Symp. Soc. Exp. Biol.* **49,** 243–252 (1995).

68. Meissner, I. *et al.* Atherosclerosis of the aorta: Risk factor, risk marker, or innocent bystander? *J. Am. Coll. Cardiol.* **44,** 1018–1024 (2004).

69. Peloquin, J., Huynh, J., Williams, R. M. & Reinhart-King, C. A. Indentation measurements of the subendothelial matrix in bovine carotid arteries. *J. Biomech.* **44,** 815–821 (2011).

70. Hertz, H. Tiber die beriihrung fester elastischer korper (On the contact of elastic solids). *J. für die reine und Angew. Math.* **95,** 156–171 (1881).

71. Murata, K., Motayama, T. & Kotake, C. Collagen types in various layers of the human aorta and their changes with the atherosclerotic process. *Atherosclerosis* **60,** 251–262 (1986).

72. Shadwick, R. E. Mechanical design in arteries. *J. Exp. Biol.* **202,** 3305–3313 (1999).

73. Fleenor, B. S., Marshall, K. D., Durrant, J. R., Lesniewski, L. A. & Seals, D. R. Arterial stiffening with ageing is associated with transforming growth factor-β1-related changes in adventitial collagen: reversal by aerobic exercise. *J. Physiol.* **588,** 3971–3982 (2010).

74. Díez, J. in *Atherosclerosis, Large Arteries and Cardiovascular Risk* (eds. Safar, M. & Frohlich, E.) **44,** 76–95 (2007).

75. Schlatmann, T. J. M. & Becker, A. E. Histologic changes in the normal aging aorta: implications for dissecting aortic aneurysm. *Am. J. Cardiol.* **39,** 13–20 (1977).

76. Keyes, J. T., Haskett, D. G., Utzinger, U., Azhar, M. & Vande Geest, J. P. Adaptation of a planar microbiaxial optomechanical device for the tubular biaxial microstructural and macroscopic characterization of small vascular tissues. *J. Biomech. Eng.* **133,** 75001 (2011).

77. Lee, K., Forudi, F., Saidel, G. M. & Penn, M. S. Alterations in internal elastic lamina permeability as a function of age and anatomical site precede lesion development in apolipoprotein E-null mice. *Circ. Res.* **97,** 450–456 (2005).

APPENDIX A

MEASUREMENT OF NITRIC OXIDE AFTER SHEAR STRESS APPLICATION

These notes should be used in conjunction with the Molecular Probes'

"Nitric Oxide Indicators: DAF-FM and DAF-FM Diacetate" protocol

1. Remove all red dye in the media before running the experiment. Incubate samples for 10 – 15 minutes with PBS in the incubator and change to media without red indicator dye.

2. Following application of shear stress, make sure to move the dishes slowly between locations so as not to induce more shear stress.

3. To detect nitric oxide (NO) changes between static and 3 hours of shear, 10 µM of DAF dye was used on each sample.

4. Static controls should be used to compare to the sheared samples. Make sure to leave the static samples in the bacterial incubator with C-15 media with dextran for the same period as the sheared samples. This will account for changes in CO_2, temperature, movement and media that are also applied to the sheared samples.

5. It is important to spread the dye out over the gel evenly. I used 3 mL/sample on a 60 mm coverslip.

6. Imaging should take place on the Zeiss laser scanning confocal microscope and the user should be careful to keep all imaging parameters the same for each acquisition. The following laser settings were used to detect effects due to 3 hours of shear stress:

    a. Laser 488 power = 7.0, Pinhole = 4.11 AU, Section thickness = 40.2 µm

b. Green gain = 700, TPMT gain = 400

7. Data can be normalized by experiment to a common condition in each experiment. In my study, the trends were the same in all experiments, but sometimes entire experiment values were higher or lower as a whole. Therefore, batch variation can be accounted for through normalization.

8. For specific procedure details used for the Biophysical Journal publication, and how to normalize the DAF data, see Julie's Lab Notebook #3, on pages 86 and 90.

APPENDIX B

MOUSE SWIMMING EXERCISE REGIMEN

This protocol was originally written by Stephanie Cheng.

Location: Weill Hall B80

Swimming Site Equipment:

- Swimming tub
- Heating pad
- Beakers (1 large, 1 small)
- Thermometer
- Paper towels
- Towel
- Heat lamp

*NOTE- do not swim mice after another stressful event, such as jaw bleeding or ultrasound.

Swimming Site Set-up:

1. Fill tub with warm water until the marked limit using the large beaker.
2. Turn on hot plate and set the temperature to 35 ^{o}C. Continue to monitor the water temperature throughout the exercise period and keep within IACUC guidelines.
3. **Weighing Mice (Location: Weill Hall B79C):** select the necessary mouse group(s) and take weight measurements with the mouse container and scale.

4. Place the mice in the water. The first three days are for acclimation swimming, in which the mice are swum for 3 minutes to acclimate them to the aquatic environment.
5. In the following weeks, 5 days a week the mice are swam, always in the same swim groups to avoid stress. The mice are swum for 10 minutes daily during the first week, followed by two weeks of 30 minute swims. They are then swum for 45 minutes until cull after 8 weeks of the exercise regimen.
6. If a mouse appears to be consistently floating instead of actively swimming, gently nudge the mouse's tail with the thermometer, or induce a gentle current with the thermometer.
7. If the mouse continues to float or appears to be struggling with swimming, separate the mouse and let it swim in a large beaker alone. If the mouse is still struggling, remove the mouse from swimming for that session. Mice that cannot swim normally with their heat group more than three times should be removed from the study.
8. Any aggressive mouse that tries to push other mice under the water should be removed and swum on his own. If he cannot swim with the swimming group for more than three times, he should be removed from the study.
9. After the swimming session, dry the mice with paper towels/towel. If necessary, use the heat lamp to keep the mice warm if they display signs of being cold.
10. Place mice back in their respective cages on the rack.
11. Monitor the mice for the next 10 minutes, especially those that underwent the swimming regimen to make sure they do not appear hunched or immobile.

APPENDIX C

MOUSE ULTRASOUND MEASUREMENTS OF PULSE WAVE VELOCITY AND LEFT VENTRICULAR EJECTION FRACTION

Location: Ultrasound Room (Weill Hall, Basement)

Ultrasound Site Equipment:

- Nair
- Tape
- Gauze
- Q-tips
- Electrogel
- Ultrasound gel
- Surgical marker
- Ruler
- Paper towel
- T-spray
- Kimwipes

Ultrasound Site Set-up:

Shaving the mice: The **day before the ultrasound measurements**, the mice have to be shaved of their fur for the readings to be taken. This allows the mice to be more calm and have a regular heart beat on the day you do ultrasound.

1. Cover the mouse chamber bottom with a paper towel and place the mouse in the mouse chamber. Make sure the line with the red tape (connects the isoflurane gas to the chamber) is open.
2. Turn on the oxygen and set the isoflurane level to 3.
3. Set the heating pad temperature to 37 ^{o}C.
4. When the mouse is breathing about one beat per second, open the line with the pink take and close the line with the red tape.
5. Transfer the mouse in the prone position to the stage, placing the nose in the stage isoflurane tube line. Set the isoflurane level to about 1-1.5, changing as needed.
6. Tape the limbs.
7. Squirt some Nair onto a paper towel and using a Q-tip, spread onto the top half of the back of the mouse, including the back of the head. Rub the head and back thoroughly with the Q-tip.
8. Use the gauze to remove the fur.
9. Turn the mouse onto its back in the supine position.
10. Apply Nair to the abdominal area and rub thoroughly with the Q-tip. For ejection fraction readings, remove hair from the central and upper left chest. As the fur here is less coarse and the area is smaller, less time is needed for the Nair to have an effect.

11. After both sides are shaved, place the mouse back into its cage. Ensure that the mouse is awake and not in distress. Use a heating pad if the mouse appears to be cold.
12. Clean the stage and chamber with T-spray and Kimwipes.
13. Place the Nair, gauze, and Q-tips back into the drawers.

Pulse wave velocity measurements (thoracic to abdominal):

14. The following day, repeat steps 1-4.
15. Apply the electrogel to the four metal pads on the stage.
16. Place the mouse in the prone position on the stage. Place the paws on top of the electrogel, and tape them down.
17. Turn on the ultrasound machine.
18. Place ultrasound gel on the shaved back of the mouse.
19. Use the MS-550D transducer to find the thoracic aorta. Move the transducer and stage positions as needed to get a clear visual.
20. Once the aorta is in view on B mode at a significant angle, place the pulse Doppler cursor around the artery so that the dotted line is within the artery and yellow. Adjust any signal/noise ratio and scaling needed and click 'capture' image.
21. Mark the middle of the transducer position with a surgical marker on the mouse's skin.
22. Measure the length of the distance between the end of the tail and the marked position.
23. After taking all the necessary thoracic measurements, place the mouse in the chamber and let it wake. Keep a heating source nearby in case of shallow breathing.

24. Induce sleep again, and place the mouse in the prone position, with its paws on top of the electrogel. Tape down the paws.
25. Repeat steps 19-22 for the abdominal aorta.
26. Subtract the abdominal distance from the thoracic distance to get the length of the aorta.
27. Transit time is measured as the quotient of the arrival times at each location. Arrival times are specified as the time measured from the peak of the R-wave on the ECG to the upstroke of the velocity profile. Avoid taking measurements around breaths.
28. Divide the distance by time to calculate pulse wave velocity.
29. Wipe down the stage and mouse chamber with T-spray and Kimwipes.
30. Place the mice cages back on the racks in the mouse room.

Pulse wave velocity measurements (abdominal only): The above procedure is used, except for steps 18-26. Instead, use the following.

18. The mouse will be placed so that full access is available to the abdomen. The mouse should have its head tilted back at a large angle. Place electrode gel on the imaging site.
19. Find the cross-section of the aorta near the renal vein to use as an anatomical landmark and keep the transducer measuring within 1 cm of this area. Turn the transducer to then image the aorta longitudinally.
20. Use the MS-550D transducer to find a long section (about 6-10 mm) of the abdominal aorta. Move the transducer and stage positions as needed to get a clear visual.

21. Once the aorta is in view on B, place the pulse Doppler cursor around the artery so that the dotted line is within the artery and yellow. Adjust any signal/noise ratio and scaling needed and click 'capture' image. Mark the location with tape on the screen.
22. Move to the other side of the artery and repeat step 20.
23. Measure the length of the distance along the abdominal aorta by using the Vevo software.
24. After taking all the necessary measurements, place the mouse in the chamber and let it wake. Keep a heating source nearby in case of shallow breathing.
25. Continue the above procedure at step 27.

Left ventricular ejection fraction: Often measured immediately following a pulse wave velocity reading. Follow steps 1 – 28 above and then use the following.

29. Place the transducer flat and the mouse at a significant angle down on the left and sweep across the mouse's upper chest. When a full image of the left ventricle is found, take an EKV high resolution image. Make sure no gasping, shallow breathing is occurring and monitor the mouse heart rate, especially in aged or high-fat, high-sugar diet mice.
30. To analyze the image, use the built-in ejection fraction measurement software on the Vevo system by outlining the long-axis view of the left ventricle at the largest and smallest volumes.
31. Wipe down the stage and mouse chamber with T-spray and Kimwipes.
32. Place the mice cages back on the racks in the mouse room.

APPENDIX D

MOUSE SURGERY FOR AORTA EXTRACTION AND THORACIC AORTA CLEANING

This protocol was originally written by Adeline Chen.

Location: Schaffer Lab (Weill Hall, basement)

Prior to Surgery:

- Prepare perfusion liquid (such as phosphate buffred saline (PBS), paraformaldehyde (PFA), or PBS+Mg^{2+}+Ca^{2+}) in a conical tube.
- Prepare yellow lid jars filled 1/2 full with PBS (or 1x DMEM for MAEC extraction) to store mouse hearts.
- Store all above on ice in a Styrofoam box.

Surgical Site Equipment:

- Cart with isoflurane dispenser and connection to oxygen (Schaffer lab, next to fume hood). Should be reserved at least a day in advance.
- Gas chamber (Tupperware box, Schaffer lab)
- Surgical tools, cleaned previously using the sonocator
- Nose cone (Schaffer lab, “ventilation” drawer)
- Pump for perfusion (Schaffer lab, in fume hood)

- 1 beaker (to hold your tube of PBS for perfusion)
- Operation table: Rack and tub (Schaffer lab, in fume hood)

Surgical Site Set-up:

1. On the cart: make sure the there is isoflurane liquid available in the anesthesia dispenser. (If running out of isoflurane, obtain a bottle of isoflurane from the surgery room to refill dispenser in the hood.)
2. Check that the oxygen tubes are connected correctly (metal ball for oxygen on the side of the cart should be floating). Turn on the oxygen.
3. Perfusion set-up: Place the tube of perfusion liquid in a beaker, unscrew cap. Connect one end of the tubing of the pump to the needle, and test the pump by inserting the other end of the tubing to the tube of perfusion liquid then press "forward" to prime the line until fluid flows out of the needle. Set rate of flow at 5.
4. In the hood: connect isoflurane tube to the gas chamber. Place mouse in the gas chamber and set dial to 3-4% isoflurane to quickly induce anesthetization.
5. When the mouse breathes at 1 Hz, remove the isoflurane tube from the gas chamber and attach it to the nose cone, placed on the operation table.
6. Set the mouse on the rack (chest up and limbs taped) and place the mouse in the nose cone (taped). See Figure D1, panel A.
7. Perfusion and Surgery: Always assure that the mouse is completely anesthetized by performing a toe pinch and monitoring breathing rate.
8. Start the incision at the center of the mouse (high enough to avoid cutting the intestines),

and cut upward toward the head circling around the chest and cutting the ribs to give full abdominal access.

9. Use a hemostat to clip the cut-off area and position the hemostat on the mouse's neck/head.
10. Find the apex of the heart, then make a small incision on the right atrium (looks like a dark tissue section on the upper left of the heart). The heart will start bleeding profusely.
11. Insert the perfusion needle shallowly into the left ventricle. Turn on the perfusion pump (connected to perfusion liquid) and allow the fluid to flow through the heart, through the body and out to the right atrium. *If done correctly, the liver will turn a peach color.
12. Turn off the perfusion pump and remove the needle from the left ventricle.
13. Cut or pull off the organs (lungs and liver) that are blocking the aorta.
14. To extract the aorta, start cutting from above the heart downward along the spine (the trachea is next to the aorta, and the aorta is attached to the spine) and detach the heart/aorta until immediately before the intestines.
15. Put the heart/aorta in the prepared yellow lid jar. If the perfusion liquid is fixation liquid, monitor the time it is fixing and then place in PBS for the remainder of the cleaning and storage process.
16. Turn off the isoflurane. Dispose of the mouse carcass in the appropriate biohazard bin in the fridge.
17. Clean-up: Put used surgical tools in a tin tray and fill it 1/3 with sonication detergent (blue liquid) and then fill the tray to 8/10 full with water. Put the tray into the sonicator, and set the time to 10 min (make sure that the drain is closed and the lid is on).
18. Clean the operating table by pouring the blood/organs into the waste jug (under the sink)

labeled “Perfusion Waste.” Scrub and Rinse the tub and rack in the sink.

19. After the tools have been cleaned, return everything back to its original place. Turn off the oxygen tank and make sure the dial for the isoflurane is set to 0.
20. Bring aorta and surgical tools back to the Reinhart-King lab in a secondary container.

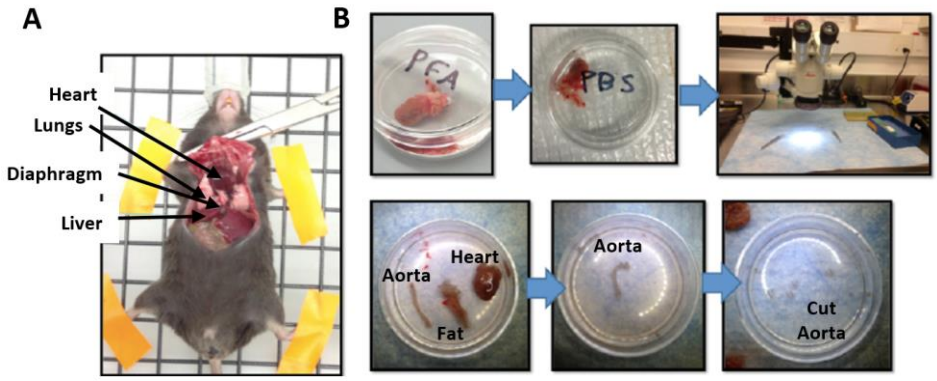

Figure D1: Mouse aorta extraction, from surgery to thoracic aorta cleaning. (A) Mouse is laid supine, with limbs taped down and the chest is held open with the hemostat. (B) After heart and aorta extraction, if tissue will be fixed, it is placed in PFA for a set time, and then rinsed in PBS. Using the dissection microscope, the aorta, fat and heart are all separated, and the aorta is cleaned and cut into the appropriate pieces. This figure was originally created by Adeline Chen.

Location: Reinhart-King lab

21. Extracting the aorta: At the dissection scope in the Reinhart-King lab, prepare a small dish of 1xPBS and transfer the heart into the small dish. Place the dish under the dissection scope and find the aorta (Figure D1, panel B).

22. Pull off fat or organ pieces first to make the aorta more visible. From the top of the heart, you should be able to see the aorta and may also see the trachea (the aorta has an arch that is connected to the top of the heart, and the trachea is a straight tube that is not connected to the heart). Remove any excess fat, organs and trachea.
23. Once the aorta is found, detach it from the heart, remove any remaining fat, making sure not to pinch the tube too much, and transfer it into another clean dish of 1xPBS.
24. The tissue can be flash frozen, stored for histology, or left in clean PBS in a yellow-lid cup at 4 ^{o}C.

APPENDIX E

ATOMIC FORCE MICROSCOPY OF THE ARTERY INTIMA OR GELS FOR ELASTIC MODULUS MEASUREMENT

The AFM is located in Clark Hall, in the CCMR lab, D15 (orange hallway). Card access and training is needed ahead of time. AFM can be booked on Coral and with an account number. Contact the Cornell Center for Materials Research to get trained on the Asylum MFP-3D AFM

NOTE: WILL NEED LOTS OF TRAINING TIME

Purchase Cantilevers:

1. AFM tips are ordered from Novascan. Make sure to ask for the tips to be calibrated before they are sent.
2. Compliant gels (1-20kPa) use tips around 0.06 N/m and arteries (10-60kPa) use tips around 0.12 N/m. However, Novascan says that the acceptable range for a 0.12 N/m purchased cantilever is 0.06-0.24 N/m, but most I receive are around 0.11-0.19 N/m.
3. Sphere radius depends on what size area you want to measure. For gels, I use 500 nm radius and for arteries, 5 μm radius. Make sure to indicate radius or diameter when purchasing.
4. Silicon nitride tips with gold coating reflect the laser the best with this particular AFM. Spheroid tips are normally polystyrene.
5. Allow up to 2/3 weeks to receive tips and store them safely in the bubble wrap. When they come in you may want to check they are calibrated correctly and send back if not.

What to bring to the AFM space:

- Artery in phosphate buffered saline (PBS), on ice, in secondary containment (artery piece must be cut open in a “c” configuration)
- AFM tips, stored safely in holders in bubble wrapping
- Supplies for manipulating arteries: cotton swabs, 60mm petri dishes, room temperature PBS, plastic transfer pipettes
- Two pointy forceps
- Super glue- use Loctite Maximum Bond- it does not decay the artery or dissolve in PBS

Calibrate the AFM- refer to MFP-3D Manuelette, Section 9:

1. Log into Coral using another computer in the room and “enable” the equipment. You should hear a click and the AFM computer screen will turn on.
2. Place cantilever in PEEK cantilever holder, screw only using the green screwdriver.
3. Cover the AFM stage holes with orange tape and place a petri dish lid with a small amount of PBS on the AFM stage.
4. Place PEEK holder into AFM head and flip the head into resting position over the AFM stage, making sure to not bump anything.
5. Move AFM head down so that the legs are all equal height, but the cantilever is not touching the petri dish. Make sure the PEEK holder is submerged in PBS, but not over flowing.
6. Turn on the laser and microscope light.

7. Open Aslyum software, use “Standard”, then “Force” and “Contact Mode” settings. (I do not select liquid mode because it does not have contact mode under this tab.) Let the software open, and press the camera button on bottom.
8. Under the force tab, set the Set Point to -1 V and the Integral Gain to 0.3-0.5 (this value will depend on the noise vibrations in the room, so that the Deflection doesn’t swing around wildly).
9. Set the curve output folder to appropriate location (probably the Desktop). Set Force distance to 1 µm, velocity to 1 µm/s and Start Distance to 2 µm. Press “setup” on all tabs so you can see the full menus.
10. Move the laser (using controls on AFM head) so that its gain is maximal (some people set it at the tip to get more sensitivity, but I find the maximum is good to use in case the laser gets bumped later, this will let you get back to the same spot when you re-adjust). The laser is best visualized by turning down the light and looking on the computer screen for a blue light.
11. Move the photodiode so that the deflection is around 0. Close the AFM doors.
12. Go to the “Thermal” Tab, click “Start thermal capture” and let the tip oscillate until you have two or three well-defined peaks.
13. Chose the applicable peak (generally the first peak for low k around 0.06 N/m, or the second peak for higher k around 0.12 N/m) and place a cursor (ctl+I) at it, center the curve and calibrate the spring constant. This may need to be adjusted a few times to calibrate the k correctly around the manufacturer’s value.

** The spring constant calibration is very important to determining the modulus**

14. Move the photodiode so that the deflection is around -2V. “Engage” the tip using the front wheel on the AFM head and take a curve of tissue culture plastic or glass.
15. Place cursors on non-contact region and set “Vert Defl Line” in Calib subtab of Force tab. This will make the non-contact region horizontal (relatively) in future curves.
16. Indent again and place cursors on contact region. You can increase the Trigger point to around 2.5 V if you need a larger region. Set “Defl Invols” in Calib subtab of Force tab. This will set the Deflection Invols, which should be around 50-110 pN/V.

** The Defl Invols calibration is very important to determining the modulus**

Tissue preparation for aorta indentation:

1. Prepare your working space on the table away from the AFM.
2. Use pointy forceps to remove artery from PBS and place on an empty petri dish with small amount of room temperature PBS.
3. Determine the side of artery with endothelial cells and scrape lightly a few times.
4. Place a small dab of super glue on new, dry petri dish in the center, and remove excess.
5. Place artery on glue and press down with forceps on outside of tissue.
6. Cut small slivers of aluminum foil and glue on either side of artery.
7. Cover tissue and foil with PBS, but not so it overflows onto the AFM head.

AFM the tissue or gel:

1. Place the tissue on the AFM stage, and make sure the stage dials are centered and the cantilever is above the tissue, hovering above the tissue/gel. Remember that when you lower

the head, the cantilever will also shift towards the back of the AFM since you are only lowering the front leg.

2. Find the tissue by locating the shiny aluminum foil and “engage” the tissue. Find the gel by making sure you are within the gel outline and try to be in the center to avoid edge effects (sometimes it is easiest to mark the location with a permanent marker on the bottom of the petri dish for thin gels).

3. Obtain AFM curves! Here are some troubleshooting tips:

- You can adjust the Force Distance, which is how far the entire contact and non-contact curves are (usually about 500 nm for arteries). Do not push too deep (I do not go above 1.5 µm).
- The Start Distance should be around 2 µm and if it’s dragging up towards only a few nm, then your cantilever is attracted to your tissue/gel. Withdraw the tip and try again.
- You can also adjust the trigger point, which is how much the stage will move up when contacting the tissue. I normally have it set by voltage, around 0.2-1 V. For arteries, I find it is best to make light indents, around 0.3 V.
- AFTER ADJUSTING MAKE SURE INDENTATION VELOCITY IS STILL AT 1 µm/s.

*** RECOGNIZING/ACQUIRING GOOD CURVES TAKES A LOT OF PRACTICE***

4. Move to a new location and take another curve. Each marking notch on the AFM stage is 10 µm. The right dial moves the tissue horizontal and the front dial moves vertical.

5. Save your raw curve files and take some print screens with each tab open. Make sure to record the Defl Invols and the Spring Constant because this may change the next time you use the

AFM and you will want to keep relatively consistent. Save the Experiment as well so you can open it later and check your settings.

6. Make sure to clean up all of your workspace. Close the AFM, and ensure no liquids have been spilled on the machine. Turn off the light and the laser, and log off of the AFM.

Analyzing AFM curves:

1. Data can be opened in the offline computer. It is possible to create a New Table of the data and save it in Excel (indentation will be in meters and force will be in Newtons).
2. Click the "Review" button on the Force tab, and Load your curves.
3. Click the "Elastic" tab and input your tip settings. For my subendothelial matrix studies, I used the Hertz model fit with tip radius 5 µm sphere and tissue Poisson ratio of 0.5. I set the tip Poisson to 0.34 and the tip Modulus to 300 GPa based on values for polystyrene, my tip sphere material.
4. Fit the blue dot to the contact point (where curve increases in the contact region) and the red dot to the final analysis location. You can adjust these by right clicking the mouse and zooming in and out of the curve.
5. Select "Fit," a black curve will connect the dots and the Young's Modulus will be highlighted in yellow. Gels are easier to fit because there is less protein breakage.

APPENDIX F

MOUSE FACIAL VEIN BLOOD COLLECTION

Original protocol written by Stephanie Cheng.

Purpose: Mouse facial vein blood can be collected after fasting to assess serum components, such as advanced glycation end product and insulin concentrations.

Location: Weill Hall, Conventional Mouse Facility, Room B79A

Jaw Bleeding Site Equipment:

- 1.7 mL centrifuge tube (two for each mouse)
- 0.65 mL centrifuge tube (one for each mouse)
- 0.5-mm lancet
- Empty mouse cages

Jaw Bleeding Site Set-up:

1. In the mouse room (B79C): Fast the required mice by moving their food to a separate, empty cage for **12 hours the night before the jaw bleeding procedure**. Place the "Researcher Will Feed" cards on the fasting mouse cages and label them with the date and fasting time interval, and initial it.
2. 12 hours later, bring the empty and fasting mouse cages to B79A and set on the metal tabletop. Wet some food pellets and place it in the empty mouse cages so the bled mice can have wet food after the procedure.

3. Put on two sets of gloves. Make sure they are form-fitting.
4. Use the right hand to pick up a mouse by his tail with and place on the cage's metal top.
5. Use the left hand to grab the skin around the neck.
6. Place the tail underneath the ring and little fingers and use the right hand to move the mouse into a position in which the body is stretched straight.
7. Maneuver the left hand scruff until the skin is pulled taut and the head aligned with the body. The head and arms should be immobilized.
8. To find the facial vein, in your head, draw a diagonal line down from the eyes and up from the jawline. The intersection (above and to the left of the freckle) is where the lancet should be placed. Prick the right cheek quickly with the lancet.
9. Turn the mouse on its side to collect the blood with the 1.7 mL centrifuge tube, making sure not to collect too much blood, which is dependent on the size of the mouse.
10. Place the mouse in the empty cage. This ensures that any distress pheromones will not affect the mice which have yet to be bled. Make sure the mouse is warm and has access to wet food.
11. Dispose of the lancet in a sharps container, and use a new lancet on the next mouse. Each mouse should be bled with its own lancet. Dispose of the top layer of gloves if it has mouse blood on it.
12. Repeat steps 4-10 for the second mouse in the cage. When done with all mice in one cage, transfer the food and mice back to the original cage.
13. Repeat the above process for all other cages of mice.
14. Dispose of bloody gloves and paper towels in a biohazard bag.

15. Place the mice cages back on the rack.

Location: Reinhart-King lab

16. **To collect serum**, the blood must be allowed to stand in the centrifuge tubes upright (not on ice) for an hour to allow clotting.
17. Spin the centrifuge tubes in the micro-centrifuge at 10,000 RPM for 10 minutes.
18. Transfer 200 µL of the supernatant (clear liquid portion of the sample) into another 1.7 mL centrifuge tube. Draw up all liquid; small amounts of blood can be drawn up as well.
19. Spin at 10,000 RPM for 5 minutes.
20. Transfer only the clear supernatant serum into a 0.65 mL centrifuge tube. Do not draw up any blood.
21. Label the tubes with necessary information, i.e. cage number, mouse labels, date, time point in the experiment, etc.
22. Place the serum samples in the correct box in the -80^{o}C freezer in a labeled box.

APPENDIX G

MOUSE AORTIC ENDOTHELIAL CELL (MAEC) EXTRACTION

The first two methods in this protocol were originally written by Adeline Chen.

METHOD 1: AORTA EXPLANTS DIRECTLY SEEDED ONTO COLLAGEN GELS

Materials for collagen gels:

- CM 199 media
- NaOH
- Rat Tail Collagen 10 mg/mL stock
- One 15 mL conical tube
- Plastic petri dishes (any size, usually the 35x10 mm dish)

Materials for aorta extraction:

- Surgical tools
- Phosphate buffered saline (PBS) + Mg2+ + Ca2+ solution
- 1x DMEM solution
- Yellow lid jars
- 35x10 mm dishes

Reagents to prepare:

- PBS + Mg2+ + Ca2+ solution:

0.1 g magnesium chloride and 0.1 g calcium chloride in 500 mL 1x PBS

- 1x DMEM:

0.64 g DMEM powder (in fridge) in 50 mL DI water

Making Collagen Gel Beads:

1. Place CM 199 media, NaOH, and rat tail collagen tubes into a bucket of ice.
2. Label a new 15 mL conical tube “collagen gel,” and place it in the ice bucket.
3. In the sterile hood, mix the reagents in the following order and volume:

(Use wide-bore tips for the collagen, mixing, and making gel beads)

a. RT collagen: 150 µL
b. CM 199: 850 µL
c. NaOH: 3 µL

- Makes 1 mL of 1.5 mg/mL collagen gel

4. After thoroughly mixing the collagen gel mixture, use the 200 µL wide bore pipet tips to distribute 20 µL drops of the collagen gel mixture evenly across the plastic petri dishes.
5. Carefully move the collagen gels in the dishes onto a tray, then transfer the dishes into an incubator.
6. The collagen gels should be ready to use by the time the aorta extraction is completed, or within 30 min.

Aorta Extraction:

1. In a box of ice, prepare a 50 mL tube of PBS + Mg2+ + Ca2+ solution for perfusion and a 50 mL tube of 1x DMEM.
2. Prepare labeled yellow lid jars to collect mouse hearts/aortas. Fill the jar 1/4 full with 1x PBS + Mg2+ + Ca2+ solution and 1/4 full with 1x DMEM, then place in the ice box.
3. To extract the heart/aorta from the mice, follow procedures in Appendix D, where the PBS + Mg2+ + Ca2+ solution is used for the perfusion step, setting 5 on the perfusion pump, for about 10 seconds. Avoid any air perfusing through the aorta.
4. Under the dissection scope, clean the aortas in cold 1x DMEM without stretching the aortas. Place cleaned aortas (no excess fat or blood) in a clean petri dish with 1x DMEM on ice.
5. When all the aortas are clean, cut the aortic tube into very small rings.
6. Take out the collagen gels from the incubator (check to see that the gels look solid), and take them to the dissection scope.
7. Have one dish of collagen gels sit next to the aorta rings, and try to keep the lid on the collagen gels as much as possible to avoid contamination and drying out.
8. Cut open on aorta ring, and transfer the opened-up aorta piece onto a gel. Pay attention that the endothelial cell side is facing downward directly on the gel bead.
9. Pat down the tissue piece carefully by lightly flattening the aorta using forceps.
10. When all aorta pieces have been transferred onto gels, stack the dishes and place them in the incubator overnight (16-20 hours).

Removing Aorta Explants:

1. Warm CM 199 media in water bath.

2. After incubating the aorta pieces on collagen gels for 16-20 hours, check the gels.
3. If the gels look dried out, moisten the gels with some CM 199 media in the hood before removing explants. If the gels look the same as the previous day (the ideal case), the explants can be removed without media.
4. Under the dissection scope, carefully remove the aorta explants by grabbing onto one corner of the explant and peeling off the tissue. Place removed tissue pieces on a piece of paper towel (throw in biohazard after finishing).
5. After removing all of the explants, add warm CM199 to the gels (enough to cover the gels, but not too much as to dislodge the gel beads from the dish).
6. Feed the cells with CM 199 every other day until they are ready to use for experiments.

METHOD 2: AORTAS DISSOLVED WITH COLLAGENASE

Materials:

- Surgical tools
- Collagenase Type II (Worthington): 4o Fridge, common shelf
- BSA (bovine serum albumin): 4 o Fridge, in box
- Heparin: chemicals shelf at common bench area
- FBS (fetal bovine serum): -20o Freezer, thaw in 4 o Fridge the night before
- PBS + Mg2+ + Ca2+ (better if sterile)
- PBS (better if sterile)
- Yellow lid jar (for aorta extraction)
- CM 199 media

- Gelatin (for coating dishes)
- 35 mm x 10 mm plastic dishes
- 21G needles and syringes

Reagents to prepare:

- PBS + Mg2++ Ca2+ solution:

0.1 g magnesium chloride and 0.1 g calcium chloride in 500 mL 1xPBS

- 0.1 %BSA/heparin/PBS+ Mg2++ Ca2+ solution:

0.05 g BSA and 100U/mL heparin in 50 mL PBS+ Mg2++ Ca2+

To calculate the amount of heparin to add, check the heparin bottle for active units per gram (i.e. "X" U/g):

(100 U/mL)/("X" U/g) = "Y" g/mL = the amount heparin per mL

"Y" g/mL * 50 mL = total number of grams of heparin to add

- Collagenase/PBS+ Mg2++ Ca2+ solution:

500 U/mL collagenase in 2 mL PBS+ Mg2++ Ca2+

To calculate the amount of collagenase to add, check the bottle for active units per gram (i.e. "X" U/g):

(500 U/mL)/("X" U/g) = "Y" g/mL = the amount collagenase per mL

"Y" g/mL * 2 mL = total number of grams of collagenase to add

Procedure:

1. Make Collagenase/PBS+ Mg2++ Ca2+ solution and store in fridge before surgery.

2. Prepare a box of ice for the aorta extraction.
3. Prepare PBS in a yellow lid jar and 0.1 %BSA/heparin/PBS+ Mg2++ Ca2+ solution in a 50 mL conical tube and place in ice.
4. For the aorta extraction, follow the steps in Appendix D, where you perfuse the heart with 0.1 %BSA/heparin/PBS+ Mg2++ Ca2+ solution at perfusion speed 5. Store aortas in PBS jar on ice. Avoid any air perfusing through the aorta.
5. Under the dissection scope, clean aortas (remove blood clots and fat) without stretching or pinching the tubes.
6. In small plastic dishes, slowly flush ~300 µL of PBS through each aorta using a needle and syringe. To prevent the aortas from detaching when flushing, use forceps to pinch on the needle where it is inserted in the aorta.

*Make sure to remove air bubbles in syringe before flushing the aortas.

7. Slowly flush ~200 µL of collagenase/PBS+ Mg2++ Ca2+ solution through each aorta. Store in incubator for 30 min.
8. Flush aortas with 5 mL PBS+ Mg2++ Ca2+ and collect all flow through in 15 mL conical tubes. Add 10% FBS to flow through to stop digestion and store on ice.
9. Repeat steps 7 – 8 two more times.
10. Spin all collected flow through at 250xg in 4o for 10 min.
11. Coat 35 mm x 10 mm small plastic dishes with gelatin.
12. After centrifuging, aspirate supernatant.
13. Re-suspend cell pellets in 2 mL of CM199 media and plate on gelatin-coated dishes.

METHOD 3: AORTAS DISSOLVED WITH DISSOCIATOR

Materials:

- gentleMACS Dissociator (Miltenyi Biotec)
- gentleMACS C-tubes
- Tumor dissociation kit solutions and DMEM media
- 100 µm MACS SmartStrainers
- Incubator at 37°C, with orbital shaker inside
- Prepared, sterile, PBS + Mg2+ + Ca2+ solution (such as in the previous methods)
- Animal tissue sample containers and petri dishes
- Sterile PBS
- Dissection microscope
- Surgical setup and tools for aorta extraction
- Mice to sacrifice- about 3 to 5 mice per condition at a minimum

Procedure:

1. Keep everything as sterile as possible throughout the process. The night before the procedure the surgery tools should be autoclaved, and all basic solutions (PBS, media) should be kept sterile. Tumor dissociation kit solutions should be aliquoted and stored at -20°C.
2. On the day of the experiment: create tumor dissociation solution by combining media and tumor dissociation kit solutions, in a sterile culture hood, into each gentleMACS C tube. Keep

the solution on ice or in the fridge until use. One C tube per mouse condition should be used so that cells between conditions are kept separate.

a. 2.35 mL of DMEM media
b. 100 µL of Enzyme D
c. 50 µL of Enzyme R
d. 12.5 µl of Enzyme A

3. Extract mouse aorta, as previously described in the previous methods, using sterile PBS + Mg2+ + Ca2+ solution for perfusion. At time of extraction, heart and aorta can be kept in DMEM media on ice.
4. Under the dissection microscope, place the heart and aorta into sterile PBS in a petri dish, and remove the aorta from the heart. Clean the aorta carefully, removing the fat, and making sure not to pinch or stretch the artery as much as possible.
5. Cut up the artery into small pieces, and cut the tubes longitudinally so they are opened, exposing the intima to the outside solution as much as possible.
6. Place pieces carefully in the C tubes with the dissociation solution. Usually about 3-5 full mouse aortas (from mature C57Bl/6 mice) have been used per C tube. When there are fewer aortas per C tube, then the pellet of cells is almost non-existent. Make sure to label the C tubes and only put aortas from the correct mouse condition into each tube.
7. Set the gengleMACS dissociator to “Brain 1” setting. Invert the C tubes, making sure all of the aorta pieces fall to the bottom, and place in the dissociator. Run the “Brain 1” setting once.
8. Place the C tubes in the incubator at 37°C on the orbital shaker for 15 minutes.
9. Place the C tubes on the gentleMACS dissociator, and run the “Brain 2” setting three times.

10. Place the C tubes in the incubator at 37°C on the orbital shaker for 10 minutes.
11. Place the C tubes on the gentleMACS dissociator, and run the “Brain 3” setting three times.
12. Place the C tubes in the incubator at 37°C on the orbital shaker for 30 minutes. If aorta pieces are not dissolved, keep in the incubator for up to 15 minutes longer. Do not leave in more than 45-60 minutes, or else the endothelial cells may start to die. White pieces of fat may not dissolve.
13. During this time, you can set up the hood for the straining, reserve the centrifuge and set it to 4°C, and prepare the dishes to receive your MAEC solutions.
14. Strain the C tube solution (dissociation solution plus dissolved aorta cells) using the 100 µm MACS SmartStrainers in the sterile hood, into separate 15 mL conical tubes, labelled with each mouse condition. Make sure to use one strainer for each separate mouse condition. The strainers should be rinsed first with DMEM, then the C tube solution can run through. Rinse out the C tube and the strainer with extra DMEM to make sure all cells are in the bottom of the 15 mL conical tubes.
15. Spin conical tubes at 4°C at 250g for 10 minutes. There should be a very small, white pellet at the bottom. Given the size of aortas, very large pellets may actually contain bacteria or other contaminants.
16. Remove the supernatant and resuspend the pellet in fresh DMEM. Plate cell solution onto desired dish. Previously, I have found gelatin-coated glass to be the best for endothelial cell viability.
17. Place dishes into the incubator.
18. Change to fresh DMEM media the next day so that leftover dissolved dead debris is removed.

19. Endothelial cells will be very small and replicate slower than the other cell types (mostly vascular smooth muscle cells and fibroblasts). They generally form clusters over time. Do not allow the cell solution to grow for more than a few days, as the other cell types will take over the dish and the endothelial cell clusters will not be present anymore.
20. See ideas in Chapter 8 of this thesis for labeling endothelial cells in a heterogeneous cell population.

Appendix H

INTIMA COLLAGEN MEASUREMENT WITH STRUCTURED ILLUMINATION MICROSCOPY

The structured illumination microscopy section of this protocol was originally written by Joseph Miller and adapted for intima collagen imaging. See this original protocol for instructions on how to setup the optics of the structured illumination microscope.

Purpose: To stain and image murine aortas for intima collagen content quantification.

Materials:

- Mouse aorta (removed as in Appendix D)
- 3.7% formaldehyde fixing solution
- Vascular-endothelial cadherin staining antibodies
- Solutions for general fluorescence microscopy staining
- Picrosirius Red kit (Polysciences, Inc 24901)
- Structured illumination microscope with computer and MATLAB codes
- Glass slides
- Forceps
- Phosphate buffered saline (PBS)

Tissue staining:

1) Immediately after thoracic aorta removal, cut a small tissue section off, open longitudinally, and fix the sample in 3.7 % formaldehyde for 15 minutes. Rinse with PBS three times and store in PBS at 4°C until use.
2) Stain the tissue with vascular-endothelial cadherin (primary 1:100 Santa Cruz, secondary 1:200 AlexaFlour-488) with **overnight incubations** using the standard lab fluorescence staining protocol.
3) At least **two nights before imaging**, stain the samples with the Picrosirius Red kit (Polysciences, Inc 24901) by soaking the tissue in solutions provided by the kit. Instead of the recommended times, use 1 hour with Solution A, 3 hours with Solution B and 1 hour with Solution C.
4) Rinse for a few hours in PBS until the liquid turns pink. Then replace the PBS and leave the samples to soak at 4°C **overnight** (or longer) to remove any excess stain.
5) On the day of imaging, remove the tissue with forceps and carefully place it on a glass slide. Note the luminal side and adjust the tissue so that this side is down towards the glass. Carefully place another glass slide on top, squishing the sample, and making sure not to slide the tissue, which could remove the endothelial cell layer. Allow the remaining space of the glass slides to be filled with PBS.

Taking structured illumination microscopy (SIM) images:

6) Place the 20 lines/mm Ronchi grid in the top slide holder located between the condenser and the light source. Peering through the eyepieces, adjust the condenser until the ruling is in clear focus.
7) Place your sample in the motorized sample holder (moves in z-direction), luminal side down.
8) Adjust the objective/sample/condenser until both the ruling and a plane of the sample are in clear focus. You want to focus on the vascular-endothelial cadherin layer, using fluorescence imaging. This will allow you to image the intima layer.
9) Once this layer is in focus, do not re-adjust the sample height (z-direction). You can still move the sample in the x and y directions to find an area that is as flat as possible and does not have disrupted (peeled or ripped off) endothelial cells.
10) You will now take images of the underlying collagen tissue in the intima layer through three images. Turn off the fluorescence and switch to white light illumination to a set level. Record the while illumination level in order to use this same setting on a different imaging day.
11) Check that the polarizer analyser is placed with its optical axis 90 degrees relative to the illumination polarizer (cross polarizer configuration). Use the micrometer control to adjust the polarizer until total extinction occurs (darkest possible setting).
12) Turn off ambient light in the room so that the only illumination of the sample comes from the white light on the microscope.
13) The Matlab software has been setup to move the Ronchi ruling 2*pi/3 and take the multiple images required. Initiate this on the Matlab software, and wait for the images to be taken.

14) Execute the MATLAB code to reconstruct each of the image sets and then provide you with a stack of images (red, green, and blue channels) of the polarized signal. This image stack represents a snapshot of the collagen content in a thin layer of tissue.

Analysis of images:

15) Measure the intensity values of the three color channels with ImageJ software.

16) Multiply each color value by the grayscale correction factors: 0.2989*red, 0.587*green, and 0.114*blue. Sum these values. This value represents the collagen content in the whole image.

17) Images taken on different days can be normalized to a control artery and can be range corrected if imaging settings are slightly different on each day.

Appendix I

QUANTIFICATION OF THE ADVANCED GLYCATION END PRODUCT N(ε)-CARBOXYMETHYL-LYSINE (CML) IN BLOOD AND AORTA TISSUE

This protocol is intended to be used in conjunction with the N(ε)-carboxymethyl-lysine (CML) ELISA kit (Cell Biolabs STA-816). The flash freezing protocol steps were originally written by Adeline Chen.

Materials:

- Blood or tissue samples for analysis
- N(ε)-carboxymethyl-lysine (CML) ELISA kit (Cell Biolabs STA-816)
- Liquid nitrogen (for tissue sample analysis only)
- BCA protein assay (Pierce, Thermo Scientific) (for tissue sample analysis only)

Blood samples (if not using blood samples, skip to step 5):

1) Collect blood from the mouse facial vein, and remove and store the serum at -80°C, as detailed in Appendix F.
2) Allow blood to thaw naturally immediately before using the N(ε)-carboxymethyl-lysine (CML) ELISA kit (Cell Biolabs STA-816). If samples must be thawed the night before, keep them in 4°C until use the next day.

3) Follow the ELISA kit instructions for CML quantification using the manufacturer's instructions. Save a few wells of the plate for the following verification tests:
    a. Test that the spectrophotometer is reading the buffer as 'zero' by testing buffer with no sample in the machine.
    b. Run a spike test with the CML ELISA. This is where you test for assay interference by adding a known amount of standard to a sample. If the value of this minus the standard value is equal to the sample value, then the assay passes the spike test.
4) Once your assay and spectrophotometer are verified as working properly, quantify the CML concentrations according to the CML ELISA kit manufacturer's instructions and analyze between sample groups.

Tissue samples:

5) Remove mouse aorta, as in Appendix D.
6) Flash freeze the tissue immediately after cleaning off the fat, as detailed below:
    a. Prepare liquid nitrogen (wear insulating gloves!) by scooping liquid nitrogen from the liquid nitrogen tank into a Styrofoam cup held by long forceps. Place Styrofoam cup into the cup holder and cap the cup-holding container to transport liquid nitrogen.
    b. Cut desired section of the cleaned mouse aorta (of length long enough to tell that the sample is a tube) for snap freezing in PBS, without fixing in formaldehyde.
    c. Prepare a labelled 1.7 mL test tube for the tissue sample.

d. After placing the tissue inside the test tube, close the lid and place the tube inside the Styrofoam cup with liquid nitrogen. Allow the tube to sit in liquid nitrogen for about 5 min.

e. After checking that the sample is frozen, transfer the tube using forceps into a box in the -80°C freezer to store. Storage can be for long periods of time.

7) The **night before** the ELISA is run with the samples, grind the arteries using a cold mortar and pestle. Dissolve the arteries in 300 µL of RIPA buffer containing 1:1000 protease inhibitor. Keep samples in 4°C overnight.

8) On the day of the ELISA test, run a BCA protein assay (Pierce, Thermo Scientific) to determine the correlation between protein content and optical density. This will also allow you to know which samples may need to be diluted, for example, for a sample with a larger artery. Save a few wells of the plate for the following verifications:

    a. Test that the spectrophotometer is reading the buffer as 'zero' by testing buffer with no sample in the machine.

    b. Run a spike test with the BCA assay. This is where you test for assay interference by adding a known amount of standard to a sample. If the value of this minus the standard value is equal to the sample value, then the assay passes the spike test.

9) Run the competitive CML ELISA (Cell Biolabs STA-816) according to manufacturer's instructions. Save a few wells of the plate for the following verifications:

    a. Test that the spectrophotometer is reading the buffer as 'zero'.

    b. Run a spike test with the CML ELISA.

10) Once your BCA assay, ELISA, and spectrophotometer are verified as working properly, quantify the CML concentrations according to the CML ELISA kit manufacturer's instructions and analyze between sample groups.
11) CML concentration in each tissue can be normalized against protein concentration to determine weight percent (ng CML per mg protein for each sample).